The Role of Amplitude, Phase, Polarization and their Interconnection in Nulling Interferometry

Proefschrift

ter verkrijging van de graad van doctor
aan de Technische Universiteit Delft,
op gezag van de Rector Magnificus prof. dr. ir. J.T. Fokkema,
voorzitter van het College voor Promoties,
in het openbaar te verdedigen op

donderdag 5 juni 2008 om 12.30 uur

door
Julien Félix Paul SPRONCK

Ingénieur civil physicien, Université de Liège
geboren te Luik, België

Dit proefschrift is goedgekeurd door de promotor:
Prof. dr. ir. J.J.M. Braat.

Toegevoegd promotor: Dr. S.F. Pereira.

Samenstelling promotiecommissie:

Rector Magnificus,	voorzitter
Prof. dr. ir. J.J.M. Braat,	Technische Universiteit Delft, promotor
Dr. S.F. Pereira,	Technische Universiteit Delft, toegevoegd promotor
Prof. dr. H.P. Urbach,	Technische Universiteit Delft
Prof. dr. J. Surdej,	Université de Liège
Prof. dr. C.U. Keller,	Universiteit Utrecht
Dr. P. Kern,	Laboratoire d'Astrophysique de Grenoble
Dr. ir. A.A.M. Maas,	TNO Science and Industry
Prof. dr. I.T. Young,	reservelid

This work was supported by TNO Science and Industry, Delft.

ISBN 978-90-78314-08-0

Cover: *Ursa Major*, Photo by Julien Spronck, Kinderdijk, 2008.

Those who dream by day are cognizant of many things which escape those who dream only by night.

Edgar A. Poe

To all dreamers.

Summary

Mercury, Venus, Mars, Jupiter, Saturn, Uranus and Neptune[1]: man has always been intrigued by these celestial bodies wandering in our sky like Gods watching over us. These planets all orbit around our Sun but many more planets are dancing around the hundreds of billions of other stars in our Galaxy while you are reading these lines.

The first extra-solar planet, or *exoplanet*, has been discovered in 1995 by Mayor and Queloz. Since then, roughly two hundred and seventy planets have been detected. Except for a few exceptions, all these planets were found by indirect methods, which means that no direct radiation coming from the planet has been detected. The challenge for direct detection of an Earth-like exoplanet is the combination of a huge brightness contrast between the star and the planet (10^6 in the best case) and a small angular separation (at a distance of 10 pc, the Sun-Earth distance is seen from an angle of 0.1 arcsec).

Mainly two promising techniques have been developed to meet this challenge: coronagraphy and nulling interferometry. A coronagraph is an instrument invented by Lyot in 1939 to observe the corona of the sun in which a mask placed at the focus of a telescope blocks the light coming from an on-axis source. Due to the limited size of the mask, light from an off-axis source is not blocked and is re-imaged onto a detector. This is the basic principle of coronagraphy but many changes have been brought to improve the cancellation up to the level required for Earth-like exoplanet detection. The second promising technique is called nulling interferometry, technique on which we concentrate in this thesis. It consists in looking at a star-planet system with an array of telescopes, and then combining the light from these telescopes in such a way that, simultaneously, destructive interference occurs for the star light and (partially) constructive interference for the planet light. The ratio between the intensities corresponding to constructive and destructive interferences is called the *rejection ratio*. To be able to detect an Earth-like planet, this ratio should be of the order of 10^6.

In addition to canceling the light from the star, nulling interferometry should also offer the possibility to obtain spectral information from the planet if one can achieve destructive interference simultaneously for all wavelengths in a wide spectral band (6-18 μm or even wider). To realize this, very stringent requirements must be fulfilled in terms of amplitude, phase and polarization of the fields to be combined. In this thesis, we analyze the role of amplitude, phase and polarization in nulling interferometry and their interconnection and use this information to develop new types of nulling interferometers.

To achieve destructive interference in a wide spectral band, most of the current nulling

[1]A planet, as defined by the International Astronomical Union (IAU) in 2006, is a celestial body orbiting a star or stellar remnant that is massive enough to be rounded by its own gravity, not massive enough to cause thermonuclear fusion, and has cleared its neighboring region of planetesimals. Using this definition, Pluto is not a planet.

interferometers make use of achromatic components. Unfortunately, manufacturing and using these components is technically challenging. In this thesis, we show that achromaticity is not always necessary. Reaching an infinite rejection ratio with wavelength-dependent components is possible in an infinitely wide spectral band, provided that the wavelength-dependence is somehow compensated. This is the concept of *chromatism compensation*.

In all current nulling interferometers, destructive interference is achieved by phase shifting. An alternative can be found by assuming coherent but arbitrary independent states of polarization for all beams. Indeed, we show that combining beams with different but coherent states of polarization can lead to a theoretically infinite rejection ratio. This can be achieved by rotating the polarization of all beams with achromatic polarization rotators. However, our approach only involves off-the-shelf wavelength-dependent components.

Since wavelength-dependent behavior is critical in nulling interferometry, a particular attention should be paid to dispersion. Indeed, since all beams pass through different materials with different wavelength-dependent refractive indices, dispersion affects the performance of the interferometer. By changing the wavelength-dependence of the phases, dispersion can either degrade or enhance the rejection ratio. In a nulling interferometer based on achromatic-phase shifting, dispersion should be compensated for since it decreases the rejection ratio. However, optimal use of dispersion can increase the rejection ratio in such a way that Earth-like extra-solar planet detection is possible without achromatic phase shifting.

In order to create interference, beams should be combined. This is realized with the help of a beam combiner. There are mainly two types of combination: uni-axial and multi-axial beam combination. In uni-axial combiners, beams are superimposed with beam-splitters to form only one beam. In a multi-axial combiner, a focusing optics is used to combine parallel beams in the image plane. We show that in a nulling interferometer based on multi-axial beam combination, a longitudinal field will be created at focus limiting the rejection ratio of the interferometer. Fortunately, this longitudinal field can be reduced to almost zero by using a single-mode optical fiber at focus of the combiner. Therefore, this fundamental limitation should not prevent us from detecting an Earth-like exoplanet.

The last chapter of this thesis shows the experimental results obtained with our table-top set-up for three different experiments. First, the set-up was used as a nulling interferometer with delay lines as phase shifters. Then, glass plates are inserted in the set-up to study the effect of dispersion and finally the set-up is changed into an interferometer based on polarization. The experimental results are drastically limited by spectral and polarization mismatchings between the beams and due to a lack of symmetry in the set-up. Finally, we present the design of a new set-up where these problems should be overcome, which can therefore lead to a much higher rejection ratio.

Julien Spronck,
April 2008

Samenvatting

Mercurius, Venus, Mars, Jupiter, Saturnus, Uranus en Neptunus[2]: de mens werd altijd geïntrigeerd door deze hemellichamen die wandelen in onze hemel zoals Goden die op ons letten. Deze planeten cirkelen rond onze Zon maar veel meer planeten dansen rond de honderden miljarden andere sterren in onze melkweg terwijl u deze regels leest.

De eerste exoplaneet, een planeet buiten ons zonnestelsel, werd ontdekt in 1995 door Mayor and Queloz. Sedertdien werden rond twee honderd en zeventig planeten gedetecteerd. Op een paar uitzonderingen na werden al die planeten gevonden via indirecte methodes. Dit betekent dat geen directe straling die van de planeet komt werd gedetecteerd. De uitdaging bij de directe opsporing van een Aardachtige exoplaneet is de combinatie van een reusachtig helderheidscontrast tussen de ster en de planeet (10^6 in het beste geval) en een kleine scheidinghoek (bij een afstand van 10 parsec wordt de Zon-Aarde afstand gezien onder een hoek van 0.1 arcsec).

Hoofdzakelijk werden twee veelbelovende technieken ontwikkeld om deze uitdaging aan te gaan: coronagrafie en nulling interferometrie. Een coronagraaf is een instrument uitgevonden door Lyot in 1938 om de zonnecorona waar te nemen, waarin een masker, dat in de brandvlak van een telescoop wordt geplaatst, het licht vanaf een bron op de as blokkeert. Wegens de beperkte grootte van het masker, wordt het licht, dat uit een off-axis bron komt, niet geblokkeerd en wordt op een detector afgebeeld. Dit is het basisprincipe van coronagrafie maar vele veranderingen werden gebracht om de uitdoving te verbeteren tot het niveau dat wordt vereist voor opsporing van Aardachtige exoplaneten. De tweede veelbelovende techniek is nulling interferometrie. In dit proefschrift concentreren we ons op die techniek. De techniek bestaat uit het bekijken van een ster-planeet stelsel met meerdere telescopen en het combineren van het licht vanaf deze telescopen op zodanige wijze dat, gelijktijdig, een destructieve interferentie voor het sterrelicht en een gedeeltelijk contructieve interferentie voor het planeetlicht plaatsvinden. De verhouding tussen de intensiteiten die behoren bij constructieve en destructieve interferenties wordt de *rejection ratio* genoemd. Om een Aardachtige planeet te detecteren zou deze verhouding van de orde van 10^6 moeten zijn.

Naast het onderdrukken van het sterrelicht, zou nulling interferometrie ook de mogelijkheid moeten bieden om spectrale informatie over de planeet te verkrijgen, als men destructieve interferentie gelijktijdig kan bereiken voor alle golflengten over een brede spectrale band (6-18 μm of breder). Om dit te realiseren moet aan heel strenge reisen worden vervuld in termen van amplitude, fase en polarisatie van de te combineren elec-

[2]Een planeet, zoals gedefinieerd door de Internationale Astronomische Unie (IAU) in 2006, is een hemellichaam dat rond een ster of een stellaire rest cirkelt die genoeg massief is om door zijn eigen gravitatie te worden rond gemaakt, niet voldoende massief is om thermonuclaire fusie te veroorzaken, en zijn naburig gebied van planetesimals heeft ontruimd. Volgens deze definitie is Pluto geen planeet.

trische velden. In dit proefschrift analyseren we de rol van amplitude, fase en polarisatie in nulling interferometrie en hun onderlinge samenhang en gebruiken we deze informatie om nieuwe soorten van nulling interferometers te ontwikkelen.

Om een destructieve interferentie te bereiken in een brede spectrale band maken de meeste huidige nulling interferometers gebruik van achromatische componenten. Helaas zijn de productie en het gebruik van deze componenten technisch lastig. In dit proefschrift tonen aan we dat achromaticiteit niet altijd noodzakelijk is. Het bereiken van een oneindig hoge rejection ratio met golflengte-afhankelijke componenten is mogelijk in een oneindig brede spectrale band, op voorwaarde dat de golflengte-afhankelijkheid op de een of andere manier wordt gecompenseerd. Dit is het concept van *chromatisme compensatie*.

In alle huidige nulling interferometers wordt destructieve interferentie bereikt door middel van faseverschuiving. Een alternatief kan worden gevonden door coherente maar willekeurig onafhankelijke polarisatietoestanden voor alle stralen te veronderstellen. Wij tonen inderdaad aan dat het combineren van stralen met verschillende maar coherente polarisatietoestanden tot een theoretisch oneindige rejection ratio kan leiden. Dit kan worden bereikt door de polarisaties van alle stralen te roteren met achromatische polarisatierotators. Maar, met onze methode, maken we slechts gebruik van eenvoudig verkrijgbare golflengte-afhankelijke componenten.

Aangezien de golflengte-afhankelijkheid in nulling interferometrie kritisch is, moet met dispersie rekening worden gehouden. Inderdaad, aangezien alle stralen door verschillende materialen met verschillende golflengte-afhankelijke brekingsindices reizen, beïnvloedt dispersie de prestaties van de interferometer. Door de golflengte-afhankelijkheid van de fases van de lichtbundels te veranderen kan dispersie de rejection ratio óf verslechteren óf verbeteren. In een nulling intererometer gebaseerd op achromatische faseverschuiving, zou dispersie moeten worden gecompenseerd vermits die de rejection ratio verslechtert. Maar een optimaal gebruik van dispersie kan de rejection ratio verhogen, zodanig dat detectie van een Aardachtige exoplaneet mogelijk is zonder achromatische faseverschuiving.

Om interferentie te creëren zouden de stralen moeten worden gecombineerd. Dit is gerealiseerd met behulp van een straalcombinatie-element. Hoofdzakelijk zijn er twee soorten van combinatie mogelijk: uni-axiale en multi-axiale combinatie. In een uni-axiale combiner worden de stralen tot overlapping gebracht met beam-splitters om vervolgens slechts één straal te vormen. In een multi-axiale combiner wordt een focusserende optiek gebruikt om parallelle stralen in het beeldvlak te combineren. We laten zien dat in een multi-axiale nulling interferometer een longitudinale component van het electrische veld in het brandvlak wordt gecreëerd. Deze component beperkt de rejection ratio van de interferometer. Gelukkig kan dit longitudinale veld tot bijna nul worden verminderd door ruimtelijk filteren met een monomode optische vezel. Daarom zou deze fundamentele beperking ons niet hoeven te verhinderen een Aardachtige exoplaneet te ontdekken.

Het laatste hoofdstuk van dit proefschrift geeft de experimentele resultaten weer die met onze opstelling worden verkregen voor drie verschillende experimenten. Eerst werd de opstelling gebruikt als nulling interferometer met vertragingslijnen als faseverschuivers. Vervolgens werden er glasplaten ingezet om het effect van dispersie te bestuderen en uiteindelijk werd de opstelling veranderd in een interferometer gebaseerd op polarisatie. De experimentele resultaten worden drastisch beperkt door ongelijke spectra en polarisatietoestanden en wegens een gebrek aan optische symmetrie in de opstelling. Uiteindelijk stellen we het ontwerp van een nieuwe opstelling voor waar deze mogelijkheden

overwonnen zouden moeten zijn en die daarom tot een veel hogere rejection ratio kan leiden.

Julien Spronck,
April 2008

Contents

Chapter 1

Introduction

Throughout the ages, the search for a new world and the insatiable need for exploration have always unleashed human passions. As children, we all have filled our minds with wonder dreaming about the extraordinary stories of famous explorers discovering an unknown land.

One of the first notable explorers was Marco Polo who, during the 13th century, travelled the Silk Road to China through the Mongol Empire; his travels were recorded by Rustichello da Pisa in the book *Il milione*. After the collapsing of the Mongol Empire, the route to the Far East became far more dangerous. In the 14th century, the Black Plague and the rise of the Ottoman empire drastically limited the possibilities of further exploration of Asia. The 15th century was of great importance for Western exploration since it marked the beginning of the Age of Discovery, period during which European explorers such as Christopher Colombus, Vasco da Gama and Ferdinand Magellan travelled all around the world searching for trading routes. Exploration by ship and by land continued until the early 20th century.

After fully covering and mapping the surface of the Earth, man decided to visit our outer space; it was the beginning of space exploration. Scientific advancements after World War II and during the Cold War enabled us to escape Earth's gravity in 1957 with the launch of the first artificial satellite, Sputnik 1. The Soviet Union also achieved the first human space flight by Youri Gagarine aboard Vostok 1 on April 12, 1961. On July 20, 1969, millions of people stared at the pictures of Neil Armstrong and Edwin Aldrin, first humans landing on the Moon.

Venus was the first planet of our solar system to be explored. The first flyby of Venus took place in 1962 with the American spacecraft Mariner 2. Our other *neighbor*, Mars, drew a lot of attention throughout the last decades and was the target of dozens of space missions. Other planets have also been visited by miscellaneous spacecrafts among which Galileo for Jupiter, Cassini-Huygens for Saturn, Voyager 2 for Uranus and Neptune and Mariner 10 for Mercury.

But still, mankind needed to go further: our dreams have no borders. The solar system was no longer enough. It was time to explore our galaxy. In our sole Milky Way, hundreds

of billions of stars wade through emptiness and infinity. Each of these stars could, like our sun, be the center of a planetary system and could, like our sun, be the source of Life. As Epicurus (341-270 BC) wrote in his Letter to Herodotus: "There is an infinite number of worlds, both like and unlike this world or ours". It is now up to us to discover these worlds.

1.1 Exoplanet detection

This endless need for exploration led to the discovery in 1995 of the first exoplanet by Mayor and Queloz [1]. This planet is a Jupiter-mass companion orbiting at 0.05 AU around the solar-type star 51 Peg. This planet has been detected using an indirect detection technique called *radial velocity method*, in which the movement of the star due to the presence of the planet can be detected by measuring the Doppler shift in the stellar spectrum induced by the change in radial velocity (see Figure 1.1(a)).

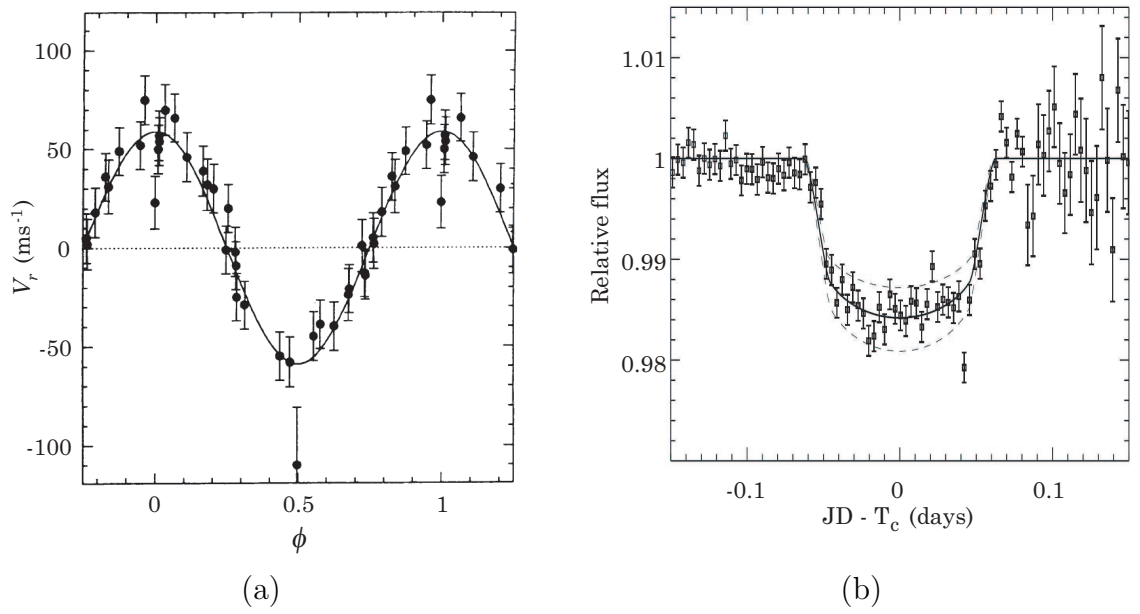

Figure 1.1: (a) Orbital motion of 51 Peg measured by Mayor and Queloz [1] and (b) first detected transit of an extra-solar planet, HD209458 by Charbonneau et al. [2].

Since 1995, much effort has been dedicated to the search for exoplanets in such a way that roughly 270 planets have been detected when these lines were written. Except for a few exceptions, all of them were detected by indirect methods, such as the radial velocity method, astrometry, transit and gravitational micro-lensing [3]. Up to now, radial velocity is the most successful method since 90% of the planets have been detected using this method. As for the radial velocity method, exoplanet detection by astrometry is based on the movement of the star, induced by the planet, around star-planet gravity center. The path of a star orbiting a star-planet barycenter appears as an ellipse when projected on the plane of the sky. Precise measurements of the astrometric position of the star would

directly give us the mass of the companion. Another succesful method is the *photometric transit* or *occultation* [2]. The principle is simple: starlight will be attenuated by the transit of the orbiting planet across its disk. We can see on Figure 1.1(b) the decrease in flux due to the transit of HD209458, the first extra-solar planet detected by occultation [2].

Gravitational micro-lensing is more complicated. It started with a paper by Einstein in 1936 [4] where he described the focusing of light by the curvature of space around a massive object, the so-called *gravitational lensing*. Consider two stars aligned with our Earth, the light coming from the distant star will be bent and focused by the gravitational field of the close-by star. The total amount of light detected is maximal in case of a perfect alignment and decreases when the observer is not perfectly aligned with the two stars. If an exoplanet is present around the star, another peak in the transmitted light will appear at a different time. This phenomenon is called *gravitational micro-lensing*. This method has the advantage to be more sensitive than the radial velocity and astrometric methods to low mass companions. Unfortunately, the amount of stars that can be studied is limited since star alignment cannot be chosen.

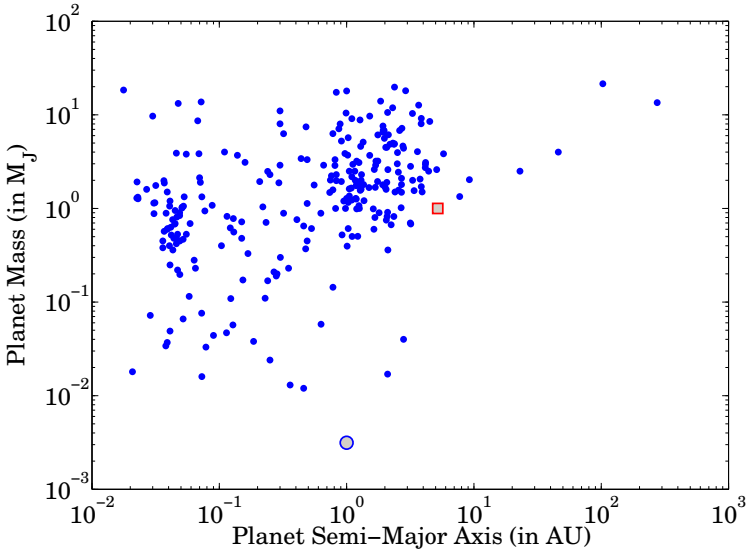

Figure 1.2: Mass of the detected planets as a function of the semi-major axis of their orbit. The square and the circle represent, respectively, Jupiter and the Earth.

Figure 1.2 depicts the mass of the detected exoplanets as a function of the semi-major axis of their orbit. Jupiter and the Earth are depicted, respectively, by a square and a circle. We can see that most of the detected extra-solar planets have a mass of the same order of magnitude as Jupiter, but are closer to their host star. These planets are referred to as *hot Jupiters*. Very few detected planets have a mass comparable to the mass of the Earth because of the currently limited sensitivity of the different detection methods. In the scope of this thesis, we will only concentrate on the detection of Earth-like extra-solar planets, which, in terms of mass, can be compared to our own planet.

1.2 Direct detection of an Earth-like planet

We have reviewed in the previous section the main indirect detection methods. These methods provide limited information about the planet, such as mass, semi-major axis, eccentricity and inclination but no fundamental knowledge on the physical nature of the planet. In order to characterize in more detail extra-solar planets, we need to directly detect light coming from the planet. By doing so, we could determine the atmospheric composition of the planet and use this knowledge to perhaps understand how Life developed on our own planet [5].

1.2.1 Life signature on extra-solar planets

Life can be defined as a chemical system capable of transferring its molecular information via self-replication and capable of evolving [6]. Searching for living beings does not seem a realistic task but a more accessible information would be the effects that Life has on its environment and the conditions for the environment to support Life. Life, defined as such, must develop within a liquid to take advantage of the diffusion of complex molecules. On Earth, Life is usually thought to have emerged in liquid water. For this reason, liquid water is considered as one of the prerequisites for Life [6, 7]. We can therefore characterize a planet as *habitable* if it can sustain liquid water at its surface [5]. The habitable zone around a star is the region where an eventual planet would be habitable.

Life, as we know it, is carbon-based. It is thought that carbon was mostly fully oxidized (CO_2) in the primitive atmosphere of terrestrial planets. This large amount of CO_2 is reduced by some process, such as photosynthesis, to release free oxygen. Since this gas is very reactive and oxidizes iron or sulfurs contained in planetary rocks, it would disappear rapidly from the atmosphere if not re-created. The massive presence of free O_2 (or O_3) and H_2O in an extra-solar planet atmosphere appears then as a criterion for the presence of carbon-based life [8].

Other bio-markers are important to detect: CO_2 indicates the presence of an atmosphere and abundant CH_4 can indicate biological sources [9].

We can see on Figure 1.3 the fluxes of the Sun and Earth as seen from 4 pc: some spectral features of the Earth flux are O_2, which can be detected in the visible, while H_2O, CO_2 and O_3 show some features in the mid-infrared (respectively at 6.3 μm, 15 μm and 9.6 μm).

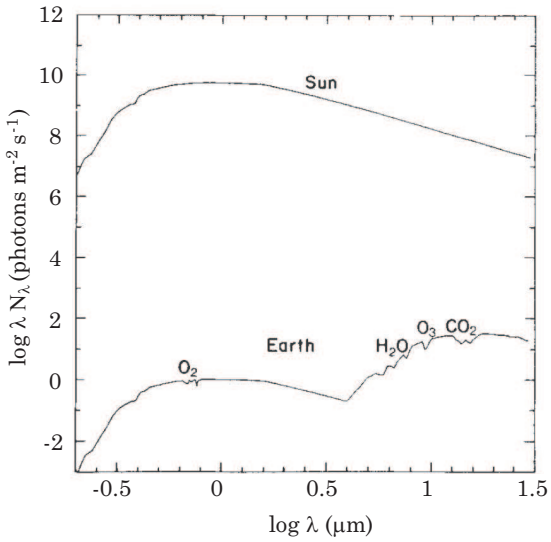

Figure 1.3: Fluxes of the Sun and Earth as seen from a distance of 4 pc [10].

1.2.2 Challenge for direct detection of Earth-like planets

The challenge for directly detecting light coming from an exo-Earth resides in the combination of three different issues:

1. a huge brightness contrast between the star and the planet; in the case of our Sun-Earth system, the star is typically 10^{10} brighter than the planet in the visible and 10^6 brighter in the mid-IR;
2. a small angular separation between the star and the planet; the Sun-Earth angular separation seen from a distance of 10 pc would be equal to 0.1 arcsec;
3. a wide observational spectral band; a wide band is required to perform spectroscopy and to optimally exploit the photon flux coming from the planet.

To overcome this challenge, two techniques have been developed: coronagraphy and nulling interferometry.

1.2.3 Coronagraphy

For visible and near-infrared wavelengths, observing two point sources with an angular separation of 0.1 arcsec with one single telescope requires a telescope diameter of at least 2 m. But, as mentioned earlier, at these wavelengths, the brightness contrast between the star and the eventual exo-Earth would be of the order of 10^{10}.

In order to see the planet, the star light has to be dimmed. This can be realized with an instrument called *coronagraph*, developed in 1939 by Bernard Lyot to observe the corona

of the Sun [11] (see Figure 1.4). In a Lyot coronagraph, light coming from the star is focused by a telescope onto a first image plane where an opaque mask is placed in the center. This mask blocks most of the light coming from the star and only lets through the high frequency content of the star signal. The unblocked portion of the light is then re-imaged onto a second image plane. An additional pupil stop is used to block the high frequencies which are mainly located at the periphery of the beam. If the size of the mask is well chosen, light coming from an off-axis source would be imaged next to the mask and would therefore be transmitted and re-imaged onto the second image plane, where detection takes place.

The level of cancellation of the star light strongly depends on the quality of the optics since wavefront distortion due to poor-quality optics will make more light to be imaged outside the mask. Another difficulty is that the physical extension of the opaque mask occults a large part of the central field and thus all sources located near the central object. A more efficient cancellation could be achieved with new coronagraphic techniques where the opaque mask is replaced by a phase mask. The first type of phase mask that has been developed is the π-phase shift phase mask [12], in which the π-phase shift creates a destructive interference for the central object. However, this phase mask exhibits a strong wavelength dependence and is sensitive to tip/tilt errors. Another type of phase mask is the four-quadrant phase mask [13]. The principle of this mask is to divide the focal plane into four quadrants with two of them providing a π-phase shift. This phase mask is well performing but suffers from two drawbacks. First, the π-phase shift is difficult to achieve achromatically. The second drawback is the presence of four λ/D-large areas (due to the four phase transitions between the adjacent quadrants) where the signal of the companion is attenuated by up to four magnitudes [14]. To overcome these issues, another phase mask has been designed, the annular groove phase mask [15], made up of concentric circular subwavelength gratings.

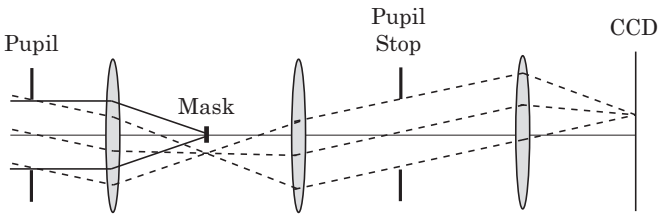

Figure 1.4: Principle of a Lyot coronagraph: on-axis light is blocked by an opaque mask while the light coming from an off-axis companion reaches the detector.

1.2.4 Nulling interferometry

The brightness contrast between the star and the planet is minimal in the mid-infrared around 10 μm and typically equal to 10^6. Unfortunately, at these wavelengths, a single telescope should have a typical diameter of 20 m in order to resolve two point sources

separated by an angular distance of 0.1 arcsec. Since the fabrication of such a telescope and its transport to the outer space is extremely challenging with the current technology, a more elegant solution would be to use multiple telescopes as a synthetic aperture.

The cancellation of the star light is then achieved by means of destructive interference, as proposed in 1978 by Bracewell [16]. This technique is called *nulling interferometry*. In the original Bracewell configuration, two telescopes point at an on-axis star (see Figure 1.5 (a)). Light coming from these two telescopes is recombined to produce interferences. If a π-phase shift is applied in one arm of the interferometer, the two beams will interfere destructively and the light from the star will be cancelled. For an eventual off-axis companion, an additional phase shift will be introduced between the beams in such a way that light coming from this companion will interfere (partially) constructively. The ratio between intensities corresponding to constructive and destructive interference, the so-called *rejection ratio*, should be of the order of 10^6 in order to detect an Earth-like planet.

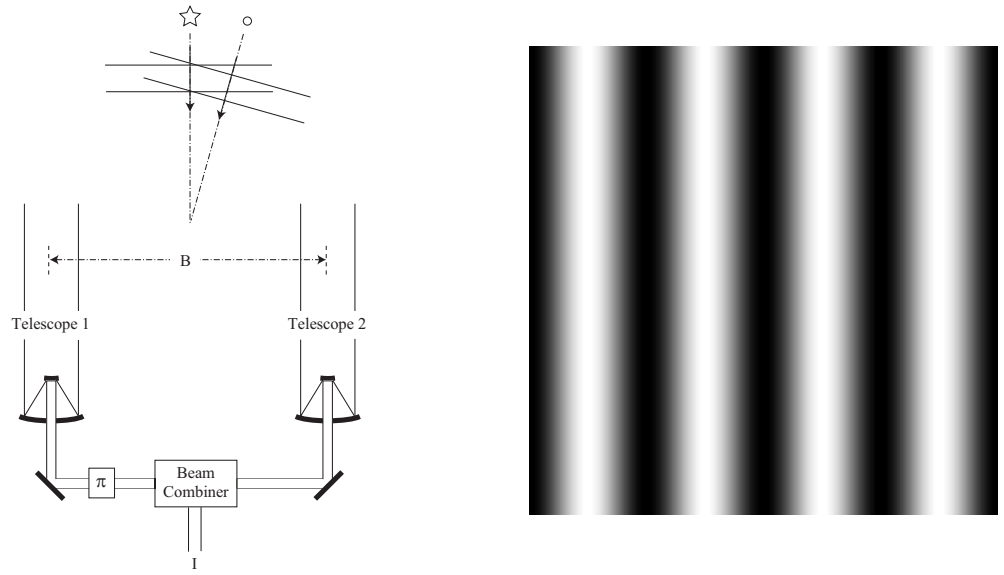

(a) (b)

Figure 1.5: (a) Principle of a nulling interferometer and (b) transmission map of the two-telescope Bracewell nulling interferometer.

Transmission map

The normalized response of the interferometer as a function of the position of the point source in the sky is called the *transmission map*. In the case of the two-telescope Bracewell configuration, the transmission map is merely a succession of dark and bright fringes as depicted in Figure 1.5(b). For small angular separations θ from the central point source, the Bracewell transmission map is proportional to θ^2. As we will discuss in this section, such a transmission map might prevent exoplanet detection.

A star is not a point source and has some non-negligible finite size. For example, the angular diameter of our sun seen from a distance of 10 pc is of the order of 5 nrad. To

detect an Earth-like exoplanet, we need to achieve a very low transmission across the whole stellar disk to prevent star light to leak through and reach the detector. This can be achieved with a short baseline interferometer. However, such a short baseline would not lead to fully constructive interference for the planet light. Another possibility to solve this issue would be to build an interferometer with a flatter transmission map [17]. That is why a transmission map proportional to θ^4 or, even better, to θ^6 is preferred. In theory, nulling interferometry can be performed with any number N of telescopes as long as the beams are recombined to achieve on-axis destructive interference. Depending on the number of beams, an ad hoc choice of amplitude ratios and phase differences between the beams can lead to θ^4 or θ^6 transmission maps. For example, Angel [17] proposed to achieve a transmission map proportional to θ^6 with a linear array of four telescopes, where the flat transmission map is achieved by combining two out-of-phase Bracewell interferometer outputs in such a way that the amplitude of one of the pairs is half the amplitude of the other pair. Such θ^6 transmission map would be very efficient to suppress the star light leaking through.

Modulation

All spatial information given by the transmission map is lost during detection, since the detector will integrate light coming from all directions in the field of view. This makes it impossible to distinguish between a bright object on a dark fringe and a faint companion on a bright fringe. As proposed by Bracewell, this problem can be solved by rotation of the interferometer [16]. Doing so, the intensity of the planet light will be modulated, while the star signal will remain constant.

Another difficulty is the possible emission from exo-zodiacal dust near the orbital plane of the planet. We, a priori, do not know anything about the exo-zodiacal cloud. However, by analogy with our own solar system, we can assume that it is centro-symmetric. A rotation of the two-telescope interferometer would modulate the planetary signal but would also modulate light from such a centro-symmetric source. A solution to this problem would be to use an asymmetric transmission map, which can be obtained by combining more than two beams. Indeed, with such an asymmetric response, the modulation frequency of the exo-zodiacal light would be twice as high as the modulation frequency of the planet signal and both can be discriminated.

However, rotation of the interferometer gives rise to very slow modulation and it will considerably decrease the number of targets that can be observed in the lifetime of a space mission. A more convenient solution is internal modulation [18]. This technique consists in applying rapid changes in the response of the interferometer in time, while keeping the star light cancelled at all times. This can be done, for example, by applying a time-varying phase shift between the nulled outputs of interferometric sub-arrays. Internal modulation does not involve rotation of the telescope array and is therefore much faster.

Achromatic phase shifters

The real challenge in nulling interferometry lies in the fact that a high rejection ratio should be achieved in a wide spectral band (typically 6–18 μm or even wider [10]). This wide band is required to spectroscopically characterize the atmosphere of the observed planets. To have destructive interference for all wavelengths simultaneously, the phase difference between the two beams must be equal to π for all wavelengths. In most nulling interferometers, this is realized with the help of an *achromatic phase shifter* [19]. The most common types of achromatic phase shifters are

- Focus crossing: a beam experiences an achromatic π-phase shift while crossing a focus;
- Rooftop mirrors [20]: this concept is based on the inversion of the electric field (π phase shift) by periscope-like mirrors;
- Fresnel rhombs [21]: based on properties of total internal reflection, they allow a π phase shift.
- Pancharatnam phase shifter [22, 23, 24]: the quasi-achromatic phase shift known as Pancharatnam phase shift is introduced by a cyclic change in the state of polarization. Any phase shift can be obtained with the possibility of fine tuning. However, this does not allow to work with both states of polarization simultaneously (dual-polarization mode);
- Birefringent achromatic phase shifter [25]: the electric field is flipped (π-phase shift) by an achromatic waveplate;
- Achromatic chessboard [26]: this achromatic phase shifter consists in cellular mirrors, in which each cell has a depth that introduces, for a given central wavelength, a phase shift of $(2k+1)\pi$ or $2k\pi$.
- Dispersive plates [27]: any phase shift can be applied with this method which uses cascaded dispersive plates with different and competing dispersions.

As mentioned, most of these methods only allow a π-phase shift and can only be used in certain configurations. Furthermore, manufacturing these achromatic phase shifters remains technically challenging. Note also that chromatic phase shifters such as delay lines can be used for certain configurations [28].

Beam combination

In order to create interference, light from different telescopes must be combined in a beam combiner. With conventional optics, there are two types of beam combination: uni-axial [20] and multi-axial [29, 30] combination (see Figure 1.6). In a uni-axial combiner, beams

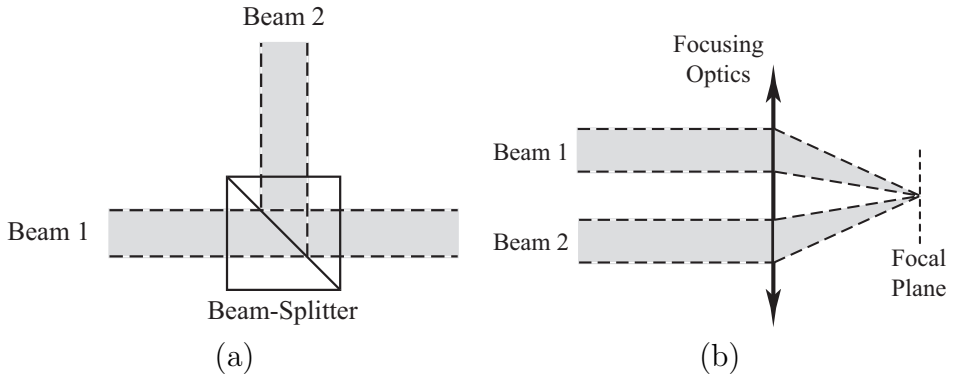

Figure 1.6: (a) Uni-axial and (b) multi-axial combination.

are superimposed with beam-splitters to form only one beam, which is then directed to the detector. The interference pattern is obtained temporally by scanning the optical path difference between the beams with a delay line. In a multi-axial combiner, the non-superimposed beams are imaged with a focusing optics and overlap only in the image plane, where the interference pattern spatially forms and where detection takes place. The advantage of the second method is that combination could be implemented with mirrors only and can therefore be achromatic. Also, this combination scheme is easily generalized to any number of beams.

Wavefront filtering

Another important stage in nulling interferometry is *wavefront filtering*. Indeed, achieving a quasi-perfect destructive interference leads to very stringent requirements in terms of the wavefronts of the beams to be combined. These requirements can be relaxed using a wavefront filter. It has been shown that an efficient way to perform wavefront filtering is to focus all beams into a common single-mode fiber [31, 32]. Indeed, whatever the incoming field, the field propagating through and transmitted by the fiber will be the fundamental mode of the fiber up to a complex factor, the so-called *complex coupling efficiency*. Therefore, any distortion of the incoming wavefront will be transformed by the fiber into an amplitude and phase change, which can be matched with delay lines and an amplitude-matching device.

Note that this single-mode fiber wavefront filtering holds for both types of beam combination. In a uni-axial combiner, the overlapping beams can be straightforwardly focused into a common fiber. In the case of a multi-axial beam combiner, the fiber can be positioned at the focus of the common imaging system [33].

State of the art

Since 1999, several groups have tried to demonstrate the feasibility of nulling interferometry for a space mission. All experimental results from these groups [34, 35, 30, 36, 29,

37, 38, 39, 40, 41, 42, 43, 44, 45, 46, 47] are summarized in Figure 1.7, which depicts the null depth[1] as a function of the bandwidth. Most of these measurements are two-beam measurements except for the results from Martin et al. [39], which is from the four-beam Planet Detection Testbed. The measurements corresponding to the squares were performed at visible wavelengths, the diamonds around 1.5 μm (H band), the star around 2.2 μm (K band) and the circles have been performed in the mid-infrared around 10 μm (N band). On the left of Figure 1.7, we can see the monochromatic measurements: a rejection ratio of 2.10^6 has been reached in the mid-infrared and even higher in the visible (10^7). These results show that achromatic effects such as pathlength variations can be controlled at a sufficient level.

The best broad-band experimental results so far were obtained in 2007 on the Adaptive Nuller testbed [48, 49], during which a rejection ratio of 8.10^4 has been reached with a 32% bandwidth. This result is very close to the minimal required performance for a space mission, which is a rejection of 10^5 in a 25% bandwidth or more.

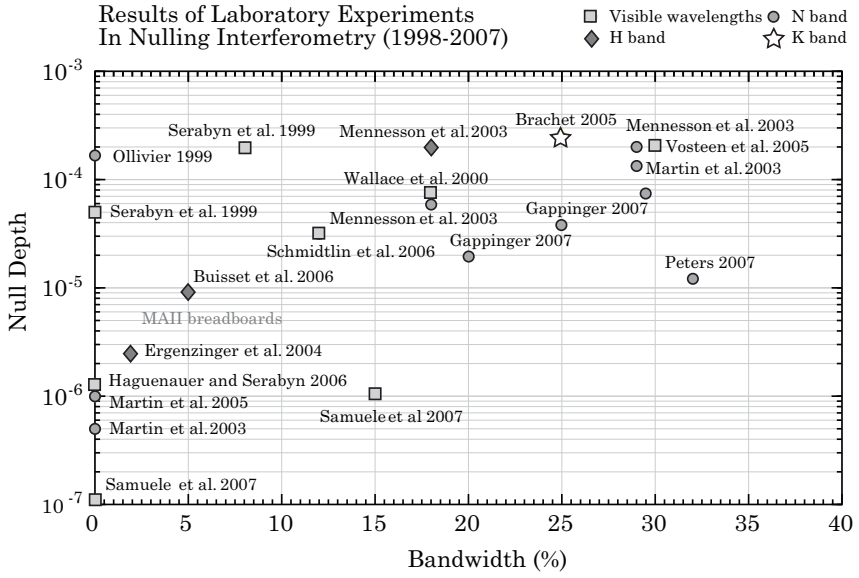

Figure 1.7: State of the art in nulling interferometry: null depth as a function of the bandwidth. The squares represent the measurements performed at visible wavelengths, the diamonds around 1.5 μm, the star around 2.2 μm and the circles have been performed in the mid-infrared around 10 μm. Courtesy of Peter R. Lawson (Jet Propulsion Laboratory, Caltech)

Context

Both European and American space agencies have plans to launch space missions that would make use of nulling interferometry to detect Earth-like exoplanets. The European mission is called Darwin, while its American equivalent is the Terrestrial Planet Finder - Interferometer (TPF-I). The Darwin project was proposed in 1993 in response to a Call for Ideas. Throughout the years, the configuration and the number of telescopes have

[1]The null depth is merely the inverse of the rejection ratio.

changed. The original proposal featured five telescopes. And then, it was thought that a better configuration should comprise six telescopes. However, in order to reduce the costs, a three-telescope configuration was proposed. Until recently, the Emma configuration, named after Charles Darwin's wife and consisting of three or four telescopes and an out-of-plane beam combiner, was the preferred one. The American counterpart preferred configuration was the stretched X-array. Recently, both the Darwin and TPF-I missions have adopted the Emma X-Array [50], a hybrid configuration between European and American designs, as the baseline configuration, getting closer to a single, joint TPF/Darwin mission.

1.3 Goal and outline of this thesis

With this thesis, we analyze both theoretically and experimentally the role of amplitude, phase and polarization in nulling interferometry and more importantly their interconnection in order to develop new types of nulling interferometers.

In Chapter 2, we introduce the concept of *chromatism compensation*, which allows us to relax the "achromaticity" condition considered in most nulling interferometers. Indeed, we show that chromatic devices can be used as long as the phase-induced chromatism is compensated by chromatic amplitudes or vice-versa.

In Chapter 3, we show that destructive interference can be achieved by changing the polarization of the beams instead of the phase of the beams. We design a new type of nulling interferometer which should allow a high rejection ratio in a theoretically infinitely wide spectral band. We show the main features of this interferometer and we study its sensitivity to imperfections.

In Chapter 4, we study the influence of dispersion in nulling interferometry. We show that dispersion can be used to enhance the performance of a nulling interferometer without achromatic phase shifter. On the other hand, in interferometers based on achromatic phase shifting, dispersion should be compensated for since it will automatically degrade the rejection ratio.

In Chapter 5, we perform a vectorial analysis of a multi-axial nulling interferometer. We first show with a simple ray tracing model that a longitudinal component of the electric field introduced by the focusing optics will limit the performance of the interferometer. We use rigorous diffraction theory to validate this model, and we analyze the filtering capabilities of a single-mode fiber with respect to the longitudinal field issue.

In Chapter 6, we present the experimental results obtained with our three-beam table-top interferometer with delay lines as phase shifters. We point out important limitations of the set-up: spectral and polarization mismatchings and a lack of symmetry between the beams. We also show the first measurements when the set-up is used as a polarization nulling interferometer. We then present the design of a totally-symmetric three-beam nulling interferometer and some of the tolerances required to reach a rejection ratio of

10^5. Finally, we validate experimentally with a two-beam set-up our theoretical results on dispersion obtained in Chapter 5.

Finally, our conclusions are summarized in Chapter 7.

Chapter 2

Chromatism compensation

In order to reach a high rejection ratio in a wide spectral band, most nulling interferometers use achromatic phase shifters (APS) [20, 24, 27, 51]. Indeed, it is usually thought that such a broadband high rejection ratio is only possible if all components satisfy an "achromaticity" condition. In this chapter, we show that this is not always necessary.

In Section 2.1, we derive the general condition to have on-axis destructive interference for an array of N telescopes, the so-called *nulling condition*. We introduce a simple vectorial formalism to analyze this condition. In Section 2.2, we give a general expression for the rejection ratio and we introduce the concept of chromatism compensation. In Section 2.3, we look at the conditions to have a θ^4-dependent transmission map. In Section 2.4, we look at the simple cases of a two and a three-beam nulling interferometer. In the latter, we apply the previously discussed concepts to the particular case where the phase shifters are delay lines and we demonstrate how various parameters can be optimized to reach the required rejection ratio. In Section 2.5, we study the influence of the type of beam combination on the results obtained in this chapter. Our conclusions are then summarized in Section 2.6.

2.1 Nulling condition for an N-telescope array

In this section, we derive the condition to have on-axis destructive interference for an array of N telescopes.

Let us consider N telescopes, all situated in the plane $z = 0$ and looking in the z direction (see Figure 2.1). The position of the center of the j^{th} telescope is given in polar coordinates by (L_j, δ_j). We assume that we can apply independent phases and amplitudes ϕ_j and A_j to each beam before recombination and that these phases and amplitudes are uniformly distributed over the pupil. We further assume that the beams are recombined with a uniaxial beam combiner associated with a single-pixel detector. For a point source located at an angular separation from the optical axis θ and at an azimuth angle φ, the complex

amplitude $f_\varphi(\theta)$ at the detector is given, within a constant factor, by

$$f_\varphi(\theta) = \sum_{j=1}^{N} A_j e^{i\phi_j} e^{ikL_j\theta\cos(\delta_j-\varphi)}, \tag{2.1}$$

where k is the wave number and where we have used the approximation $\sin\theta \simeq \theta$. Note that, if the observation direction is different from the z-axis, the optical path lengths have to be compensated with delay lines.

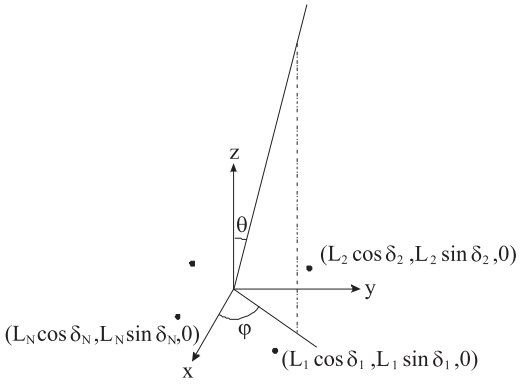

Figure 2.1: Array of telescopes (dots) situated in the plane $z = 0$ and looking in the z direction. The angles θ and φ define the direction of the incoming light. The position of the center of the j^{th} telescope is given in polar coordinates by (L_j, δ_j).

We define the transmission map $T_\varphi(\theta)$ as the normalized detected intensity,

$$T_\varphi(\theta) = \frac{|f_\varphi(\theta)|^2}{\max\left[|f_\varphi(\theta)|^2\right]}. \tag{2.2}$$

Since the angle θ is very small, we can expand the complex amplitude around $\theta = 0$ according to

$$f_\varphi(\theta) = f_\varphi(0) + \theta f'_\varphi(0) + \frac{\theta^2}{2} f''_\varphi(0) + \frac{\theta^3}{6} f'''_\varphi(0) + \cdots. \tag{2.3}$$

To have on-axis ($\theta = 0$) destructive interference, we must satisfy

$$f_\varphi(0) = \sum_{j=1}^{N} A_j e^{i\phi_j} = 0, \tag{2.4}$$

and this can be decomposed into two conditions :

$$\sum_{j=1}^{N} A_j \cos\phi_j = 0 \quad \text{and} \quad \sum_{j=1}^{N} A_j \sin\phi_j = 0. \tag{2.5}$$

If the complex amplitude from each telescope is represented by a vector with a length A_j and an angle ϕ_j with respect to an arbitrary reference, the conditions in Eq. (2.5) amount to nullify the sum of all vectors (see Figure 2.2).

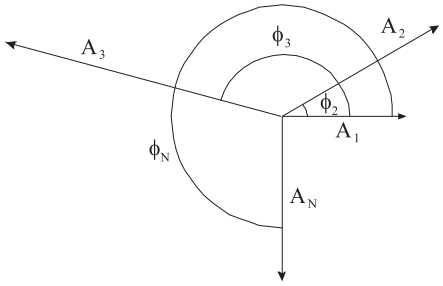

Figure 2.2: Vectorial representation of the combination of the N beams. The length and the angle of the vectors represent, respectively, the amplitude and the phase of the fields. The squared modulus of the sum of these vectors gives the on-axis ($\theta = 0$) detected intensity.

Since we can choose a certain amplitude and a certain phase as references, we actually have $(2N-2)$ unknowns and only two conditions. Two of these unknowns can thus be determined as a function of the other unknowns. For example, let us assume that these two unknowns are A_l and A_{l+1}. We can show that we have

$$\begin{pmatrix} A_l \\ A_{l+1} \end{pmatrix} = \frac{1}{\sin\left(\phi_{l+1} - \phi_l\right)} \begin{pmatrix} \sin\phi_{l+1} & -\cos\phi_{l+1} \\ -\sin\phi_l & \cos\phi_l \end{pmatrix} \begin{pmatrix} -\sum\limits_{j=1\neq l\neq l+1}^{N} A_j \cos\phi_j \\ -\sum\limits_{j=1\neq l\neq l+1}^{N} A_j \sin\phi_j \end{pmatrix}. \quad (2.6)$$

Using these expressions to find the amplitudes A_l and A_{l+1} ensures us that the nulling conditions are satisfied.

2.2 On-axis rejection ratio of an N-telescope array

If we define the rejection ratio as the ratio between the maximal and the minimal intensities of the interference pattern, we have that

$$R = \frac{1}{T_\varphi(0)} = \frac{\left|\sum\limits_{j=1}^{N} A_j\right|^2}{\left|\sum\limits_{j=1}^{N} A_j e^{i\phi_j}\right|^2}. \quad (2.7)$$

The denominator of Eq. (2.7) is the squared modulus of the sum of all the vectors defined in Section 2.1. If we want to reach a high rejection ratio in a wide spectral band, we have to satisfy the nulling conditions in Eq. (2.5) for each wavelength in the spectral band. But, unlike it is usually thought, this does not imply that all phases and amplitudes must be achromatic. Each phase and amplitude could be wavelength-dependent, provided that the sum of the vectors is equal to zero for every wavelength. Let us assume that we use a phase-matching device that will give chromatic phases. We usually think that this

chromatism will limit the rejection ratio. But, if we insert these chromatic phases in Eq. (2.6), we will find chromatic amplitudes A_l and A_{l+1}. There are thus chromatic amplitudes that will compensate the phase-induced chromatism in such a way that the rejection ratio is not affected since the nulling conditions are satisfied over the whole spectral band (*chromatism compensation*). Note that the inverse is also possible; we could compensate the chromatism induced by a certain amplitude-matching device using chromatic phases in order to fulfill the nulling conditions for each wavelength present in the spectral band. There is thus, in nulling interferometry, a very close relation between amplitude and phase.

Next, we derive an expression for the rejection ratio with either amplitude or phase mismatching. Let us first consider an amplitude mismatching ϵ_m for the m^{th} beam, as shown vectorially in Figure 2.3(a).

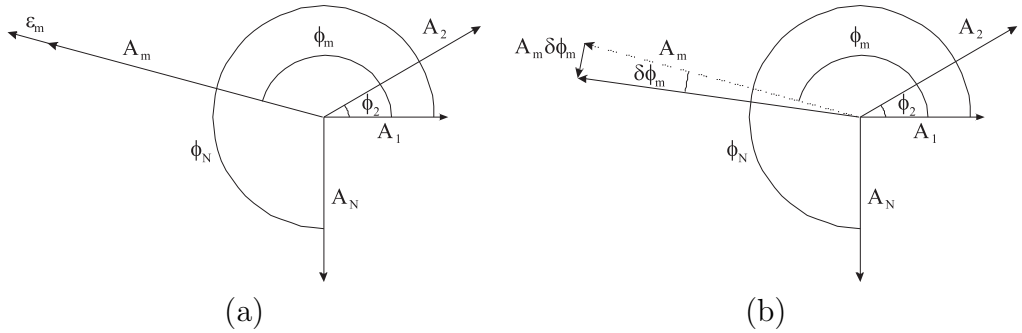

Figure 2.3: Vectorial representations of the N beams with (a) an amplitude mismatching ϵ_m and (b) a phase mismatching $\delta\phi_m$ for the m^{th} beam.

The amplitudes and the phases have been chosen so that the nulling conditions in Eq. (2.5) are satisfied. Without mismatching, the sum is thus equal to zero. In presence of an amplitude mismatching, the modulus of the sum is simply given by $|\epsilon_m|$, in such a way that the rejection ratio is given by

$$R = \frac{\left|\sum_{j=1}^{N} A_j\right|^2}{\epsilon_m^2}. \tag{2.8}$$

We now assume a phase mismatching $\delta\phi_m$ for the m^{th} beam, as shown in Figure 2.3(b).

Similarly, the rejection ratio is given by

$$R = \frac{\left|\sum_{j=1}^{N} A_j\right|^2}{A_m^2 \delta\phi_m^2}. \tag{2.9}$$

For example, a phase mismatching of 1 mrad gives, for a two-beam nulling interferometer, a rejection ratio of $R = 4 * 10^6$.

2.3 θ-dependence of the transmission map of an N-telescope array

As explained in the introduction, a transmission map proportional to θ^4 or θ^6 is preferable to prevent stellar leakage. In order to have a θ^4-transmission map, it follows from Eq. (2.2) and Eq. (2.3) that, in addition to the nulling conditions, we must also satisfy

$$f'_{\varphi}(0) = \sum_{j=1}^{N} A_j L_j \cos(\delta_j - \varphi) e^{i\phi_j} = 0. \tag{2.10}$$

Since this should be true for all azimuth angles, we actually have the following four conditions :

$$Q_{41} = \sum_{j=1}^{N} A_j L_j \cos\delta_j \cos\phi_j = \sum_{j=1}^{N} A_j X_j \cos\phi_j = 0, \tag{2.11a}$$

$$Q_{42} = \sum_{j=1}^{N} A_j L_j \cos\delta_j \sin\phi_j = \sum_{j=1}^{N} A_j X_j \sin\phi_j = 0, \tag{2.11b}$$

$$Q_{43} = \sum_{j=1}^{N} A_j L_j \sin\delta_j \cos\phi_j = \sum_{j=1}^{N} A_j Y_j \cos\phi_j = 0, \tag{2.11c}$$

$$Q_{44} = \sum_{j=1}^{N} A_j L_j \sin\delta_j \sin\phi_j = \sum_{j=1}^{N} A_j Y_j \sin\phi_j = 0. \tag{2.11d}$$

We can see that if the nulling conditions can be satisfied with chromatic phases and amplitudes, it is not straightforward to fulfill these θ^4-conditions in Eq. (2.11) chromatically since the positions of the telescopes are included in the conditions and obviously, these cannot be wavelength-dependent. Note that these conditions can only be satisfied if the number of telescopes is larger than two.

2.4 Examples

In the previous sections, we have presented a general theory for an array of N telescopes. In reality, however, the number of telescopes is limited to a few. Therefore, it can be interesting to see how the nulling conditions in Eq. (2.5) can be fulfilled in the case of N being small. Thus, in this section, we will look at two simple cases : a two- and a three-beam nulling interferometer.

2.4.1 Two-beam nulling interferometer

In this case, we observe that satisfying the nulling conditions amounts to nullify the sum of two vectors, as shown in Figure 2.4(a).

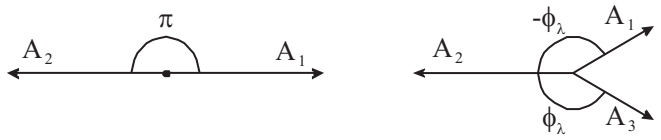

(a) (b)

Figure 2.4: Vectorial representations of (a) a two-beam and (b) the studied three-beam nulling interferometers.

It is obvious that the sum of these vectors can only be equal to zero if the vectors are opposite to each other, which means that the amplitudes of the two beams must be equal, and that the phase difference between the two beams must be equal to π for all wavelengths. For a two-beam nulling interferometer, the use of an achromatic phase shifter with π phase difference is necessary in order to reach a high (theoretically infinite) rejection ratio in a wide spectral band.

2.4.2 Three-beam nulling interferometer

For the case of three beams and considering the second beam as a reference for the phases ($\phi_2 = 0$), we have the following nulling conditions :

$$A_1 \cos\phi_1 + A_3 \cos\phi_3 = -A_2, \tag{2.12a}$$

$$A_1 \sin\phi_1 + A_3 \sin\phi_3 = 0. \tag{2.12b}$$

For the particular case where $\phi_3(\lambda) = -\phi_1(\lambda) = \phi_\lambda$, we find

$$A_3 = A_1, \tag{2.13a}$$

$$A_2 = -2A_1 \cos\phi_\lambda, \tag{2.13b}$$

which vectorially corresponds to Figure 2.4(b).

This result is important in the sense that, for a three-beam nulling interferometer, it is possible to compensate the chromatism induced by the phase-matching device using chromatic amplitudes in such a way that the nulling conditions can be satisfied in a wide spectral band (chromatism compensation). In this case, the use of achromatic phase shifters is not necessary once the amplitudes can be set according to Eq. (2.13a) and Eq. (2.13b). The difficulty of having achromatic phase shifters is then shifted to the difficulty of obtaining accurate spectral profiles [52]. Note that chromatism compensation is possible for every configuration with more than two telescopes.

Physical implementation

A question that can arise is how could we achieve the chromatic amplitudes of Eq. (2.13b). One possibility would be to separate spatially all wavelengths using a diffractive element.

Once the wavelengths are separated, a spatial light modulator, such as a liquid crystal (in single-polarization mode) can be used to achieve the desired spectrum. An identical diffractive element is then used to recombine all wavelengths into one single beam.

This example is not the only possibility. However, whatever the device used to shape the spectrum of the beams, we should always stay aware that this device will also probably affect the phase (and also the polarization) of the beams. Since, as discussed previously, amplitude and phases are coupled, we have to make sure that the nulling conditions in Eq. (2.5) will be fulfilled.

Optimal constant amplitude

In practice, we often use (quasi-)achromatic amplitude-matching devices. Therefore, it can be interesting to see what rejection ratio can be obtained with chromatic phases and "constant" amplitudes.

Hereafter, all amplitudes are defined with respect to the amplitude of the first beam A_1. The term "constant amplitude" means thus that the amplitudes A_2 and A_3 will be of the type

$$A_j = c_j A_1, \tag{2.14}$$

where c_j is a constant. To find the optimal values for c_j, we will consider A_1 to be independent of the wavelength but the results can be applied to the case where A_1 is a function of wavelength as well. Because of our choice of phase shifts ($\phi_3(\lambda) = -\phi_1(\lambda) = \phi_\lambda$), we already know (see Eq. (2.13)) that $A_3 = A_1$, i.e. $c_3 = 1$.

We also know that there is a chromatic amplitude ratio $a_2 = A_2/A_1 = -2\cos\phi_\lambda$ for which the nulling conditions are satisfied in the whole spectral band. This amplitude varies over the spectral band between a minimal value a_{min} and a maximal value a_{max}. If we use a constant amplitude c_2, the rejection ratio will be limited because the nulling conditions are not fulfilled for every wavelength. Defining the amplitude mismatching as the maximal distance between the used amplitude (constant in this case) and the nominal chromatic amplitude, this amplitude mismatching will be minimal if

$$c_2 = \frac{a_{\min} + a_{\max}}{2}. \tag{2.15}$$

The amplitude $A_{2,opt} = c_2 A_1 = A_1 \left(a_{\min} + a_{\max}\right)/2$ is called the optimal constant amplitude and we define d as the corresponding amplitude mismatching,

$$d = \frac{a_{\max} - a_{\min}}{2}. \tag{2.16}$$

Let us assume that, with a certain phase-matching device, we want to reach a phase shift equal to α. Because of this phase-matching device, we will actually have $\phi_\lambda = \alpha + \epsilon\left(\lambda\right)$. There will thus be a phase variation $\Delta\epsilon$ around the nominal phase shift α (see Figure 2.5). Note that it is important to adjust the phase-matching device so that this phase variation is symmetric around the desired phase shift. Indeed, this will lead to the minimal phase

mismatching. Because of this phase variation, the extremity of the vector $\vec{A_1}$ will describe an arc of a circle. The projection of this arc along the horizontal axis is equal to the distance d, previously defined as the amplitude mismatching corresponding to the optimal constant amplitude.

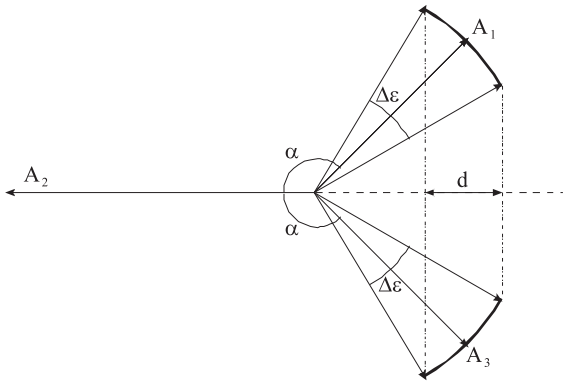

Figure 2.5: Phase variation $\Delta\epsilon$ around the desired phase shift α. This phase variation is then translated in terms of amplitude variation $2d$ by projecting the vectors A_1 and A_3 horizontally.

To derive an expression for the rejection ratio, we choose the amplitude of the first beam as a reference ($A_1 = A_0$ for all wavelengths). Using Eq. (2.8), we find that the minimal rejection ratio in the spectral band is given by

$$R_{\min} = \frac{(2A_0 + A_{2,opt})^2}{d^2}. \tag{2.17}$$

If the phase variation $\Delta\epsilon$ does not depend on the phase shift α, it is geometrically obvious (see Figure 2.5) that the distance d will be minimal for $\alpha = \pi$. This configuration will therefore give the highest rejection ratio.

Delay lines as phase shifters

If we use delay lines as phase shifters, then the phase shifts are of the type

$$\phi_k = \frac{k\alpha}{k_0}, \tag{2.18}$$

where k_0 is the reference wave number and is chosen in such a way that the phase variation $\Delta\epsilon$ is symmetric around the phase shift α. If k_m and k_M are respectively the minimal and maximal wave numbers, we can show that the reference wave number is given by

$$k_0 = \frac{k_m + k_M}{2}. \tag{2.19}$$

If we define B as the ratio between the maximal and the minimal wave numbers in the spectral band, we can show that the phase variation $\Delta\epsilon$ is given by

$$\Delta\epsilon = 2\alpha\frac{B-1}{B+1}. \tag{2.20}$$

In this case, the phase variation depends on the phase shift α, but we can still show that the highest rejection ratio occurs when $\alpha = \pi$. In this particular case, we have that

$$d = 1 + \cos\left(\frac{2\pi}{B+1}\right) \quad \text{and} \quad A_{2,opt} = 1 - \cos\left(\frac{2\pi}{B+1}\right). \tag{2.21}$$

The minimal rejection ratio in the spectral band is then given by

$$R_{\min} = \frac{\left|3 - \cos\left(\frac{2\pi}{B+1}\right)\right|^2}{\left|1 + \cos\left(\frac{2\pi}{B+1}\right)\right|^2}. \tag{2.22}$$

The rejection ratio as a function of the normalized bandwidth B is depicted in Figure 2.6. We see, as expected, that the rejection ratio decreases as the bandwidth increases. The desired 10^6 rejection ratio can only be reached in a very narrow spectral band ($B = 1.06$). Indeed, in nulling interferometers using delay lines as phase shifters [53], a high rejection ratio in a wide spectral band can only be obtained by increasing the number of beams to $N = 6$ (as it was originally planned for the Darwin mission).

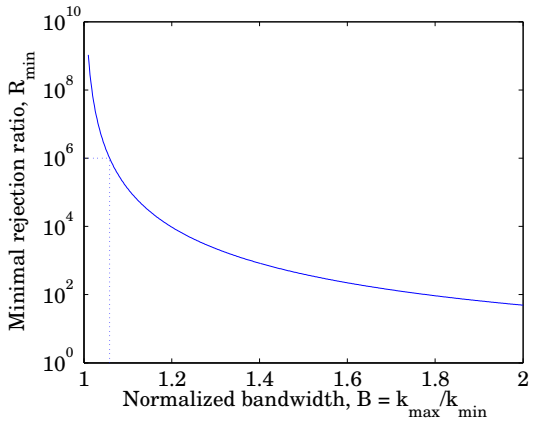

Figure 2.6: Rejection ratio as a function of the normalized bandwidth B for the three-telescope configuration that uses delay lines as phase shifters and achromatic amplitude-matching (used to reach the optimal constant amplitude).

Numerical example

Let us consider a spectral band from 500 nm to 650 nm, as it is the case in our table-top experimental set-up. In terms of wave numbers, we have $k_m = 9.67 \times 10^4$ cm^{-1} and $k_M = 1.26 \times 10^5$ cm^{-1}, which gives the value for $B = 1.3$. Replacing these values in Eq. (2.19), Eq. (2.21) and Eq. (2.22), we find

$$k_0 = 1.11 \times 10^5 \text{ cm}^{-1}, \quad A_{2,opt} = 1.917 \quad \text{and} \quad R = 2230. \tag{2.23}$$

We can see in Figure 2.7(a) the chromatic amplitude for which the rejection ratio is infinite and the optimal constant amplitude $A_{2,opt} = 1.917$. The rejection ratio corresponding to this constant amplitude as a function of the wave number is depicted in Figure 2.7(b).

We can see that the rejection ratio is infinite for the wave numbers at which chromatic and constant amplitudes are equal. Indeed at these wave numbers, the nulling conditions in Eq. (2.13) are satisfied. The rejection ratio is minimal when the difference between chromatic and constant amplitudes is maximal and equal to d. This minimal rejection ratio is equal to 2230. As discussed in the previous section, the rejection ratio in such a wide spectral band is very low. However, the rejection ratio can be improved by considering a larger number of beams, as proposed originally by Mieremet [53]. Note that, the amplitudes-matching device will not have an infinite accuracy. In practice, the amplitudes will be matched within 0.1%.

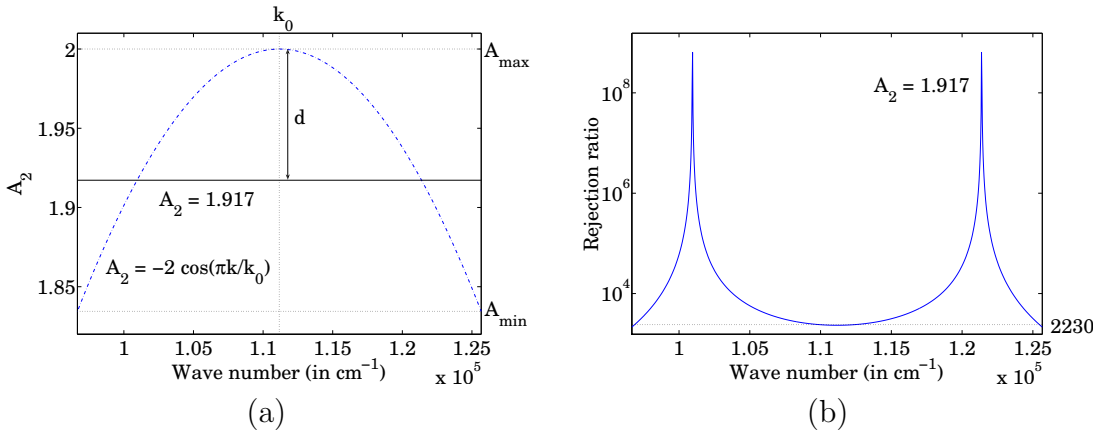

Figure 2.7: (a) Chromatic amplitude for which the rejection ratio is theoretically infinite over the whole spectral band (dash-dot line) and optimal constant amplitude (solid line). For this amplitude, the amplitude mismatching is equal to d. (b) Rejection ratio corresponding to the optimal constant amplitude. The minimal rejection ratio over the spectral band is equal to 2230.

2.4.3 N-beam nulling interferometer

Although the example of the three-beam interferometer has been treated in detail in order to match our experimental set-up, the concepts presented in this chapter can be applied to N-beam interferometers. In particular, it can be used in the case of four telescopes, which is the current plan for the Darwin mission.

In the case of four telescopes, an interesting solution can be found by assuming the following phase distribution,

$$\phi_1 = 0,\ \phi_2 = \phi_\lambda,\ \phi_3 = 2\phi_\lambda \text{ and } \phi_4 = 3\phi_\lambda. \tag{2.24}$$

These wavelength-dependent phases can be compensated by using the chromatic amplitudes,

$$A_4 = A_1, \tag{2.25a}$$

$$A_2 = A_3 = A_1\left[3 - 4\cos^2\left(\phi_\lambda/2\right)\right]. \tag{2.25b}$$

This configuration is interesting since, for $\phi_\lambda = \pi$, it leads to the phase distribution $(0, \pi, 2\pi, 3\pi)$ and the amplitude distribution $(1, 3, 3, 1)$, which is the configuration proposed by Mieremet for $N = 4$ in order to lower the requirements in terms of achromaticity [53].

2.5 Beam combination

As mentioned in Section 2.1, we made, throughout this chapter, the assumption that beams were combined with the help of a uni-axial beam combiner and detected by a monopixel detector. Indeed, in such a beam combiner, we can assume all beams to have identical pupil functions. These pupil functions can therefore merely be taken into account in the definition of the complex amplitude $f_\varphi(\theta)$ of Eq. (2.1) by a constant factor C, which does not affect the results,

$$f_\varphi(\theta) = C \sum_{j=1}^{N} A_j e^{i\phi_j} e^{ikL_j\theta\cos(\delta_j - \varphi)}. \tag{2.26}$$

This is not valid anymore in the case of a multi-axial beam combiner, since the pupil functions are identical functions but located at different positions. Let us consider the case of a multi-axial combiner with a single-mode optical fiber at focus of the imaging system for wavefront filtering. If the position of the j^{th} beam in the pupil plane of this imaging system is given in cartesian coordinates by (x_j, y_j), the total pupil function $\mathcal{P}(x, y)$ is given by

$$\mathcal{P}(x, y) = \sum_{j=1}^{N} A_j e^{i\phi_j} e^{ikL_j\theta\cos(\delta_j - \varphi)} \mathcal{P}_0(x - x_j, y - y_j). \tag{2.27}$$

where $\mathcal{P}_0(x, y)$ is the pupil function of one individual beam positioned at $(0, 0)$. The complex amplitude at the detector is given by the complex coupling efficiency of this total pupil function into the single-mode fiber [31],

$$f_\varphi(\theta) = \iint \mathcal{P}(x, y)\, \tilde{F}^*(x, y)\; dxdy, \tag{2.28}$$

where $\tilde{F}^*(x, y)$ is the complex conjugate of the fundamental mode of the single-mode fiber back-propagated to the pupil plane. Replacing Eq. (2.27) into Eq. (2.28), we find

$$f_\varphi(\theta) = \sum_{j=1}^{N} A_j e^{i\phi_j} e^{ikL_j\theta\cos(\delta_j - \varphi)} \iint \mathcal{P}_0(x - x_j, y - y_j)\, \tilde{F}^*(x, y)\; dxdy, \tag{2.29}$$

where the last integral represents the complex coupling efficiency of each individual beam. If the beams in the entrance pupil are regularly-spaced on a circle, the complex coupling efficiency of all beams will be identical due to the radial symmetry of the fundamental

mode of the fiber. Therefore, we have the same situation as in Eq. (2.26),

$$f_{\varphi}(\theta) = \sum_{j=1}^{N} A_j e^{i\phi_j} e^{ikL_j\theta\cos(\delta_j-\varphi)} \underbrace{\iint \mathcal{P}_0(x-x_j, y-y_j)\,\tilde{F}^*(x,y)\;dxdy}_{C'}, \tag{2.30}$$

in such a way that the results of this chapter are still valid in this case. However, if the beams in the entrance pupil are not regularly-spaced on a circle, each beam will have a different complex coupling efficiency. Since these complex coupling efficiencies are also wavelength-dependent, they have to be taken into account in the nulling conditions in order to compensate for phase-induced chromatism. In this case, even though the general idea of chromatism compensation can still be used, the results of this chapter cannot be directly applied.

Note that in practice, the desired beam configuration in the pupil plane will be circularly symmetric in order to have a pupil function as compact as possible, which would lead to an efficient coupling into the optical fiber.

2.6 Conclusions

We have shown that the interferometric nulling conditions can be fulfilled over a wide spectral band, using chromatic phases and amplitudes, leading thus to a high rejection ratio in this band. Therefore, we prove that an achromatic device is not always necessary. Chromatic devices can be used if we compensate the phase-induced chromatism by chromatic amplitudes or vice-versa (chromatism compensation). There is thus a very close relation between amplitudes and phases and the vectorial formalism that we introduced is a very simple and useful tool to look at this relation.

We have seen that, if the nulling conditions can be satisfied chromatically, it is not straightforward to fulfill the θ^4-conditions with chromatic phases and amplitudes, which can lead to an important 'stellar leakage'. However, there should be optimal configurations or modulation techniques for which this effect is reduced. But, such configurations have not been studied yet and their existence has to be confirmed in the future.

We have also shown that chromatism compensation is not possible for a two-beam nulling interferometer. For this kind of interferometer, it is thus mandatory to use achromatic phase shifters but also achromatic amplitude-matching devices and an achromatic beam combiner in order to reach a high rejection ratio in a wide spectral band.

We have looked in detail at the particular case of a three-beam nulling interferometer, where the phase shift between the second and the first beam is equal to the phase shift between the third and the second beam. We have seen that, with three beams, it is possible to use chromatism compensation and we have derived an expression for the rejection ratio if we use a chromatic phase-shifting device and an achromatic amplitude-matching device. We have applied this theory to the particular case where the phase-shifters were delay

lines. We have seen that for a certain spectral band, there are several parameters that we can use to optimize the rejection ratio (mean phase shift, reference wave number and optimal amplitude).

Finally, we have studied the influence of the type of beam combination on the results obtained in this chapter and we have seen that these results can be used in the case of uni-axial beam combination and also in the case of multi-axial beam combination if the beams in the pupil plane are regularly-spaced on a circle. If not, chromatism compensation can still be applied but attention should be paid to include the wavelength-dependence induced by the complex coupling efficiency of the beams into the single-mode optical fiber.

With the approach presented in this chapter, we showed new possibilities for direct detection of exoplanets by nulling interferometry.

Chapter 3

Polarization nulling interferometry

In this chapter, we introduce a new concept of nulling interferometer which uses polarization properties of light to achieve destructive interference. This type of interferometer should enable a high rejection ratio in a theoretically unlimited spectral band. Note that a similar analogy has been proposed in visible coronagraphy [54].

In Section 3.1, we derive the generalized condition to have on-axis destructive interference for an N-telescope array, including polarization effects. We apply this condition to a two- and a three-telescope configurations. In Section 3.2, we apply this concept for the case of a wide spectral band and we propose a design of a new type of nulling interferometer. In Section 3.3, we look at the interference patterns that can be obtained with the proposed design. In Section 3.4, we establish a criterion to define an acceptable width of the spectral band. In Section 3.5, we analyze the sensitivity of the proposed design with respect to some imperfections and misalignments. Our conclusions are then summarized in Section 3.7.

3.1 Generalized nulling condition

In this section, we derive the general condition to have on-axis destructive interference for an array of N telescopes and we look at some implications of this condition, in the case of a two- and a three-beam nulling interferometer.

Let us consider an array of N telescopes and let us assume that we can apply independent phases ϕ_j and amplitudes A_j to each beam before recombination. As we have seen in Chapter 2, the condition to have on-axis destructive interference (nulling condition) is given by

$$\sum_{j=1}^{N} A_j \exp\left(i\phi_j\right) = 0. \tag{3.1}$$

A more general condition can be derived by including the vector character of the beams and assuming coherent but arbitrary and independent states of polarization for each of them. Using Jones formalism [55] to describe polarization, the generalized condition is

given by

$$\sum_{j=1}^{N} \vec{A}_j \exp(i\phi_j) = \sum_{j=1}^{N} \begin{pmatrix} A_{x,j} \\ A_{y,j} \end{pmatrix} \exp(i\phi_j) = \vec{0}, \tag{3.2}$$

where $A_{x,j}$ and $A_{y,j}$ are complex numbers representing the polarization state of the j^{th} beam. This generalized condition has very important consequences since it can lead to a new type of nulling interferometers, as discussed below.

3.1.1 Example 1: Two-beam nulling interferometer

In the case of a two-beam nulling interferometer, the generalized nulling condition in Eq. (3.2) simply amounts to

$$\vec{A}_1 \exp(i\phi_1) = -\vec{A}_2 \exp(i\phi_2). \tag{3.3}$$

In most current nulling interferometers, this condition is satisfied by applying a π-phase shift between the two beams ($\phi_2 = \phi_1 + \pi$). The condition in Eq. (3.3) could also be fulfilled without any phase shift but considering a rotation of the polarization plane of one of the beams over an angle π ($\vec{A}_1 = -\vec{A}_2$). This idea has been exploited in several concepts of achromatic phase shifters [20, 25]. However, although mathematically equivalent to an achromatic phase shift, this is a fundamentally different approach, as it will appear more clearly in the following example.

3.1.2 Example 2: Three-beam nulling interferometer

In this case, we have the following nulling condition.

$$\vec{A}_1 \exp(i\phi_1) + \vec{A}_2 \exp(i\phi_2) + \vec{A}_3 \exp(i\phi_3) = \vec{0}. \tag{3.4}$$

If we assume that all the beams have the same phase, we have

$$\vec{A}_1 + \vec{A}_2 + \vec{A}_3 = \vec{0}. \tag{3.5}$$

This condition can be fulfilled by rotating the polarization of the beams. To this goal, we select a horizontal linear state of polarization for the first beam. We could then satisfy the condition in Eq. (3.5) using

$$\vec{A}_1 = A_0 \begin{pmatrix} 1 \\ 0 \end{pmatrix}, \tag{3.6a}$$

$$\vec{A}_2 = A_0 \begin{pmatrix} \cos\left(\frac{2\pi}{3}\right) & \sin\left(\frac{2\pi}{3}\right) \\ -\sin\left(\frac{2\pi}{3}\right) & \cos\left(\frac{2\pi}{3}\right) \end{pmatrix} \begin{pmatrix} 1 \\ 0 \end{pmatrix} = A_0 \begin{pmatrix} \cos\left(\frac{2\pi}{3}\right) \\ -\sin\left(\frac{2\pi}{3}\right) \end{pmatrix}, \tag{3.6b}$$

$$\vec{A}_3 = A_0 \begin{pmatrix} \cos\left(\frac{4\pi}{3}\right) & \sin\left(\frac{4\pi}{3}\right) \\ -\sin\left(\frac{4\pi}{3}\right) & \cos\left(\frac{4\pi}{3}\right) \end{pmatrix} \begin{pmatrix} 1 \\ 0 \end{pmatrix} = A_0 \begin{pmatrix} \cos\left(\frac{4\pi}{3}\right) \\ -\sin\left(\frac{4\pi}{3}\right) \end{pmatrix}. \tag{3.6c}$$

This shows that we can satisfy the nulling condition without any phase shifter but only by rotating the polarization and consequently cancel the light coming from an on-axis star.

If a planet is orbiting around that star, then the planetary light coming from the different telescopes will have different optical path lengths. Therefore, it can be interesting to look at the detected intensity as a function of the optical path differences between the three beams. Let us first consider the monochromatic case. The detected amplitude as a function of the optical path differences is given, up to a constant phase factor, by

$$\vec{A}_{tot} = \vec{A}_1 + \vec{A}_2 \exp\left(i\Delta\phi_{21}\right) + \vec{A}_3 \exp\left(i\Delta\phi_{31}\right). \tag{3.7}$$

where $\Delta\phi_{21}$ and $\Delta\phi_{31}$ are respectively the phase differences between beams 2 and 1 and between beams 3 and 1 due to optical path differences. The detected intensity is then given by the squared modulus of the amplitude in Eq. (3.7).

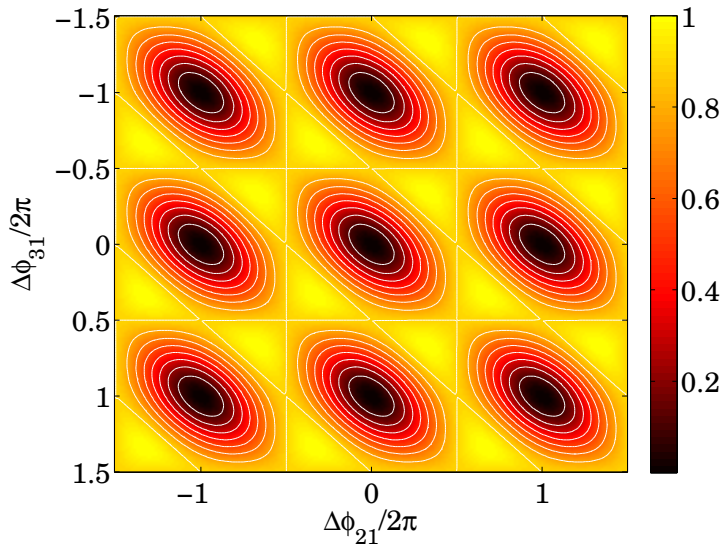

Figure 3.1: Normalized intensity as a function of the phase differences between the three beams resulting from the optical path differences.

In the case of the example of Eqs. (3.6), we find the detected intensity depicted in Figure 3.1. The rejection ratio, defined as the ratio between the maximal and minimal intensities of the interference pattern, is theoretically infinite.

It is usually thought that beams with different coherent states of polarization cannot interfere with a high contrast. Our example shows that we can make three differently-polarized coherent beams interfere with a theoretically perfect contrast. This is also true for N beams provided that $N > 2$. The second consequence is that, since the intensity depends on the optical path differences, it should be possible to have constructive interference for the light coming from the planet. The important fact is that the destructive interference takes place at the zero-OPD position. In that case, there is no wavelength-dependent phase difference between the beams.

3.2 Applications in wide-band nulling interferometry

In this section, we look at the generalized condition working over a wide spectral band in order to design a new type of nulling interferometer.

To reach the amplitudes in Eqs. (3.6) for every wavelength in the spectral band, we would need achromatic polarization rotators. This is possible by combining different waveplates to create achromatic half-wave plates [56, 57] or by using zero-order gratings [25]. But we choose a different approach, as explained below.

Suppose a system of N beams, initially horizontally linearly polarized (x direction). Each polarization is then changed using a simple waveplate whose principal axis makes an angle α with the horizontal (see Figure 3.2). If T_r and T_α are the complex transmission coefficients of the waveplate in its principal directions ($T_r = |T_r|$ and $T_\alpha = |T_\alpha| \exp(i\phi_{o-e})$, where ϕ_{o-e} is the phase difference between the ordinary and extraordinary waves), the Jones matrix of that waveplate at an angle $\alpha = 0$ is given by

$$M_w(0) = \begin{pmatrix} T_r & 0 \\ 0 & T_\alpha \end{pmatrix}. \tag{3.8}$$

For an orientation α of the waveplate, the Jones matrix would then be

$$M_w(\alpha) = R(-\alpha)\, M_w(0)\, R(\alpha) = \begin{pmatrix} T_r \cos^2\alpha + T_\alpha \sin^2\alpha & \frac{1}{2}\sin 2\alpha\,(T_r - T_\alpha) \\ \frac{1}{2}\sin 2\alpha\,(T_r - T_\alpha) & T_r \sin^2\alpha + T_\alpha \cos^2\alpha \end{pmatrix}, \tag{3.9}$$

where $R(\alpha)$ is the rotation matrix at an angle α. The field components after the waveplate are then given by

$$\vec{A} = A \begin{pmatrix} T_r \cos^2\alpha + T_\alpha \sin^2\alpha & \frac{1}{2}\sin 2\alpha\,(T_r - T_\alpha) \\ \frac{1}{2}\sin 2\alpha\,(T_r - T_\alpha) & T_r \sin^2\alpha + T_\alpha \cos^2\alpha \end{pmatrix} \begin{pmatrix} 1 \\ 0 \end{pmatrix} = A \begin{pmatrix} T_r \cos^2\alpha + T_\alpha \sin^2\alpha \\ \frac{1}{2}\sin 2\alpha\,(T_r - T_\alpha) \end{pmatrix}, \tag{3.10}$$

with A the amplitude of the incident beam, linearly polarized along the x-direction.

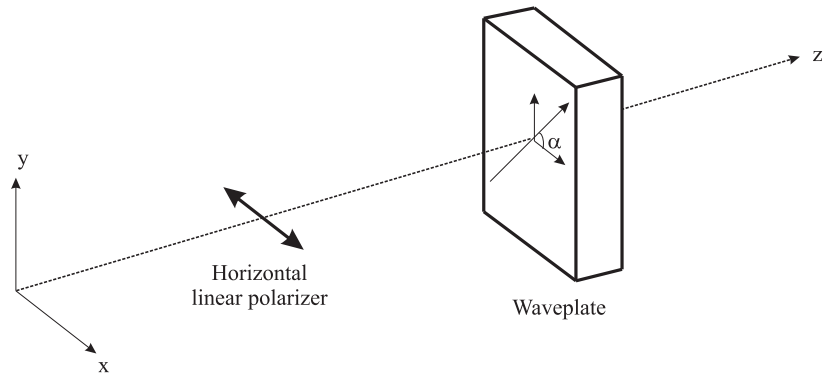

Figure 3.2: The polarization of each beam (initially linear in the x direction (horizontal)) is changed after a waveplate whose principal axis makes an angle α with the horizontal.

Since we want on-axis destructive interference in the absence of any phase difference between the beams and assuming that all the waveplates are exactly the same but with

different orientations, we must satisfy

$$\sum_{j=1}^{N} A_j \begin{pmatrix} T_r \cos^2\alpha_j + T_\alpha \sin^2\alpha_j \\ \frac{1}{2}\sin 2\alpha_j \,(T_r - T_\alpha) \end{pmatrix} = \begin{pmatrix} T_r \sum_{j=1}^{N} A_j \cos^2\alpha_j + T_\alpha \sum_{j=1}^{N} A_j \sin^2\alpha_j \\ \frac{1}{2}(T_r - T_\alpha) \sum_{j=1}^{N} A_j \sin 2\alpha_j \end{pmatrix} = \vec{0}. \tag{3.11}$$

Using a simple waveplate in a wide spectral band, T_r and T_α will be wavelength-dependent in such a way that the first component of the vector in Eq. (3.11) cannot be equal to zero for every wavelength. The second component, on the other hand, can be canceled achromatically by a good choice of the amplitudes A_j and angles α_j. If we add, for each beam, a perfect vertical linear polarizer after the wave plate, the amplitude of the j^{th} beam is then given by

$$\vec{A_j} = \begin{pmatrix} 0 \\ \frac{1}{2}A_j \,(T_r - T_\alpha)\sin 2\alpha_j \end{pmatrix}, \tag{3.12}$$

and the nulling condition simply amounts to

$$\sum_{j=1}^{N} A_j \sin 2\alpha_j = 0. \tag{3.13}$$

This condition is wavelength-independent. Therefore the null is achromatic if we assume identical waveplates.

In this proposed type of nulling interferometers, each beam encounters a horizontal linear polarizer, a waveplate and a vertical linear polarizer (see Figure 3.3). Thus, it should be possible to reach a high rejection ratio in a wide spectral band with simple commercially available components. For example, in the case of a two-beam nulling interferometer and choosing $A_1 = A_2$, the condition to have an achromatic null is that $\alpha_2 = \pi - \alpha_1$ or $\alpha_2 = \pi/2 + \alpha_1$. In order to maximize the transmission of the interferometer, we can choose $\alpha_1 = \pi/4$ and $\alpha_2 = 3\pi/4$. This can also be easily applied to a three-beam nulling interferometer by choosing for example $A_1 = A_2 = A_3$, $\alpha_1 = \pi/4$, $\alpha_2 = 7\pi/12$ and $\alpha_3 = 11\pi/12$.

Note that we would have obtained similar results if the beams were initially vertically linearly polarized. We then could use a polarizing beam splitter instead of the first linear polarizer and apply the same principle to both outputs of the beam splitter in order to use the whole incoming power.

3.3 Transmission and modulation

In this section, we look at several direct consequences of the proposed design in the case of a three-beam nulling interferometer.

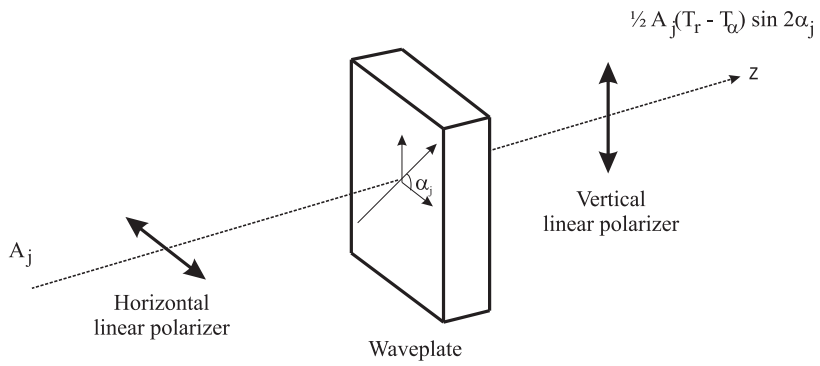

Figure 3.3: Design of a new type of nulling interferometer; each beam encounters a horizontal linear polarizer, a waveplate and a vertical linear polarizer.

3.3.1 Transmission map

Let us consider N coplanar telescopes looking in the same direction z (see Figure 3.4). The position of the j^{th} telescope is given in polar coordinates by (L_j, δ_j). For a point source located at an angular separation from the optical axis θ and at an azimuth angle φ, the detected complex amplitude $\vec{f_\varphi}(\theta)$ is given by

$$\begin{aligned} \vec{f_\varphi}(\theta) &= \sum_{j=1}^{N} \vec{A_j} \exp\left[ikL_j\theta\cos\left(\delta_j - \varphi\right)\right] \\ &= \sum_{j=1}^{N} \begin{pmatrix} 0 \\ \frac{1}{2}A_j\left(T_r - T_\alpha\right)\sin 2\alpha_j \end{pmatrix} \exp\left[ikL_j\theta\cos\left(\delta_j - \varphi\right]\right). \end{aligned} \tag{3.14}$$

Note that this expression is not general in the sense that the star which we point at lies on the z-axis. If this was not the case, there would be additional delays that are not taken into account here. Note also that this reasoning is valid only for a space mission where longitudinal dispersion[1] can be neglected. For any ground-based interferometer, this effect would decrease the performances of the interferometer.

In principle, the function $\vec{f_\varphi}(\theta)$ should also include the polarization and birefringent properties of the individual telescopes. We have not included this effect here because we suppose that the telescopes behave identically in this respect and that, on recombination, these effects are canceled. In reality, the polarization properties of the different telescopes can differ considerably (for example, on the VLTI). But this problem is not specific to the type of nulling interferometer considered here and is therefore out of the scope of this chapter.

[1]Longitudinal dispersion is the dispersion caused by the column of water vapor above the ground-based telescopes. This effect is important since water vapor is highly dispersive in the near- and mid-infrared and the column density randomly fluctuates. Longitudinal dispersion can be compensated to a sufficient level to perform ground-based nulling [58]. However, the main difficulty is the rapid time variability of the water vapor column density.

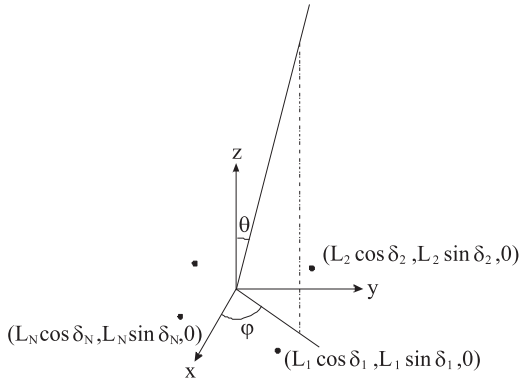

Figure 3.4: Array of telescopes (dots) situated in the plane $z = 0$ and looking in the z direction. The angles θ and φ define the direction of the incoming light. The position of the j^{th} telescope is given in polar coordinates by (L_j, δ_j).

If we define the transmission map $T_\varphi(\theta)$ as the normalized detected intensity, we have

$$T_\varphi(\theta) = \frac{\left|\vec{f_\varphi}(\theta)\right|^2}{\max\left[\left|\vec{f_\varphi}(\theta)\right|^2\right]}. \tag{3.15}$$

3.3.2 θ-dependence of the transmission map

Similarly to what has been shown in Chapter 2, in order to have a θ^4-transmission map, we must satisfy, in addition to the nulling condition in Eq. (3.13),

$$\sum_{j=1}^{N} A_j \sin 2\alpha_j L_j \cos(\delta_j - \varphi) = 0. \tag{3.16}$$

Since this condition should be fulfilled for all angles φ, Eq. (3.16) can be split into two different conditions

$$\sum_{j=1}^{N} A_j \sin 2\alpha_j L_j \cos\delta_j = 0, \tag{3.17a}$$

$$\sum_{j=1}^{N} A_j \sin 2\alpha_j L_j \sin\delta_j = 0. \tag{3.17b}$$

These conditions are different from the θ^4-conditions for other types of nulling interferometers [59]. However, we can show that, in the case of a three-telescope configuration, the only possible configuration to fulfill these conditions is a linear configuration, as it is the case for other nulling interferometers. For exoplanet detection, a linear configuration is less interesting because it only gives information in one direction. A solution to this

lack of information would be to rotate the whole array of telescopes but this would give rise to slow modulation, as explained in the next section. We can then conclude, that no interesting three-telescope configuration can fulfill the θ^4-conditions.

3.3.3 Modulation

As discussed in the previous section, the stellar leakage due to the finite size of the star could prevent us from directly detecting Earth-like exoplanets. If the star is on-axis, the stellar leakage should be rotationally symmetric. Another difficulty is the possible emission from exo-zodiacal dust near the orbital plane of the planet. We, a priori, do not know anything about the exo-zodiacal cloud. However, by analogy with our own solar system, we can assume that it is centro-symmetric.

Because of this central symmetry, both problems could be handled by using modulation techniques. A possible solution is to use external modulation, which consists in rotating the whole telescope array around its center, but this gives rise to very slow modulation and it will considerably decrease the number of targets that we can observe during a space mission. A more convenient solution is internal modulation. With this technique, we do not change the positions of the telescopes. Via optical means, we create different transmission maps that we combine in order to create modulation maps.

In the proposed design, we can change the "weight" of the amplitude A_j by changing the angle α_j. Thus, we can then change the ratio between the amplitudes of the different beams by simply rotating the waveplates, provided that the nulling condition in Eq. (3.13) is satisfied. This has two consequences: the first one is that, with this type of nulling interferometer, we do not need any extra amplitude-matching device, as it is the case in most of current nulling interferometers. The amplitude-matching is inherent to the design and is simply produced by a rotation of the waveplate; the second, and much more important, consequence is that since we can change the ratio between the amplitudes of the beams, we can have a continuous set of transmission maps, which could be used for fast modulation.

Figure 3.5 shows an example of a set of six transmission maps in the three-telescope case that have been obtained by only rotating the waveplates. In these transmission maps, the maximal intensity has been normalized to a value given by $\left(\sum_{j=1}^{N} |A_j/A_1 \sin 2\alpha_j|\right)^2$. Note that this is just an example out of a continuous range of transmission maps. Nevertheless, as shown in the next section, any of these transmission maps can be represented by a linear combination of three others. Therefore, three different transmission maps are sufficient to get the whole continuous set (for example, Figures 3.5(a), 3.5(c) and 3.5(e) or Figures 3.5(b), 3.5(d) and 3.5(f)).

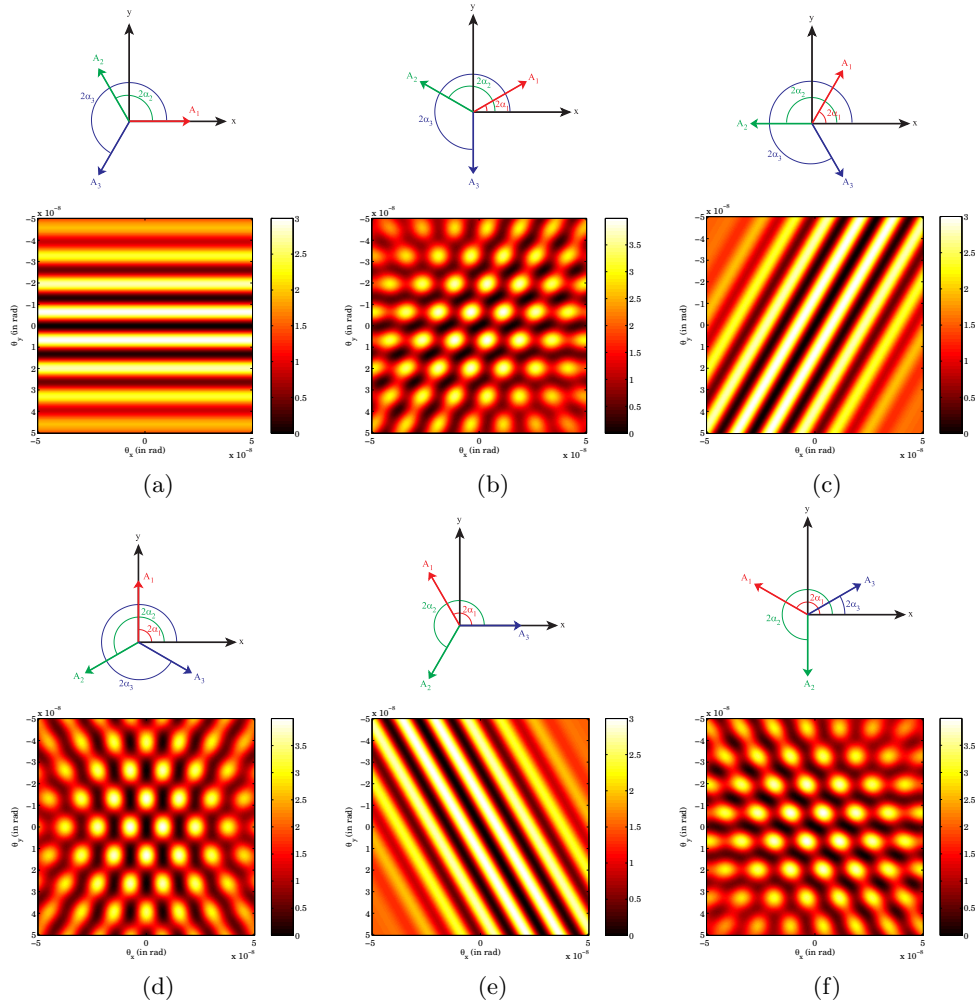

Figure 3.5: Simulated three-telescope transmission maps corresponding to different waveplate orientations. All these maps have been calculated with the following parameters: $A_1 = A_2 = A_3$, $L_1 = L_2 = L_3 = 25m$ and $\delta_1 = 0, \delta_2 = 2\pi/3, \delta_3 = 4\pi/3$, and for a spectral band going from 500 to 650nm. (a) $2\alpha_1 = 0, 2\alpha_2 = 2\pi/3, 2\alpha_3 = 4\pi/3$, (b) $2\alpha_1 = \pi/6, 2\alpha_2 = \pi/6 + 2\pi/3, 2\alpha_3 = \pi/6 + 4\pi/3$, (c) $2\alpha_1 = 2\pi/6, 2\alpha_2 = 2\pi/6 + 2\pi/3, 2\alpha_3 = 2\pi/6 + 4\pi/3$, (d) $2\alpha_1 = 3\pi/6, 2\alpha_2 = 3\pi/6 + 2\pi/3, 2\alpha_3 = 3\pi/6 + 4\pi/3$, (e) $2\alpha_1 = 4\pi/6, 2\alpha_2 = 4\pi/6 + 2\pi/3, 2\alpha_3 = 4\pi/6 + 4\pi/3$, (f) $2\alpha_1 = 5\pi/6, 2\alpha_2 = 5\pi/6 + 2\pi/3, 2\alpha_3 = 5\pi/6 + 4\pi/3$

3.3.4 Modulation maps and planet detection scheme

Consider three coplanar telescopes regularly spaced on a circle of radius L ($\delta_1 = 0$, $\delta_2 = 2\pi/3$ and $\delta_3 = 4\pi/3$). The three beams have equal amplitudes A, equal phases and in order to fulfill Eq. (3.13), the orientation of the j^{th} waveplate is chosen to be

$$2\alpha_j = \frac{2\pi}{3}(j-1) + \alpha, \tag{3.18}$$

where the angle α provides the modulation. The transmission map as a function of the angle α is given, within a constant factor, by

$$I_\alpha(kL\theta,\varphi) = \left| A\sum_{j=1}^{3}\left\{\sin\left[\frac{2\pi}{3}(j-1)+\alpha\right]\exp\left[ikL\theta\cos(\delta_j-\varphi)\right]\right\}\right|^2. \tag{3.19}$$

If we introduce the notations I_{12}, I_{13} and I_{23}, which, respectively, represent the two-beam transmission maps obtained with the first and the second beams, the first and the third beams and the second and the third beams,

$$I_{12}(kL\theta,\varphi) = 2A^2\left\{1-\cos\left[\sqrt{3}kL\theta\sin\left(\frac{\pi}{3}-\varphi\right)\right]\right\}, \tag{3.20a}$$

$$I_{13}(kL\theta,\varphi) = 2A^2\left\{1-\cos\left[\sqrt{3}kL\theta\sin\left(\frac{2\pi}{3}-\varphi\right)\right]\right\}, \tag{3.20b}$$

$$I_{23}(kL\theta,\varphi) = 2A^2\left\{1-\cos\left[\sqrt{3}kL\theta\sin\varphi\right]\right\}, \tag{3.20c}$$

we can easily rewrite the previous equation as

$$\begin{aligned} I_\alpha(kL\theta,\varphi) = \; & -\tfrac{1}{4}\left(\sqrt{3}\sin 2\alpha - 2\sin^2\alpha\right) I_{12}(kL\theta,\varphi) \\ & -\tfrac{1}{4}\left(-\sqrt{3}\sin 2\alpha - 2\sin^2\alpha\right) I_{13}(kL\theta,\varphi) \\ & -\tfrac{1}{4}\left(-3\cos^2\alpha + \sin^2\alpha\right) I_{23}(kL\theta,\varphi). \end{aligned} \tag{3.21}$$

Eq. (3.21) shows that, for all angles α, the transmission map I_α is a linear combination of the three transmission maps I_{12}, I_{13} and I_{23}. Rearranging the terms in Eq. (3.21), we find

$$\begin{aligned} I_\alpha(kL\theta,\varphi) = \; & \tfrac{1}{4}\left[I_{12}(kL\theta,\varphi) + I_{13}(kL\theta,\varphi) + I_{23}(kL\theta,\varphi)\right] \\ & +\tfrac{\sqrt{3}}{4}\sin 2\alpha\left[I_{13}(kL\theta,\varphi) - I_{12}(kL\theta,\varphi)\right] \\ & +\tfrac{1}{4}\cos 2\alpha\left[2I_{23}(kL\theta,\varphi) - I_{13}(kL\theta,\varphi) - I_{12}(kL\theta,\varphi)\right]. \end{aligned} \tag{3.22}$$

This can be re-written as

$$I_\alpha(kL\theta,\varphi) = I_M(kL\theta,\varphi) + A_M(kL\theta,\varphi)\sin\left[2\alpha + \Phi_M(kL\theta,\varphi)\right], \tag{3.23}$$

where $I_M(kL\theta,\varphi)$, $A_M(kL\theta,\varphi)$ and $\Phi_M(kL\theta,\varphi)$ are given by

$$I_M(kL\theta,\varphi) = \frac{1}{4}\left(I_{12} + I_{13} + I_{23}\right), \tag{3.24a}$$

$$A_M(kL\theta,\varphi) = \frac{1}{2}\sqrt{I_{12}^2 + I_{13}^2 + I_{23}^2 - I_{12}I_{23} - I_{12}I_{13} - I_{13}I_{23}}, \tag{3.24b}$$

$$\tan\Phi_M(kL\theta,\varphi) = \frac{2I_{23} - I_{12} - I_{13}}{\sqrt{3}\left(I_{13} - I_{12}\right)}, \tag{3.24c}$$

where the dependence $(kL\theta, \varphi)$ has been omitted for clarity. Therefore, for every point source in the sky, the modulation curve – the intensity as a function of the modulation angle α – will be a periodic function of period π. The modulation of the intensity corresponding to the point source $(kL\theta, \varphi)$ is characterized by a modulation phase Φ_M and a modulation depth μ_M,

$$\mu_M\left(kL\theta, \varphi\right) = \frac{\max\left(I_\alpha\right) - \min\left(I_\alpha\right)}{\max\left(I_\alpha\right) + \min\left(I_\alpha\right)} = \frac{A_M\left(kL\theta, \varphi\right)}{I_0\left(kL\theta, \varphi\right)}. \tag{3.25}$$

The modulation depth μ_M and the modulation phase Φ_M as a function of the generalized radial coordinate $kL\theta$ and the azimuthal coordinate φ are depicted in Figure 3.6.

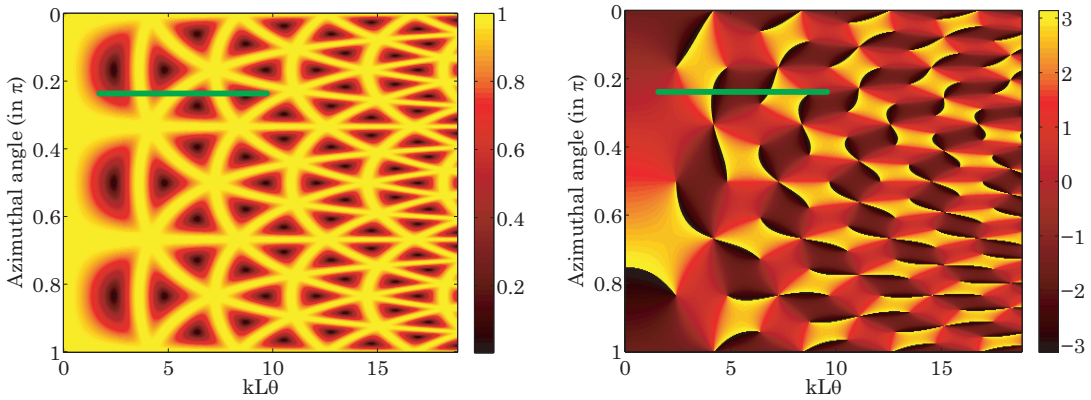

Figure 3.6: (a) Modulation depth $\mu_M\left(kL\theta, \varphi\right)$ and (b) modulation phase $\Phi_M\left(kL\theta, \varphi\right)$

Assume the three telescopes are observing a point-like star with a planet at the angular position (θ, φ). The modulated intensity can be recorded and a modulation depth and a modulation phase can be calculated. To this planet corresponds one single point on the modulation maps of Figure 3.6 and therefore cannot be differentiated from eventual sources of noise. However, the radial coordinate scales with the wavelength. Thus, if we use a spectrometer (which would be anyway needed for the study of the eventual atmosphere), the planet would be represented on Figure 3.6 by a horizontal segment going from $k_{\min}L\theta$ to $k_{\max}L\theta$ (see Figure 3.6). By comparison between the calculated modulation depth and phase and the theoretical modulation maps of Figure 3.6, the position of the planet can be found and the spectrum of the planet light can be derived.

Since the three transmission maps I_{12}, I_{13} and I_{23} are merely rotations of each other, their response to a rotationally symmetric source would be identical. Rotationally symmetric sources such as a finite-size star would not be modulated since the transmission map I_α is a linear combination of I_{12}, I_{13} and I_{23}. However, replacing φ by $\pi + \varphi$ in Eq. (3.20) and Eq. (3.21), we can see that the transmission map I_α is centro-symmetric. We therefore could not differentiate between two centro-symmetric point sources. Light coming from a centro-symmetric exo-zodiacal cloud would be modulated together with the planet

light. It is possible to coherently combine two different transmission maps to create a non-symmetric modulation map but further investigations are needed to find still other strategies.

An additional problem would be the presence of instability noise or variability noise. This noise is due to time-depending amplitude or phase instabilities in the interferometer such as optical path difference, tip-tilt, fringe tracking offset, defocus, etc. In this proposed approach, we can see that such an instability noise would also be modulated. Some techniques have been developed to get rid of instability noise by pre-filtering [60] or by calibration [61]. But further studies are needed to know whether these techniques are viable in our case.

3.4 Spectral response

In some applications, besides the detection of an Earth-like exoplanet, spectral information of the light coming from the planet is needed in order to study its atmosphere. In this case, the wide spectral band is required anyhow, not only for photon collection efficiency.

In the proposed design, if we make the assumption of perfect polarizers and exactly identical waveplates, there is absolutely nothing in the nulling condition of Eq. (3.13) that limits the spectral band, so a high rejection ratio in an infinitely-wide spectral band is not unthinkable. However, in practice, this is not true since polarizers and waveplates are not perfect and are spectrally limited. Furthermore, as we will see in this section, the response of the interferometer is not the same for all wavelengths, that is, the detected intensity is wavelength-dependent.

If we assume identical waveplates for each beam, the detected intensity will be proportional to

$$I \propto |T_r - T_\alpha|^2 , \tag{3.26}$$

independently of the optical path length differences between the beams. The intensity for the constructive interference is then also proportional to Eq. (3.26), which, in the case of a perfect waveplate is proportional to

$$I \propto |1 - \exp(i\Delta\phi)|^2 = 4\sin^2\frac{\Delta\phi}{2}, \tag{3.27}$$

where $\Delta\phi$ is the phase difference between the two eigenstates of polarization induced by the waveplate. If we furthermore consider conventional waveplates (as opposed to achromatic waveplates), we have

$$\Delta\phi = \frac{2\pi}{\lambda}\left[n_e(\lambda) - n_o(\lambda)\right] d = \frac{2\pi}{\lambda} B(\lambda) , \tag{3.28}$$

where λ is the wavelength, $n_e(\lambda)$ and $n_o(\lambda)$ are the extraordinary and ordinary refractive indices, d is the thickness and $B(\lambda)$ is the birefringence of the waveplate.

The intensity is then maximum for $\Delta\phi = (2n+1)\,\pi$ (half-wave plate) and equal to zero for $\Delta\phi = 2n\pi$, where n is an integer representing the order of the waveplate. This shows that some wavelengths will be well transmitted to the detector, while others will not be transmitted at all.

The criterion that we chose to define as the *acceptable spectral band* is then that all the wavelengths should be transmitted with at least half the maximal intensity, which leads to the following condition

$$(4n+1)\,\frac{\pi}{2} \leq \Delta\phi = \frac{2\pi}{\lambda} B\,(\lambda) \leq (4n+3)\,\frac{\pi}{2}, \tag{3.29}$$

We assume that the birefringence is constant in the spectral band. This is not a very realistic assumption but we can show, in the example of quartz, that it does not drastically affect the criterion. In Figure 3.7, we compare the spectral response of the interferometer in the visible domain in the case of quartz waveplates and in the case of constant-birefringence approximation. We can see that the approximation is not very good but in both cases, the acceptable spectral band is of the same order of magnitude. Furthermore, the birefringence is chosen in such a way that the waveplate is a half-wave plate for the wavelength λ_0. We then have

$$B = (2n+1)\,\frac{\lambda_0}{2}. \tag{3.30}$$

The minimal and maximal wavelengths in the acceptable spectral band are then given by

$$\lambda_{min} = \frac{4n+2}{4n+3}\lambda_0 \quad \text{and} \quad \lambda_{max} = \frac{4n+2}{4n+1}\lambda_0. \tag{3.31}$$

We can characterize the bandwidth by defining

$$M = \frac{\lambda_{max}}{\lambda_{min}} = \frac{4n+3}{4n+1}. \tag{3.32}$$

We can see that the bandwidth is maximum if we use zero-order waveplates ($n = 0$), which in this case gives $M = 3$. For example, in the infrared region, this technique would allow us to work from 6 to 18 μm. The spectral band will then probably be limited by the polarizers. Obviously, the acceptable spectral band can be wider if we use achromatic waveplates (see Figure 3.7).

Important remark: The presence of polarizers does not necessarily imply losses if we use achromatic waveplates and a polarizing beam splitter to separate the two orthogonal states of polarization and use both of them in a similar set-up.

3.5 Sensitivity to imperfections and misalignments

In this section, we will see how sensitive the proposed set-up is with respect to misalignments and imperfections and how these defects affect the rejection ratio.

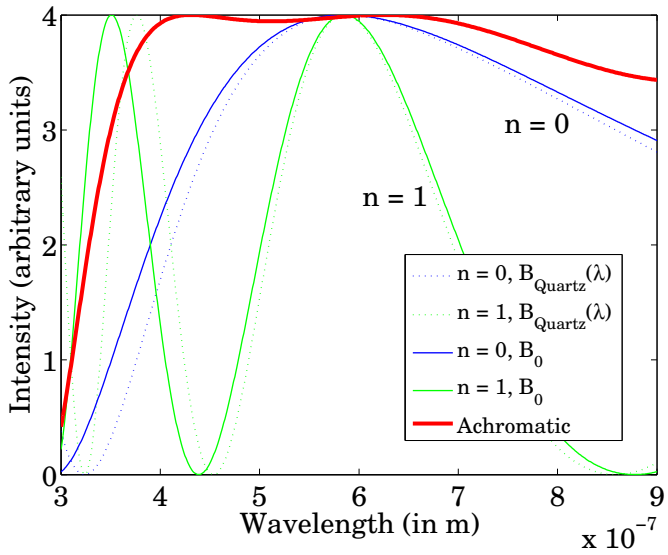

Figure 3.7: Spectral response of the interferometer in the visible domain in the case of quartz waveplates (dotted lines) and in the case of constant-birefringence approximation (solid lines). We also compare zeroth-order (dark lines) and first-order (light-grey lines) waveplates. The thick solid line represents the spectral response in the case of an achromatic waveplate made of a combination of quartz and magnesium fluoride.

Let us first derive a general expression for the on-axis detected intensity. We assume that each polarizer could have its own imperfection, that is its own extinction ratio, $\epsilon_{k,j}$, $k = 1$ or 2 ($\epsilon_{k,j}$ represents the imperfection of the first or second polarizer for the j^{th} beam) and that each waveplate could be different for each beam ($T_{r,j}$ and $T_{\alpha,j}$). The amplitude of the j^{th} beam is given by

$$\vec{A_j} = A_j \begin{pmatrix} \epsilon_{2,j} & 0 \\ 0 & 1 \end{pmatrix} \begin{pmatrix} T_{r,j}\cos^2\alpha_j + T_{\alpha,j}\sin^2\alpha_j & \frac{1}{2}\sin 2\alpha_j\,(T_{r,j} - T_{\alpha,j}) \\ \frac{1}{2}\sin 2\alpha_j\,(T_{r,j} - T_{\alpha,j}) & T_{r,j}\sin^2\alpha_j + T_{\alpha,j}\cos^2\alpha_j \end{pmatrix} \begin{pmatrix} 1 \\ \epsilon_{1,j} \end{pmatrix}. \tag{3.33}$$

After some calculations, we find that the on-axis detected intensity is given by

$$\begin{aligned} I_\lambda \;&= \left| \sum_{j=1}^{N} A_j \epsilon_{2,j} \left[T_{r,j}\cos^2\alpha_j + T_{\alpha,j}\sin^2\alpha_j + \frac{1}{2}\epsilon_{1,j}\sin 2\alpha_j\,(T_{r,j} - T_{\alpha,j}) \right] \right|^2 \\ &+ \left| \sum_{j=1}^{N} A_j \left[\frac{1}{2}\sin 2\alpha_j\,(T_{r,j} - T_{\alpha,j}) + \epsilon_{1,j}\left(T_{r,j}\sin^2\alpha_j + T_{\alpha,j}\cos^2\alpha_j\right) \right] \right|^2 . \end{aligned} \tag{3.34}$$

Hereafter, we will analyze each defect separately. For all simulations, we used the following

parameters for the perfect case

$$\begin{gathered} A_1 = A_2 = A_3 = 1, \\ 2\alpha_1 = \tfrac{7\pi}{6}, 2\alpha_2 = \tfrac{11\pi}{6}, 2\alpha_3 = \tfrac{\pi}{2}, \\ \epsilon_{1,1} = \epsilon_{1,2} = \epsilon_{1,3} = 0, \\ \epsilon_{2,1} = \epsilon_{2,2} = \epsilon_{2,3} = 0, \\ T_{r,1} = T_{r,2} = T_{r,3} = T_r = 1, \\ T_{\alpha,1} = T_{\alpha,2} = T_{\alpha,3} = T_\alpha = \exp\left(i5\pi\lambda_0/\lambda\right), \\ \lambda_{min} = 500nm, \lambda_{max} = 650nm, \lambda_0 = 562nm. \end{gathered} \tag{3.35}$$

3.5.1 Amplitude and phase mismatchings

Let us first consider an amplitude mismatching $A_l = A_{l,0} + \delta A_l$. We can show that the on-axis detected intensity is then given by

$$I_\lambda = \left|\delta A_l \sin 2\alpha_l\right|^2 \frac{\left(T_r - T_\alpha\right)^2}{4} \propto \left|\delta A_l\right|^2. \tag{3.36}$$

The rejection ratio obtained with an amplitude mismatching for the first beam is depicted in Figure 3.8. The amplitude mismatching should be of the order of 4 10^{-3} or lower in order to have a rejection ratio of 10^6.

If we consider now a phase mismatching $A_l = A_{l,0}\exp\left(i\delta\phi_l\right)$, we will find a similar expression for the on-axis intensity,

$$I_\lambda = \left|\delta\phi_l \sin 2\alpha_l\right|^2 \frac{\left(T_r - T_\alpha\right)^2}{4} \propto \left|\delta\phi_l\right|^2. \tag{3.37}$$

We can then draw the same conclusion for the rejection ratio (not depicted here since it is identical to the rejection ratio obtained with an amplitude mismatching). The phase mismatching should be lower than 4 10^{-3}, which corresponds to an optical path difference lower than $\lambda/2000$. This means that, in the visible domain, optical path differences should be corrected within 0.2 nm, while they should only be compensated within 3 nm in the mid-IR.

3.5.2 Polarization mismatching

In principle, each telescope (and each optical component until the interferometer) will induce amplitude, phase and polarization defects that will decrease the performances of the interferometer. However, if we assume perfect polarizers, all polarization defects will be translated in terms of amplitude and phase mismatchings. This leads to the following tolerance: the phase difference between the two states of polarization should be identical for all beams within 1 mrad and the amplitude ratio between the two states of polarization should be identical for all beams within 10^{-3}. The case of non-perfect polarizers is considered in the next section.

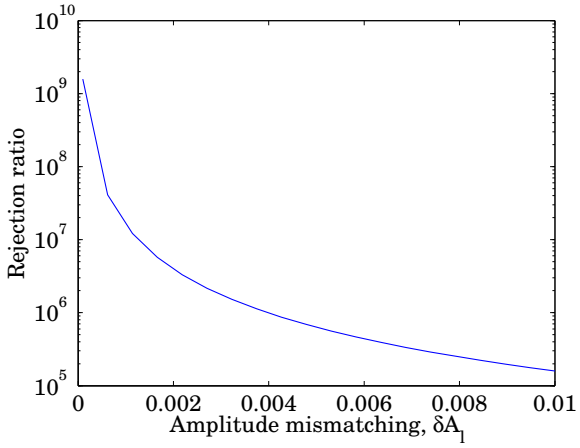

Figure 3.8: Rejection ratio as a function of an amplitude-mismatching δA_1

3.5.3 Rotation of the polarizers

Each beam goes through two different polarizers (one horizontal and one vertical). Differences in the orientation of these polarizers result in a deterioration of the rejection ratio.

Let us first consider the case of the second polarizer (vertical). Assume that, in all beams, the second polarizer is vertical except for one beam, for which the polarizer makes a small angle β with the y-axis. This beam will have a polarization slightly rotated compared to the other beams and therefore, they cannot interfere perfectly. The on-axis detected intensity will be proportional to the square of the rotation angle β [62],

$$I \propto \beta^2. \tag{3.38}$$

The case of the first horizontal polarizer is fundamentally different. Consider two unpolarized beams. These two beams can interfere perfectly if they encounter polarizers with identical orientations (or if there is no polarizer at all). However, if the two polarizers do not have the same orientation, both incoherent states of polarization will be mixed and the beams cannot interfere with a perfect contrast, even though an additional device is used to match the polarization orientation. In this case, the degradation of the rejection ratio is not due to a polarization mismatching between the interfering beams but is due to the incoherence of the two orthogonal states of polarization. We can show that, in this case, the on-axis detected intensity would still be proportional to the square of the angle β between the polarizers.

In order to reach a rejection ratio of 10^6, the orientation of the polarizers should be accurate within 1 mrad. Note that the orientation of the last polarizers (vertical) can be identical for all beams by using one single polarizer after beam recombination (in the case of a uni-axial beam combiner).

3.5.4 Imperfections of the polarizers

Imperfections of the polarizers are modeled by setting $\epsilon_{1,j}$ and $\epsilon_{2,j}$ different from zero. These numbers can be complex, giving rise to a certain ellipticity in the polarization state.

We chose all the $\epsilon_{1,j}$ and $\epsilon_{2,j}$ in such a way that their moduli are a random number between 0 and 10^{-3} and the phases are also randomly chosen. We then looked at the average rejection ratio that can be obtained. The results are plotted in Figure 3.9.

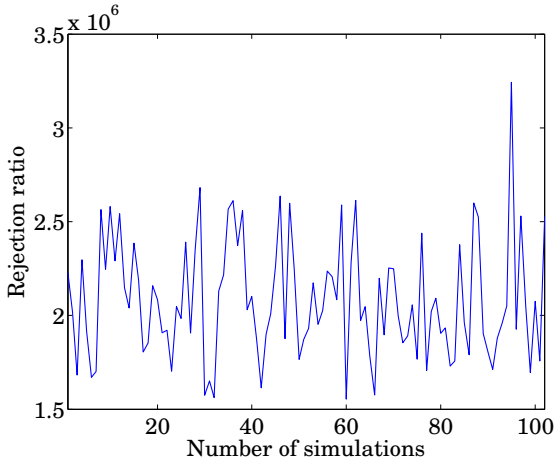

Figure 3.9: Rejection ratio with randomly-chosen $\epsilon_{1,j}$ and $\epsilon_{2,j}$.

The rejection ratio is in average slightly higher than 10^6. The "amplitude imperfections" of the polarizers should then also be of the order of 10^{-3}, which is not easy to satisfy in a wide spectral band. Note that this requirement is less stringent if we use achromatic waveplates instead of conventional waveplates. Indeed, if we consider identical quasi-achromatic waveplates ($T_{\alpha,1} = T_{\alpha,2} = T_{\alpha,3} = T_\alpha = \exp(i(\pi + \delta))$, where $\delta << \pi$) and identical imperfect polarizers ($\epsilon_{1,1} = \epsilon_{1,2} = \epsilon_{1,3} = \epsilon_{2,1} = \epsilon_{2,2} = \epsilon_{2,3} = \epsilon << 1$), we can show that the on-axis intensity is then proportional to

$$I \propto (\epsilon\delta)^2, \tag{3.39}$$

which shows that imperfections of the polarizers can be compensated by very achromatic waveplates and inversely, chromatic waveplates can be used combined with very good polarizers. Note that, in reality, it remains challenging to manufacture polarizers and waveplates that are sufficiently good in the whole spectral band.

3.5.5 Rotation of the waveplates

We consider a small additional angle in the rotation of the l^{th} waveplate having $\alpha_l = \alpha_{l,0} + \delta\alpha_l$. After some calculations, we find

$$I_\lambda = |T_r - T_\alpha|^2 \left| A_l \left(\delta\alpha_l \cos 2\alpha_l - \delta\alpha_l^2 \sin 2\alpha_l \right) \right|^2. \tag{3.40}$$

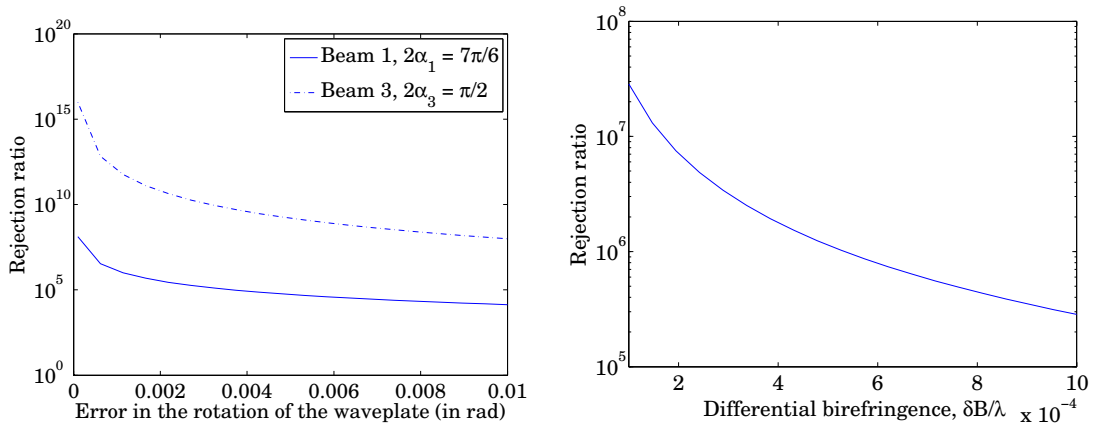

(a) (b)

Figure 3.10: (a) Rejection ratio when one of the waveplates is rotated with respect to its normal position for $2\alpha_1 = 7\pi/6$ (solid line) and $2\alpha_3 = \pi/2$ (dash-dot line) and (b) rejection ratio with a differential birefringence δB in the third beam.

This shows that the rejection ratio will be much less sensitive to waveplate rotations if $\cos 2\alpha_l = 0$, as shown in Figure 3.10(a). In the worst case ($\cos 2\alpha_l = 1$), the rotation of the waveplate should be accurate within 1 mrad to reach a rejection ratio of 10^6. In all cases, the required accuracy in waveplate rotation should not be the limiting factor in an actual set-up.

3.5.6 Differential birefringence

Suppose that the birefringence of the l^{th} waveplate is slightly different from the birefringence of the other waveplates, $B_l = B_0 + \delta B$. The detected intensity is then given by

$$I_\lambda = \left| A_l \sin 2\alpha_l \frac{\pi \delta B}{\lambda} \right|^2 . \tag{3.41}$$

As shown in Figure 3.10(b), we should have $\delta B/\lambda \leq 5 \times 10^{-4}$ in order to have a rejection ratio higher than 10^6, which should be easier to reach in the infrared ($\delta B \leq 3$ nm) than in the visible ($\delta B \leq 0.2$ nm) region of the spectrum.

3.6 N-beam interferometer

We treated the case of three-beam interferometer in detail since our table-top experimental set-up consists of three beams. However, although out of the scope of this chapter, the concepts presented here can be invariably applied to N beams.

3.7 Conclusions

We have derived an expression for the generalized N-beam nulling condition, which includes amplitude, phase and polarization. We have applied this condition to the cases of a two- and a three-beam nulling interferometer. We have shown that interferometry with beams with different coherent states of polarization is possible with a theoretically perfect contrast.

We have seen that we can theoretically reach an infinite rejection ratio in the monochromatic case without any phase shifter, using only polarization rotation. In a wide spectral band, we can still have a high rejection ratio without any phase shifter, but we need an extra device, which could be an achromatic polarization rotator. The approach we show involves only off-the-shelf elements: linear polarizers and waveplates. We thus have introduced a totally new type of nulling interferometers, which should allow a high rejection ratio, without any achromatic device. We have derived an expression for the nulling condition of the newly-designed nulling interferometer, which can be fulfilled by rotating waveplates only.

We have looked at the θ-dependence of the transmission map and have seen that, as in regular nulling interferometers, the only three-telescope configuration to have a θ^4-transmission map is the linear configuration, which is not very interesting for exoplanet detection. However, an advantage of the proposed design is that it does not need any amplitude-matching device and it is also very suitable for fast internal modulation. Indeed, it allows to obtain a continuous set of transmission maps by simple rotation of the waveplates.

Another interesting aspect of our analysis is that there is no theoretical limit for the width of the spectral band for which we can reach a deep null. However, the transmission is not equal for all wavelengths. We have established a criterion to define the acceptable spectral band in such a way that the transmission over the whole spectral band is higher than half the maximal transmission. We have seen that this criterion could lead to a relatively wide band in the infrared. The ultimate limit of the spectral band will probably be set by the transmission of the linear polarizers and the waveplates.

In order to complete the analysis, we also have looked at the sensitivity of the proposed design to some imperfections and misalignments. We have seen that the factor limiting the rejection ratio will probably be the imperfections of the polarizers and not their angular settings. Indeed, rotations can be reached very accurately. Phase mismatching and differential birefringence can be a problem in the visible region but are less important in the infrared. In conclusion, using the approach presented in this chapter, we have shown that it should be possible to reach a high rejection ratio without any achromatic device, thus opening a new promising way to detect Earth-like exoplanets.

Chapter 4

Compensation or optimization of dispersion

Dispersion is the dependence of the refractive index with respect to the wavelength. In white light interferometry and especially in nulling interferometry, dispersion might be of great importance since all interfering beams will pass through different optics and might therefore acquire different wavelength-dependent phases. These different phases will affect the performance of the interferometer.

Dispersion can be compensated for by adding some extra path lengths in glass. On the other hand, as we will see in this chapter, dispersion could also lead to better performance of the interferometer and therefore could be used or optimized to reach a higher rejection ratio.

In Section 4.1, we analyze the effect of dispersion on the interference patterns and on the rejection ratio in the case of N-beam nulling interferometers ($N \leq 6$). In Section 4.2, we discuss in which cases dispersion should be compensated for or optimized. Our conclusions are then summarized in Section 4.3.

4.1 Theory and simulations

In this section, we will see how dispersion can affect the performance of a general nulling interferometer. The cases of two- and three-beam interferometers will be analyzed separately.

4.1.1 Two-beam interferometer

We consider two beams of amplitudes $a_1(\lambda)$ and $a_2(\lambda)$, with a phase difference $\Delta\phi$ and an optical path difference L between the two beams. Their complex amplitudes are given

by

$$A_1(\lambda, L) = a_1(\lambda) \exp(i\Delta\phi), \tag{4.1a}$$

$$A_2(\lambda, L) = a_2(\lambda) \exp\left(i\frac{2\pi}{\lambda}L\right). \tag{4.1b}$$

If the second beam goes through an extra glass plate of thickness d and of refractive index $n(\lambda)$, we have

$$A_1(\lambda, L) = a_1(\lambda) \exp(i\Delta\phi), \tag{4.2a}$$

$$A_2(\lambda, L) = a_2(\lambda) \exp\left\{i\frac{2\pi}{\lambda}[L + n(\lambda) d]\right\}. \tag{4.2b}$$

For a given thickness d, the intensity as a function of the optical path difference L is given by

$$I(L) = \int \left| a_1(\lambda) \exp(i\Delta\phi) + a_2(\lambda) \exp\left\{i\frac{2\pi}{\lambda}[L + n(\lambda) d]\right\}\right|^2 d\lambda. \tag{4.3}$$

Nulling without achromatic phase shifter

Let us assume that there is no additional phase difference between the beams ($\Delta\phi = 0$). Furthermore, we assume that the beams have equal amplitudes ($a_1(\lambda) = a_2(\lambda) = a(\lambda)$). We have

$$\begin{aligned} I(L) &= \int |a(\lambda)|^2 \left|1 + \exp\left\{i\frac{2\pi}{\lambda}[L + n(\lambda) d]\right\}\right|^2 d\lambda \\ &= 4\int |a(\lambda)|^2 \cos^2\left\{\frac{\pi}{\lambda}[L + n(\lambda) d]\right\} d\lambda. \end{aligned} \tag{4.4}$$

In our simulations, we chose the refractive index of BK7 and for the amplitude $a(\lambda)$, we used the spectrum of the lamp used in our experimental set-up (see Section 6.1.4). Interference patterns corresponding to different thicknesses $d = 0, 4.8, 9.6$ and 14.4 μm are depicted in Figure 4.1(a)-(d) respectively. When there is no additional glass plate (Figure 4.1(a)), the pattern is symmetric with respect to the zero-OPD position ($I(L) = I(-L)$). As the thickness of the additional glass plate increases to $d = 4.8$ μm (Figure 4.1(b)), the fringes become asymmetric. For further increase of the plate thickness (Figure 4.1(c), $d = 9.6$ μm) the fringes become quasi-symmetric with respect to the minimum of the interference pattern. Finally, as the thickness gets larger (Figure 4.1(d)), the fringes become again asymmetric.

The rejection ratio is defined as the ratio between the maximal and the minimal intensities,

$$R = \frac{\max(I(L))}{\min(I(L))}. \tag{4.5}$$

The rejection ratio as a function of the thickness d of the glass plate is depicted in Figure 4.2(a) (solid line). Note that negative values of the thickness d physically mean that the glass plate has been introduced in the first beam instead of the second one. We can see

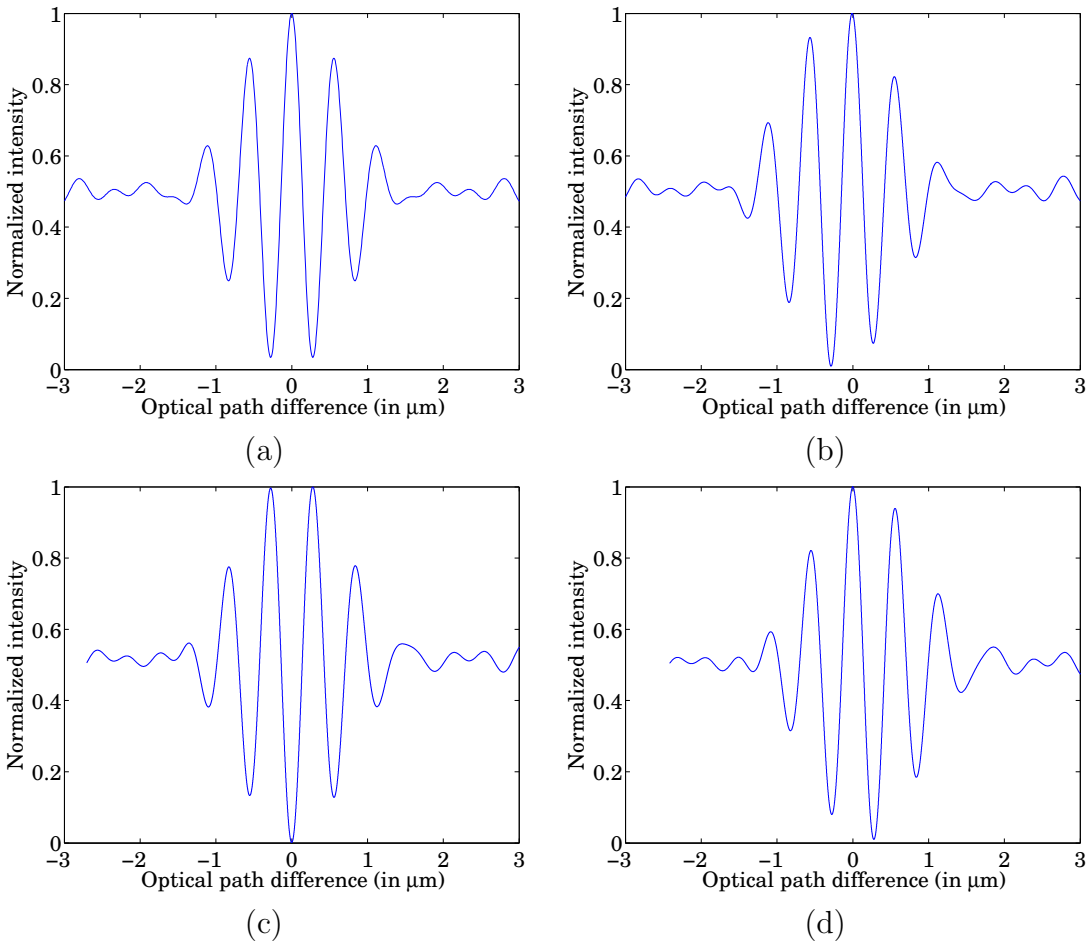

Figure 4.1: Interference patterns corresponding to different thicknesses of the glass plate: (a) $d = 0\mu$m, (b) $d = 4.8\mu$m, (c) $d = 9.6\mu$m and (d) $d = 14.4\mu$m.

that the rejection ratio is minimal when there is no glass plate ($d = 0$ μm) and is maximal when the thickness of the glass plate is around 9.6 μm. The rejection ratios corresponding to the fringes of Figure 4.1 are marked by the four dots in Figure 4.2(a). We can also see on Figure 4.2(a) (dash-dotted line) the rejection ratio when the two beams have slightly different spectra (see Section 6.1.4). In this case, the rejection ratio has the same overall shape but the values are somewhat lower.

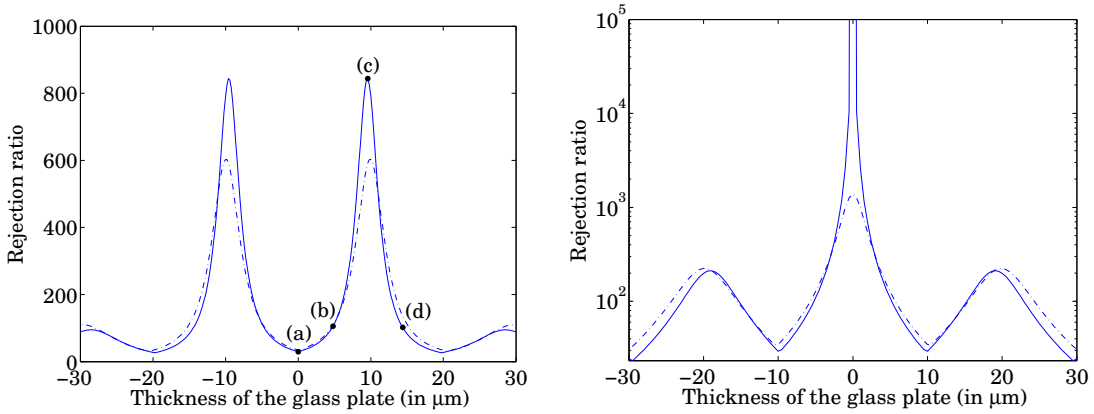

(a) (b)

Figure 4.2: Rejection ratio as a function of the thickness of the introduced glass plate (a) when there is no phase difference and (b) when there is a π phase difference between the beams. For the solid lines, the spectrum of the two beams are identical and equal to the spectrum of the Xe lamp used in our experimental set-up (see Section 6.1.4) and for the dash-dotted lines, the spectra of the beams are slightly different leading to a lower rejection ratio (see Section 6.1.4).

In order to understand why there is a peak in the rejection ratio, let us look at the phase difference between the two beams,

$$\Phi_2(\lambda) = \Phi_1(\lambda) + \frac{2\pi}{\lambda} L + \frac{2\pi}{\lambda} n(\lambda)\, d. \tag{4.6}$$

If we express the refractive index in a power series,

$$n(\lambda) = \sum_{j=0}^{\infty} \alpha_j \lambda^j, \tag{4.7}$$

we have

$$\Phi_2(\lambda) = \Phi_1(\lambda) + \frac{2\pi}{\lambda} L + \frac{2\pi}{\lambda} \alpha_0 d + \frac{2\pi}{\lambda} \alpha_1 \lambda d + \underbrace{\frac{2\pi}{\lambda} \sum_{j=2}^{\infty} \alpha_j \lambda^j}_{\mathcal{O}(\lambda)}. \tag{4.8}$$

After compensating for the optical path difference ($L = -\alpha_0 d$) and choosing the right thickness of the glass plate ($d = 1/2\alpha_1$), we find

$$\Phi_2(\lambda) = \Phi_1(\lambda) + \pi + \mathcal{O}(\lambda). \tag{4.9}$$

In this case, the glass plate acts therefore as a first-order achromatic phase-shifter. Indeed, the fringes corresponding to the maximal rejection ratio (see Figure 4.1(c)) are very similar to the one that would be obtained with an achromatic phase shifter.

Nulling with an achromatic phase shift of π

Consider an additional π phase difference between the beams ($\Delta\phi = \pi$). The rejection ratio as a function of the glass thickness d is depicted in Figure 4.2(b). The solid line is the rejection ratio for two beams with identical spectra. The rejection ratio is infinite when there is no dispersion because of the perfectly achromatic π phase shift. We can see that the rejection ratio is now minimal around $d = 10\mu$m, where the rejection ratio of Figure 4.2(a) was maximal. Dispersion will therefore degrade the performances of such a nulling interferometer.

We now consider the same spectral mismatching between the beams as in of Figure 4.2(a) (dash-dotted line). We can see that the rejection ratio has a similar shape but is now drastically limited (to 10^3) in the case of no dispersion (Figure 4.2(b) dash-dotted line).

4.1.2 Three-beam interferometer

In this section, we consider three beams of amplitudes $a_1(\lambda)$, $a_2(\lambda)$ and $a_3(\lambda)$ and no achromatic phase shift between the beams. The complex amplitudes of the beams are given by

$$A_1(\lambda, L_{21}, L_{31}) = a_1(\lambda), \tag{4.10a}$$

$$A_2(\lambda, L_{21}, L_{31}) = a_2(\lambda) \exp\left\{ i\frac{2\pi}{\lambda} \left[L_{21} + n(\lambda) d_2 \right] \right\}, \tag{4.10b}$$

$$A_3(\lambda, L_{21}, L_{31}) = a_3(\lambda) \exp\left\{ i\frac{2\pi}{\lambda} \left[L_{31} + n(\lambda) d_3 \right] \right\}, \tag{4.10c}$$

where L_{21} and L_{31} are, respectively, the optical path differences between the second and the first beams and between the third and the first beams. d_2 and d_3 are respectively the thicknesses of the glass plates of refractive index $n(\lambda)$ inserted in the second and the third beams.

For given thicknesses d_2 and d_3, the intensity as a function of the optical path differences L_{21} and L_{31} is given by

$$I(L_{21}, L_{31}) = \int \left| \sum_{j=1}^{3} A_j(\lambda, L_{21}, L_{31}) \right|^2 d\lambda. \tag{4.11}$$

In this section, we will study two configurations: in the first one, all beams have identical amplitudes ((1-1-1) amplitude distribution) and in the second configuration, one beam has twice the amplitude of each of the two other beams ((1-2-1) amplitude distribution). In both configurations, the rejection ratio is optimal when the phase of the third beam is twice the phase of the second beam [53, 59]. We can therefore reduce the dimensionality of the problem by using

$$L_{31} = 2L_{21}, \tag{4.12a}$$

$$d_3 = 2d_2. \tag{4.12b}$$

From these intensities, we can calculate the rejection ratio as a function of the thickness of the glass plate d_2. The rejection ratios for the amplitude distributions (1-1-1) and (1-2-1) are depicted in Figure 4.3(a) and Figure 4.3(b), respectivelty. In both cases, the rejection ratio is minimal when there is no dispersion. For the (1-1-1) amplitude ratio, the maximal rejection ratio takes place at $d_2 = 6.4$ μm, which corresponds to a quasi-achromatic phase shift of $2\pi/3$. In the case of the (1-2-1) amplitude distribution, a rejection ratio larger than 10^5 could be reached using the glass plates as first-order achromatic phase shifters. Note that when the amplitude ratio is (1-2-1), the maximal rejection ratio reaches 2.10^5. It can be increased by a factor of 2-3 using the optimal constant amplitude defined in Chapter 2.

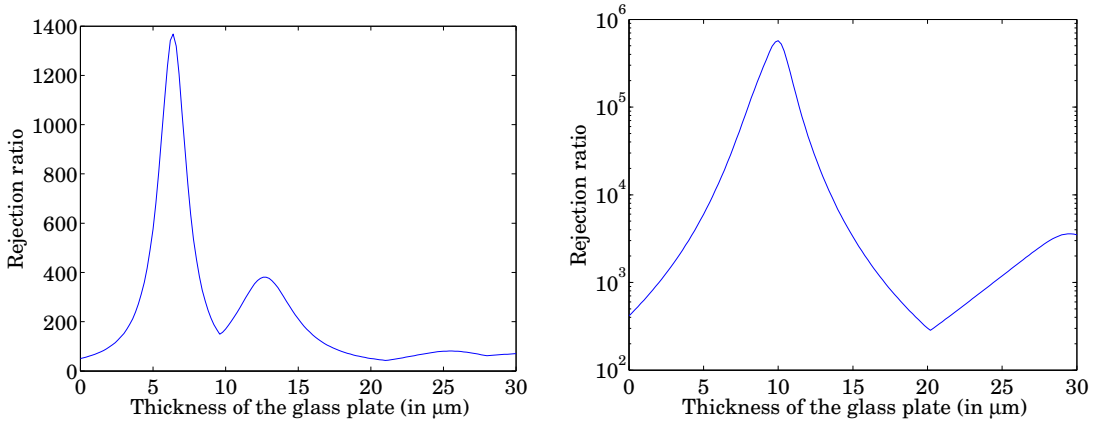

(a) (b)

Figure 4.3: Rejection ratio as a function of the thickness of the glass plate d_2 in the case of (a) (1-1-1) and (b) (1-2-1) amplitude distributions. For optimal performance, the thickness of the glass plate in the third beam is chosen to be $d_3 = 2d_2$.

4.1.3 N-beam interferometers

Since the number of telescopes for the Darwin mission changed from six to three and currently to four, it is important to study the influence of the number of beams on the rejection ratio. In this section, we will consider N-beam interferometers ($N \leq 6$) without achromatic phase shifter. We will also analyze the influence of the spectral bandwidth.

Consider N beams with amplitudes A_j and desired phases ϕ_j given by

$$\begin{aligned} A_j &= \begin{pmatrix} N-1 \\ j-1 \end{pmatrix}, \\ \phi_j &= (j-1)\,\tfrac{2\pi}{N}. \end{aligned} \tag{4.13}$$

These amplitudes and phases, summarized in Table 4.1 for $N \leq 6$, were proposed by Mieremet [53] in order to lower the requirements in terms of achromaticity. Indeed, given a certain phase shift error introduced by the phase shifter, this family of interferometers leads to the optimal rejection ratio.

N	$\mathbf{A_1 \cdots A_N}$	$\phi_1 \cdots \phi_N$
2	1 1	0 π
3	1 2 1	0 π 2π
4	1 3 3 1	0 π 2π 3π
5	1 4 6 4 1	0 π 2π 3π 4π
6	1 5 10 10 5 1	0 π 2π 3π 4π 5π

Table 4.1: Values of the amplitudes A_j and phases ϕ_j for $N \leq 6$.

Each beam goes through a glass plate, which thickness is optimally chosen to attain as closely as possible the desired phase in the whole spectral band. The spectrum of the beams is arbitrarily chosen to be a top-hat function with a normalized bandwidth $B = \lambda_{max}/\lambda_{min}$. In the visible region and in the near-IR (from 0.4 μm to 1 μm), we consider glass plates made out of BK7, while in the mid-IR (from 6 μm to 18 μm), we chose CsI as a material for the plates.

We can see on Figure 4.4(a) and Figure 4.4(b) the rejection ratio as a function of the normalized bandwidth B for N beams ($N \leq 6$). In the visible, we see that a rejection ratio of 10^5 is possible with a spectral bandwidth $B = 2.4$ or even wider with four telescopes. A rejection ratio of 10^6 in a broad band with BK7 plates is only possible with a five-beam interferometer. However, although this case is interesting from an experimental point of view, we are mainly interested in the mid-IR region (see Figure 4.4(b)). We see that a rejection ratio higher than 10^6 is possible in the whole $6 - 18$ μm spectral band ($B = 3$) with only four beams. With three beams, a rejection ratio nearly as high as 10^5 can be reached.

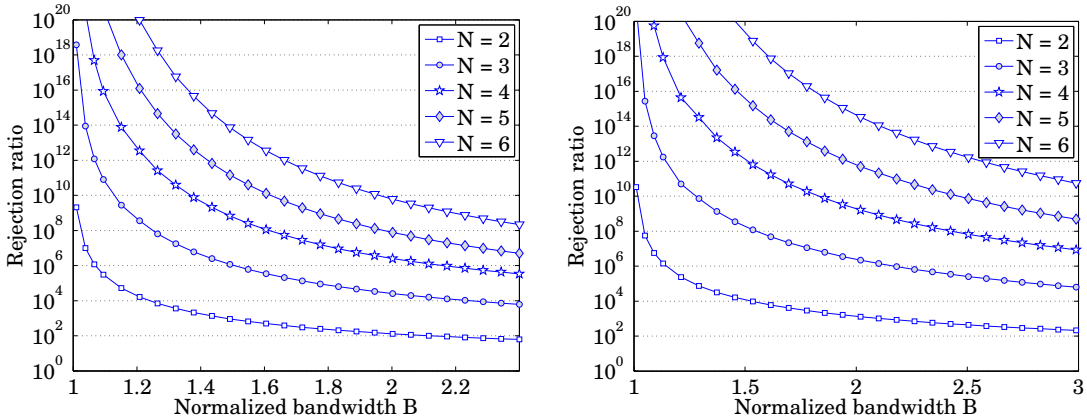

Figure 4.4: Rejection ratio as a function of the normalized bandwidth $B = \lambda_{max}/\lambda_{min}$ for $N \leq 6$ (a) in the visible domain and in the near-IR (from 0.4 μm to 1 μm, BK7) and (b) in the mid-IR (from 6 μm to 18 μm, CsI).

In the mid-IR, we chose CsI plates because of the transmission of this material in this spectral band and because of its quasi-linear refractive index. However, other materials can be considered. In Figure 4.5, we show the rejection ratio for a spectral band from 6 μm to 18 μm ($B = 3$) for N beams ($N \leq 6$) for a few materials that are transparent in

the mid-IR. We see that the material leading to the highest rejection ratio is CdTe. This material would allow a rejection ratio of 10^7 in the whole $6-18$ μm spectral band with four beams and a rejection ratio of 10^5 with three beams.

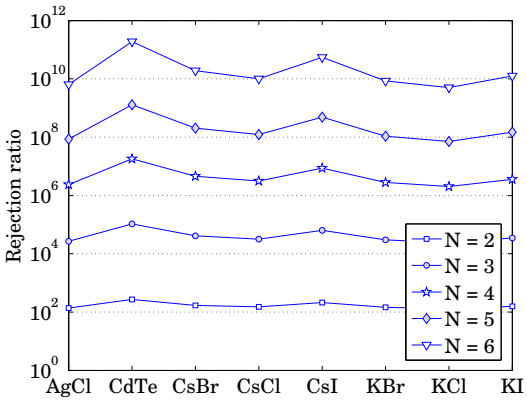

Figure 4.5: Rejection ratio as a function of the chosen material in a spectral band from 6 μm to 18 μm ($B = 3$) for $N \leq 6$.

4.2 Compensation or optimization

We have seen in the previous section that the performance of the interferometer strongly depend on dispersion. Therefore, we should wonder whether dispersion should be *compensated* for or *used* for optimal performances.

When no achromatic phase shifter is present in the set-up, changing the dispersion can lead to a drastic increase in the rejection ratio. Indeed, we have seen that the rejection ratio without dispersion was minimal, while dispersion can lead to a rejection ratio orders of magnitude larger. If we aim for the highest rejection ratio, one may conclude that additional dispersion should be used. However, on the other hand, the purpose of our set-up was to demonstrate the principle of nulling interferometry without achromatic phase shifter. In that respect, we should compensate for a differential dispersion.

Obviously, additional dispersion only works in a set-up without achromatic phase shifter, since in this case, additional dispersion would limit the rejection ratio.

4.3 Conclusions

We have studied the effect of dispersion on the performances of N-beam nulling interferometers ($N \leq 6$). In the case of two beams, we have seen that, if there is no achromatic phase shifter, the rejection ratio will be minimal when there is no dispersion and the interference pattern will be symmetric with respect to the maximal intensity. Asymmetry will arise when introducing a glass plate in one of the beams. We have also concluded that if

we carefully choose the thickness of the glass plate, we can realize a first-order achromatic phase shift that will lead to an optimal rejection ratio. Increasing further the thickness will decrease the rejection ratio to reach a secondary minimum etc. In the two-beam case or in the three-beam case with (1-1-1) amplitude distribution, the optimal rejection ratio is of the order of 10^3 for the considered spectral band, compared to 10^2 without dispersion. For the case of three beams with an (1-2-1) amplitude distribution, the theoretical maximal rejection ratio could be larger than 5.10^5 in the same spectral band. Further, we have seen that in the visible domain (from 0.4 μm to 1 μm), a rejection ratio of 10^5 is possible with a spectral bandwidth $B = 2.4$ or even wider using four telescopes and BK7 plates. A rejection ratio of 10^6 in this spectral band can only be reached with a five-beam interferometer. In the mid-IR, we could reach, using CdTe plates, a rejection ratio of 10^7 in the whole $6 - 18$ μm spectral band with four beams and a rejection ratio of 10^5 with three beams.

If a perfectly achromatic phase shifter was used to achieve destructive interference, the rejection ratio would be infinite when there is no dispersion. The introduction of additional dispersion would decrease the rejection ratio and drastically limit the performances of the interferometer.

We have seen that dispersion should be compensated for when the goal of the set-up is to demonstrate nulling interferometry without achromatic phase shifter. On the other hand, following the analysis presented in this chapter, if we optimize the set-up for the highest reachable rejection ratio, additional dispersion can be used as an extra tool. Obviously, in the case of a set-up *with* an achromatic phase shifter, dispersion has to be compensated for since, in this case, it is a strict condition to achieve the best nulling performance.

Chapter 5

Multi-axial nulling interferometry

As mentioned in the introduction, there are conventionally two types of beam combination: uni-axial [20] and multi-axial [29, 30] combination (see Figure 5.1). The multi-axial combiner has the advantage to be achromatic and to be easily generalizable to any number of beams. Unfortunately, depending on the configuration, a longitudinal component of the electric field, also referred to as longitudinal polarization, will be introduced by the focusing optics and will limit the performances of the nulling interferometer.

In this chapter, we show the theoretical limitations of a multi-axial nulling interferometer with respect to longitudinal polarization. In Section 5.1, we use a simple approach to illustrate and quantify the longitudinal polarization issue. In Section 5.2, we use rigorous diffraction theory to validate the results obtained in Section 5.1. In Section 5.3, we analyze the filtering capabilities of a single-mode fiber with respect to that issue. In Section 5.4, we study the case of polarization-based nulling interferometers. Our conclusions are then summarized in Section 5.5.

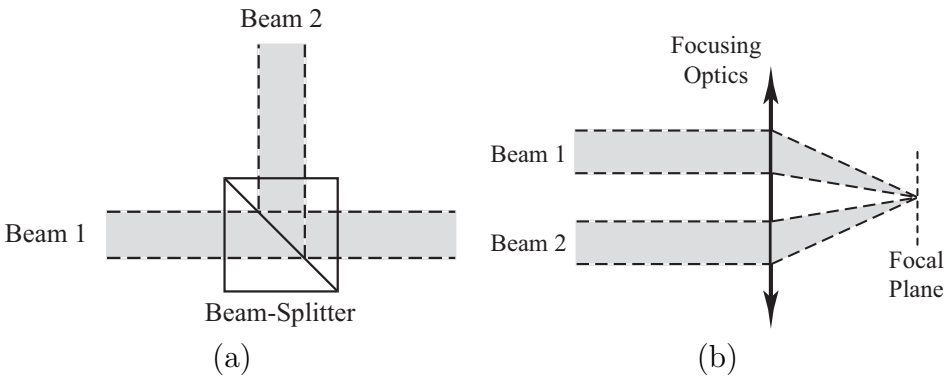

Figure 5.1: (a) Uni-axial and (b) multi-axial combination.

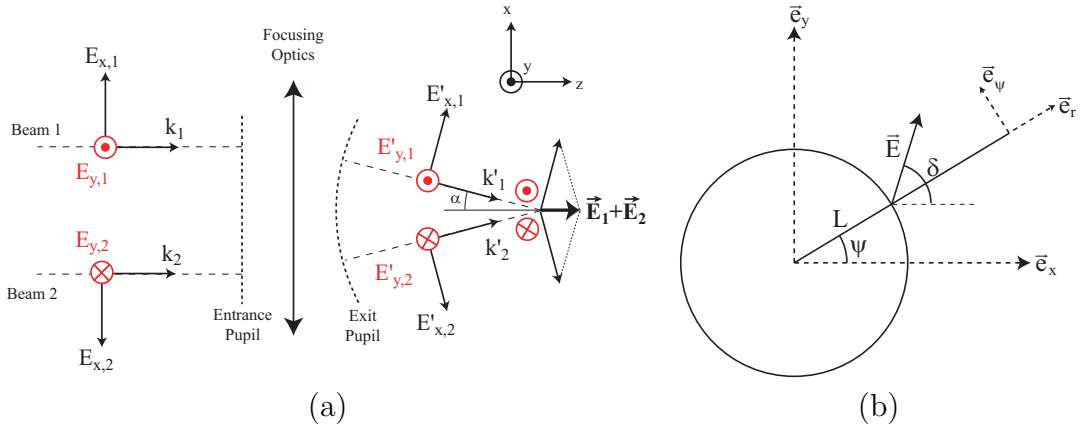

Figure 5.2: (a) Schematic combination of two out-of-phase linearly polarized beams. Depending on the initial orientation of the polarization, the focusing optics introduces a longitudinal component of the electric field. (b) Entrance pupil of the focusing optics with a beam whose position is (L, ψ) in polar coordinates and whose linear polarization is oriented at an angle δ.

5.1 Ray tracing

In this section, we use a simple ray tracing approach to illustrate and quantify the longitudinal polarization problem in a multi-axial beam combiner.

Consider two linearly polarized beams out of phase with equal amplitudes. We furthermore assume the beams to be monochromatic since the problem treated here does not depend on the width of the spectral band. Using a simple ray tracing model [63], we can show that the focusing optics rotates the wave vectors (k_1 and k_2) and therefore the vibration planes of the two beams (see Figure 5.2(a)). Depending on the initial polarization, a longitudinal field is created at focus. Indeed if the beams are linearly polarized along the baseline (x-polarized) and are out-of-phase, we can see on Figure 5.2(a) that the resulting vector at focus is non-zero and purely longitudinal (z-direction). This non-zero longitudinal field will be detected and will limit the rejection ratio and therefore the performance of the nulling interferometer. If the initial polarization is perpendicular to the baseline (y-polarized), the electric field remains transversal and the resulting on-axis energy density is zero. In this case, the rejection ratio is theoretically infinite.

Consider now an infinitely small beam of which the position in the entrance pupil is given in polar coordinates by (L, ψ) (see Figure 5.2(b)). If this beam is linearly polarized at an angle δ, the corresponding electric field in the entrance pupil $\vec{E}_{ent}$ can be written

$$\vec{E}_{ent} = E_0 \cos(\delta - \psi)\, \vec{e}_r + E_0 \sin(\delta - \psi)\, \vec{e}_\psi, \tag{5.1}$$

where $\vec{e}_r$ and $\vec{e}_\psi$ represent the polar and azimuthal axes. The electric field in the exit pupil $\vec{E}_{ex}$ is found by rotating the field $\vec{E}_{ent}$ around the azimuthal axis,

$$\begin{aligned} \vec{E}_{ex} \;=\; & E_0 \cos(\delta - \psi) \cos\alpha . \vec{e}_r + E_0 \sin(\delta - \psi)\, . \vec{e}_\psi \\ & + E_0 \cos(\delta - \psi) \sin\alpha . \vec{e}_z, \end{aligned} \tag{5.2}$$

which after simple trigonometric manipulations can be re-written in cartesian coordinates

$$\begin{aligned}\vec{E}_{ex} &= E_0\left\{\cos\delta + \left[\cos\delta\cos^2\psi + 1/2\sin\delta\sin\left(2\psi\right)\right]\left(\cos\alpha - 1\right)\right\}\vec{e}_x \\ &\quad + E_0\left\{\sin\delta + \left[1/2\cos\delta\sin\left(2\psi\right) + \sin\delta\sin^2\psi\right]\left(\cos\alpha - 1\right)\right\}\vec{e}_y \\ &\quad + E_0\left(\cos\delta\cos\psi + \sin\delta\sin\psi\right)\sin\alpha\,\vec{e}_z\,.\end{aligned} \tag{5.3}$$

The field at focus $\vec{E}$ is simply given by adding the fields in the exit pupil corresponding to all individual beams $\vec{E}_{ex,j}$,

$$\vec{E} = \sum_{j=1}^{N} \vec{E}_{ex,j}. \tag{5.4}$$

Consider N beams regularly spaced on a circle ($N > 1$). The position of the j^{th} beam in polar coordinates is given by $\left(L, \psi_j = \frac{2\pi}{N}\left(j-1\right)\right), j = 1, .., N$. The beams are all linearly-polarized at an angle δ and, in order to get on-axis destructive interference, the phase of the j^{th} beam is chosen to be $\phi_j = \frac{2\pi}{N}\left(j-1\right)$. In good approximation, the electric field at focus $\vec{E}$ is purely longitudinal and we have

$$\begin{aligned}E_z &= E_0\sin\alpha\cos\delta\underbrace{\sum_{j=1}^{N}\cos\left(\frac{2\pi}{N}\left(j-1\right)\right)\exp\left(i\frac{2\pi}{N}\left(j-1\right)\right)}_{\begin{cases}2 & \text{if } N=2\\ N/2 & \text{if } N\neq 2\end{cases}} \\ &\quad + E_0\sin\alpha\sin\delta\underbrace{\sum_{j=1}^{N}\sin\left(\frac{2\pi}{N}\left(j-1\right)\right)\exp\left(i\frac{2\pi}{N}\left(j-1\right)\right)}_{\begin{cases}0 & \text{if } N=2\\ Ni/2 & \text{if } N\neq 2\end{cases}} \\ &= \begin{cases}2E_0\sin\alpha\cos\delta, & \text{if } N=2,\\ E_0 N\sin\alpha\exp(i\delta)/2, & \text{if } N\neq 2.\end{cases}\end{aligned} \tag{5.5}$$

In order to calculate the rejection ratio, we also need the electric field in the case of a constructive interference. This purely transverse field can be calculated by setting the phase of each beam to zero. The field corresponding to constructive interference is given

by

$$\begin{aligned} E_x &= E_0 \sum_{j=1}^{N} \cos\delta \\ &\quad + E_0 \cos\delta \underbrace{\sum_{j=1}^{N} \cos^2 \frac{2\pi}{N}(j-1)}_{\begin{cases} 2, & \text{if } N=2, \\ N/2, & \text{if } N \neq 2, \end{cases}} (\cos\alpha - 1) \\ &\quad + E_0/2 \sin\delta \underbrace{\sum_{j=1}^{N} \sin\left(2\frac{2\pi}{N}(j-1)\right)}_{0} (\cos\alpha - 1) \\ &= \begin{cases} E_0 2\cos\delta\cos\alpha, & \text{if } N=2, \\ E_0 N\cos\delta\left(1+1/2\left(\cos\alpha-1\right)\right), & \text{if } N\neq 2, \end{cases} \\ &= \begin{cases} E_0 2\cos\delta\cos\alpha, & \text{if } N=2, \\ E_0 N\cos\delta\left(\cos\alpha+1\right)/2, & \text{if } N\neq 2, \end{cases} \end{aligned} \tag{5.6}$$

and

$$\begin{aligned} E_y &= E_0 \sum_{j=1}^{N} \sin\delta \\ &\quad + E_0/2 \cos\delta \underbrace{\sum_{j=1}^{N} \sin\left(2\frac{2\pi}{N}(j-1)\right)}_{0} (\cos\alpha - 1) \\ &\quad + E_0 \sin\delta \underbrace{\sum_{j=1}^{N} \sin^2 \frac{2\pi}{N}(j-1)}_{\begin{cases} 0, & \text{if } N=2, \\ N/2, & \text{if } N \neq 2, \end{cases}} (\cos\alpha - 1) \\ &= \begin{cases} E_0 2\sin\delta, & \text{if } N=2, \\ E_0 N\sin\delta\left(1+1/2\left(\cos\alpha-1\right)\right), & \text{if } N\neq 2, \\ E_0 2\sin\delta, & \text{if } N=2, \\ E_0 N\sin\delta\left(\cos\alpha+1\right)/2, & \text{if } N\neq 2. \end{cases} \end{aligned} \tag{5.7}$$

The electric energy density $\mathcal{U}_+$ corresponding to constructive interference is then given, within a constant factor, by

$$\mathcal{U}_+ = \begin{cases} 4\left|E_0\right|^2\left(\cos^2\delta\cos^2\alpha + \sin^2\delta\right), & \text{if } N=2, \\ \left|E_0\right|^2 N^2\left(\cos\alpha+1\right)^2/4, & \text{if } N\neq 2, \end{cases} \tag{5.8}$$

which shows as expected that the power corresponding to constructive interference is proportional to N^2.

The rejection ratio is found by dividing the electric energy densities corresponding to constructive and destructive interferences,

$$R = \begin{cases} \frac{\left(\cos^2\delta\cos^2\alpha+\sin^2\delta\right)}{\sin^2\alpha\cos^2\delta}, & \text{if } N = 2, \\ \frac{(\cos\alpha+1)^2}{\sin^2\alpha}, & \text{if } N \neq 2. \end{cases} \tag{5.9}$$

For very small numerical apertures ($\alpha < 0.1$), we have

$$R \approx \begin{cases} \frac{1}{\sin^2\alpha\cos^2\delta}, & \text{if } N = 2, \\ \frac{4}{\sin^2\alpha}, & \text{if } N \neq 2. \end{cases} \tag{5.10}$$

From Eq. (5.10), we can see that the rejection ratio is inversely proportional to the square of the numerical aperture[1] ($\sin\alpha$). We can also see that when $N > 2$, the rejection ratio does not depend on the orientation of the incoming linear polarization. In the two-beam case, as we discussed previously, the rejection ratio is infinite if the polarization is perpendicular to the baseline ($\delta = \pi/2$) and minimum if the polarization is along the baseline ($\delta = 0$). Note that for small numerical apertures, the electric energy density $\mathcal{U}_+$ corresponding to constructive interference is simply given by

$$\mathcal{U}_+ = |E_0|^2 N^2, \tag{5.11}$$

which is the expected value for the constructive interference of a N-beam interferometer.

5.2 Electric field distribution

In Section 5.1, we showed, based on geometrical considerations, that longitudinal polarization will limit the rejection ratio of a multi-axial nulling interferometer. In order to validate these results in the case of extended beams, we will, in this section, perform an analysis of the three-dimensional electric field distribution in the focal plane of the focusing optics using rigorous diffraction theory.

5.2.1 Theory

Let us consider the aplanatic imaging system depicted in Figure 5.3. In this imaging system, the electric field in the entrance pupil $\mathbf{E}_0(k_r, k_\phi, 0)$ is mapped to the exit pupil $\mathbf{E}_1(k_r, k_\phi, k_z)$ according to the aplanatic condition. This exit pupil is a spherical shell with radius ρ. To describe the electric field, we introduce two sets of cylindrical coordinates: $\mathbf{k} = (k_r, k_\phi, k_z)$ in the exit pupil and $\mathbf{r} = (r, \phi, z)$ in the focal region, where the plane $z = 0$ is the focal plane. If we consider a monochromatic time-harmonic electric field, we can calculate the electric field distribution in the focal plane using diffraction integrals

[1] In astronomy, it is more common to describe a telescope in terms of f-number instead of numerical aperture (f-number$= 1/2\sin\alpha$).

described by Ignatowsky [64] and re-derived by Richards and Wolf [65]. These diffraction integrals are valid in the Debye approximation and therefore our point of observation should not be too close to the spherical shell Ω over which the integration takes place. Nevertheless, it is more convenient to integrate over the entrance pupil Ω' rather than over the exit pupil Ω. In a weakly-aberrated and aplanatic imaging system with the object at infinity, the transition from the entrance pupil to the exit pupil can be considered as a rotation of the wave vector, described by the propagation matrix $\mathbf{M}$ [66]

$$\mathbf{M} = \frac{1}{k}\begin{pmatrix} k_z\cos^2 k_\phi + k\sin^2 k_\phi & (k_z - k)\cos k_\phi \sin k_\phi \\ (k_z - k)\cos k_\phi \sin k_\phi & k_z \sin^2 k_\phi + k\cos^2 k_\phi \\ -k_r \cos k_\phi & -k_r \sin k_\phi \end{pmatrix}, \tag{5.12}$$

where $k = 2\pi/\lambda$ is the wave number. This matrix is a (3×2)-matrix since, with the foregoing assumptions, the electric field has no z-component in the entrance pupil.

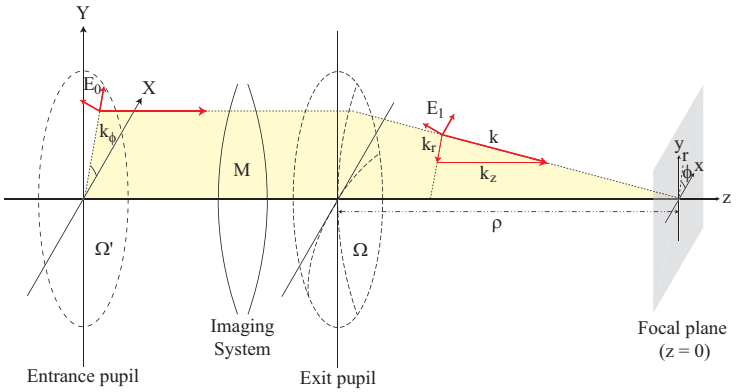

Figure 5.3: Schematic overview of the studied configuration. Light distribution in the entrance pupil $\mathbf{E}_0(k_r, k_\phi, 0)$ is mapped to the exit pupil $\mathbf{E}_1(k_r, k_\phi, k_z)$ via an aplanatic imaging system, denoted by the operation $\mathbf{M}$. The field distribution in the focal region is then obtained by integration over the exit pupil. The focal plane is the plane $z = 0$.

Taking these considerations into account, the electric field in the focal plane is given by [66]

$$\mathbf{E}(r, \phi, 0) = -\frac{i\rho}{2\pi}\iint_{\Omega'}\sqrt{\frac{k_z}{k}}\frac{\mathbf{M}.\mathbf{E}_0(k_r, k_\phi)}{k_z}\exp\left[irk_r\cos(k_\phi - \phi)\right]k_r dk_r dk_\phi. \tag{5.13}$$

This expression allows us to calculate the three-dimensional distribution of the electric field in the focal plane $\mathbf{E}(r, \phi, 0)$ given a certain field $\mathbf{E}_0(k_r, k_\phi)$ in the entrance pupil. The electric energy density in the focal plane is then given by

$$\mathcal{U}(r, \phi) = \frac{\epsilon_0}{2}\left[|E_x(r, \phi)|^2 + |E_y(r, \phi)|^2 + |E_z(r, \phi)|^2\right]. \tag{5.14}$$

To calculate the rejection ratio R, we need the on-axis densities corresponding to constructive ($\mathcal{U}_+$) and destructive ($\mathcal{U}_-$) interferences.

$$R = \frac{\mathcal{U}_+(r = 0)}{\mathcal{U}_-(r = 0)}. \tag{5.15}$$

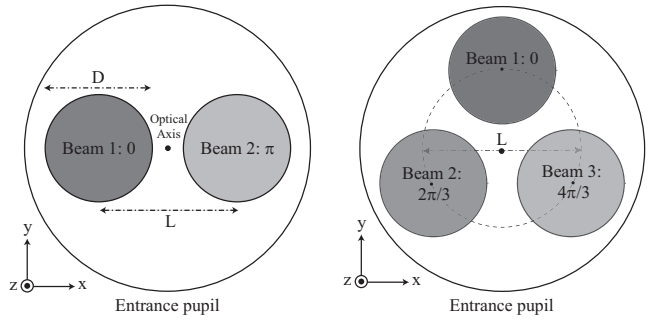

Figure 5.4: Schematic entrance pupil for the combination of (a) two beams positioned along the x-axis and (b) three beams. There is a phase-shift between the beams in order to have on-axis destructive interference. The applied phases are (a) 0 and π and (b) 0, $2\pi/3$ and $4\pi/3$. The diameter of the beams is D and the baseline is L.

Note that Eq. (5.15) only gives a theoretical rejection ratio since in practice, one would need an infinitely small, mono-pixel detector. In reality, the detector has a certain extent and will therefore capture more light. Therefore, the rejection ratio as defined in Eq. (5.15) gives a maximal theoretical limit. Note also that the case of a pinhole-detector is not taken into account here, since a realistic pinhole size will automatically lead to a very poor performance of the multi-axial nulling interferometer.

5.2.2 Simulations

Nulling interferometry can be performed with any number N of beams. However, in practice, a small number of beams ($N \leq 3$) is generally proposed. Therefore, in this section, we will only consider two- and three-beam nulling interferometers.

We use in all simulations linearly polarized beams with equal and constant amplitudes (top-hat distribution) and the phase of the j^{th} beam is chosen to be $\phi_j = \frac{2\pi}{N}(j-1)$ in order to get on-axis destructive interference. The diameter of the beams is $D = 2$ cm and the wavelength is 600 nm. The focusing optics that we simulated has a focal length $f = 60$ cm and the distance between the beams in the entrance pupil, called the *baseline*, is $L = 5$ cm. Note that for a number of beams $N > 2$, we can define the baseline as the diameter of the circle on which the centers of the beams are positioned. For $N = 2$, these two definitions coincide. The values of the different parameters have been chosen to match our table-top experimental set-up.

Two-beam interference

In this case, we consider multi-axial combination of two beams (see Figure 5.4(a)). The baseline is along the x-axis and we consider linearly polarized beams along the x- and y-axis.

The amplitudes of the three-dimensional electric field components in the focal plane for x- and y-polarized beams are respectively depicted in Figure 5.5(a) and Figure 5.5(b). In each case, the three components of the field have been normalized to the largest component (E_x for x-polarization and E_y for y-polarization). In both cases, the main field component shows the well-known interference fringes and the other transverse component is negligible. Only the modulus of the field components is depicted in Figure 5.5(a) and Figure 5.5(b). If the phase was also represented, we would see that the longitudinal components are centro-symmetric while the transverse components are anti-symmetric and therefore equal to zero on-axis ($x = 0$ and $y = 0$) whatever the polarization. When the polarization is perpendicular to the baseline (see Figure 5.5(b)), the on-axis longitudinal field is also equal to zero in such a way that the on-axis energy density is null. The rejection ratio is therefore infinite. As expected from the ray-tracing model, when the polarization is along the baseline (see Figure 5.5(a)), the on-axis longitudinal component is no longer equal to zero, implying a limited rejection ratio (to 575 in this case).

Three-beam interference

In this case, we consider the combination of three beams regularly spaced on a circle of diameter $L = 5$ cm as depicted in Figure 5.4(b). In order to have on-axis destructive interference, the phases of the different beams have been respectively chosen to be equal to 0, $2\pi/3$ and $4\pi/3$.

The field distributions for $x-$ and $y-$polarizations are depicted in Figure 5.5(c) and Figure 5.5(d). In the three-beam case, none of the components are either symmetric or anti-symmetric and the on-axis longitudinal field is always non-zero. The rejection ratio of such a three-beam multi-axial nulling interferometer is therefore limited for both x- and y- polarizations (to 2300 in this case).

N-beam interference

As shown by Eq. (5.10), the rejection ratio in the case of a N-beam multi-axial interferometer is limited for both polarizations to the same value for all $N > 2$.

Influence of the numerical aperture

We can define an effective numerical aperture ($\mathrm{NA_{eff}}$) as the ratio between the semi-baseline $L/2$ and the focal length of the focusing optics f,

$$\mathrm{NA_{eff}} = \frac{L}{2f}. \tag{5.16}$$

The rejection ratio as a function of the effective numerical aperture in the case of two and three beams is depicted in Figure 5.6. The dots represent the rejection ratio calculated with rigorous diffraction theory, while the lines have been calculated using Eq. (5.10). We

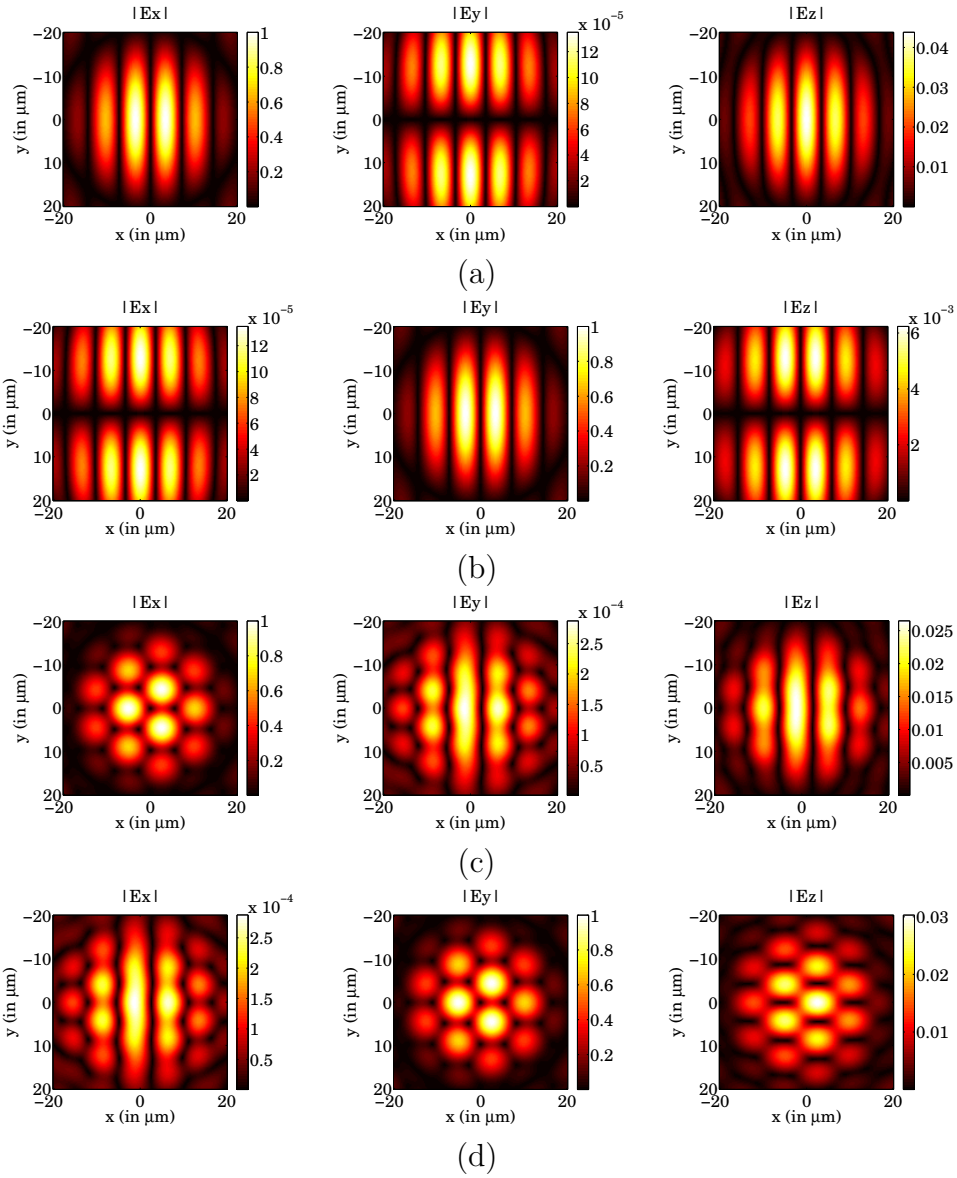

Figure 5.5: Three components of the electric field ($|E_x|$, $|E_y|$ and $|E_z|$) in the focal plane of the focusing optics in the case of ((a) and (b)) two-beam and ((c) and (d)) three-beam multi-axial combiner. The beams are linearly polarized along either the x-axis ((a) and (c)) or the y-axis ((b) and (d)). In each case, the three components of the field have been normalized to the largest component (E_x for x-polarization and E_y for y-polarization).

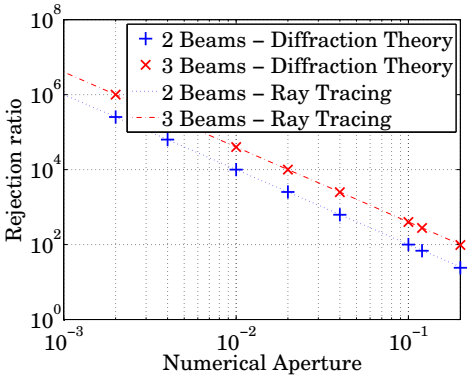

Figure 5.6: Rejection ratio as a function of the effective numerical aperture.

can see that for both two- and three-beam cases, the agreement between ray tracing and diffraction theory is very good.

In a real nulling interferometer, the numerical aperture of the focusing optics is typically 0.06 in order to match the numerical aperture of the single-mode fiber (used for wavefront filtering). The corresponding rejection ratio is of the order of 10^2 for two beams and 10^3 for three beams. This is definitely too low for Earth-like exoplanet detection and such a multi-axial nulling interferometer therefore cannot be used as such. A solution needs to be found to solve this fundamental problem.

5.3 Longitudinal polarization and single-mode fibers

In Section 5.2, we studied the electric field distribution in the focal plane of the focusing optics and we concluded that the rejection ratio of a multi-axial nulling interferometer can be drastically limited due to longitudinal polarization. However, a wavefront filter is needed to have quasi-perfect destructive interference. This filter will affect the field distribution and therefore the rejection ratio. In the case of multi-axial nulling interferometry, an efficient way to perform wavefront filtering is to focus the light from the different beams into a unique single-mode fiber (positioned at the focus of the imaging system) [33]. In this section, we will study the filtering capabilities of a single-mode fiber with respect to the longitudinal polarization issue. We will consider perfectly lossless and perfectly single-mode fibers. In reality, these fibers are not ideal and the lack of single-modeness might limit the performance of the interferometer. However, these issues are out of the scope of this chapter.

5.3.1 Theory

If we neglect losses inside the fiber, the output field of an optical fiber can be described in terms of complex coupling efficiencies [31, 67, 32]. Consider an incoming field focused onto an optical fiber. The incoming electric field $\vec{E}_{inc}(x, y)$ will excite a certain mode $\vec{E}_j(x, y)$

of the fiber with a certain (complex) strength, namely the complex coupling efficiency ξ_j. As shown in [68], all modes (bound and radiation modes) of a non-absorbing waveguide satisfy the orthogonality relation

$$\iint \left(\vec{E}_j(x,y) \times \vec{H}_k^*(x,y)\right) \cdot \vec{z}\, dxdy = \delta_{jk} \iint \left(\vec{E}_j(x,y) \times \vec{H}_j^*(x,y)\right) \cdot \vec{z}\, dxdy, \quad (5.17)$$

where $\vec{H}_k^*(x,y)$ is the complex conjugate of the magnetic field $\vec{H}_k$ of the k^th mode, $\vec{z}$ is the unit vector along the axis of the fiber and δ_{jk} is the Kronecker symbol. Using this relation, we can find an expression for the complex coupling efficiency ξ_j to the j^{th} mode

$$\xi_j = \frac{\iint \left(\vec{E}_{inc}(x,y) \times \vec{H}_j^*(x,y)\right) \cdot \vec{z}\, dxdy}{\iint \left(\vec{E}_j(x,y) \times \vec{H}_j^*(x,y)\right) \cdot \vec{z}\, dxdy}. \quad (5.18)$$

From Eq. (5.18), we can see that the distribution of the longitudinal field does not play any role in the calculation of the coupling efficiencies since only the z-component of the cross product between the incident field and the corresponding modes is used. The electric field $\vec{E}(x,y)$ propagating inside the fiber is then given by

$$\vec{E}(x,y) = \sum_j \xi_j \vec{E}_j(x,y). \quad (5.19)$$

A single-mode fiber has two orthogonal fundamental modes corresponding to the two orthogonal polarizations. In order to keep the same nomenclature as in [68], we will call these modes even $\vec{E}_e$ and odd $\vec{E}_o$. An expression for these modes is given in Appendix B. The electric field at the output of the fiber is then given by

$$\vec{E}(x,y) = \xi_e \vec{E}_e(x,y) + \xi_o \vec{E}_o(x,y), \quad (5.20)$$

where ξ_e and ξ_o are given by Eq. (5.18). For the magnetic field, we have

$$\vec{H}(x,y) = \xi_e \vec{H}_e(x,y) + \xi_o \vec{H}_o(x,y), \quad (5.21)$$

where $\vec{H}_e$ and $\vec{H}_o$ denote respectively the magnetic fields of the even and the odd fundamental modes of the fiber. The average energy flow is then given by the Poynting vector $\vec{S}$ defined as

$$\vec{S}(x,y) = \frac{1}{2}\Re\left(\vec{E}(x,y) \times \vec{H}^*(x,y)\right). \quad (5.22)$$

The output power is found by integrating the z-component of the Poynting vector $S_z(x,y)$ over the xy-plane,

$$P_{out} = \iint S_z(x,y)\, dxdy. \quad (5.23)$$

Since both even and odd modes are orthogonal in the sense of Eq. (5.17) and since the powers corresponding to these modes are equal ($P_e = P_o = P$), we find for the output power

$$P_{out} = \left(|\xi_e|^2 + |\xi_o|^2\right) P. \quad (5.24)$$

Knowing the electric field distributions in the focal plane of the focusing optics for both constructive and destructive interferences, we can calculate the different coupling efficiencies and therefore the output powers corresponding to constructive ($P_{out,+}$) and destructive ($P_{out,-}$) interferences. The rejection ratio after fiber filtering is then given by

$$R_{out} = \frac{P_{out,+}}{P_{out,-}} = \frac{|\xi_{e,+}|^2 + |\xi_{o,+}|^2}{|\xi_{e,-}|^2 + |\xi_{o,-}|^2}. \tag{5.25}$$

Note that this expression is only valid in the monochromatic case.

Consider N ray-like beams regularly spaced on a circle. The position of the j^{th} beam in polar coordinates is given by $\left(k_r, k_{\phi,j} = \frac{2\pi}{N}(j-1)\right), j = 1, .., N$. The beams are linearly-polarized at an angle δ and, in order to get on-axis destructive interference, the phase of the j^{th} beam is chosen to be $\phi_j = \frac{2\pi}{N}(j-1)$. Under these conditions, we can use Eq. (5.13) to find an analytical expression for the transverse electric field distribution in the focal plane. After elementary manipulations, we find

$$E_x = K \sum_{j=1}^{N} \{[G_1 \cos\delta - G_2 \cos(\delta - 2k_{\phi,j})] \exp(i\phi_j) \exp[irk_r \cos(k_{\phi,j} - \phi)]\}, \tag{5.26a}$$

$$E_y = K \sum_{j=1}^{N} \{[G_1 \sin\delta + G_2 \sin(\delta - 2k_{\phi,j})] \exp(i\phi_j) \exp[irk_r \cos(k_{\phi,j} - \phi)]\}. \tag{5.26b}$$

where

$$\begin{aligned} K &= -\tfrac{i\rho}{2\pi} \tfrac{\exp(ik_z)}{\sqrt{k_z k}} k_r, \\ G_1 &= 1/2\,(1 + k_z/k)\,, \\ G_2 &= 1/2\,(1 - k_z/k)\,. \end{aligned} \tag{5.27}$$

To calculate the coupling efficiencies given by Eq. (5.18), we need to know the magnetic fields of the fundamental modes. An expression for these fields in the case of a step-index single-mode fiber is given in Appendix B. The transverse magnetic fields for both even and odd modes can be rewritten

$$H_{x,e}(r,\phi) = A_2(r)\sin(2\phi)\,, \tag{5.28a}$$

$$H_{y,e}(r,\phi) = -A_1(r) - A_2(r)\cos(2\phi)\,, \tag{5.28b}$$

$$H_{x,o}(r,\phi) = A_1(r) - A_2(r)\cos(2\phi)\,, \tag{5.28c}$$

$$H_{y,o}(r,\phi) = -A_2(r)\sin(2\phi)\,. \tag{5.28d}$$

where

$$\begin{aligned} A_1(r) &= \left(\tfrac{\epsilon_0}{\mu_0}\right)^{1/2} \tfrac{kn_{co}^2}{\beta} \begin{cases} a_3 \frac{J_0(Ur/a)}{J_1(U)}, & \text{if } r \le a \\ \frac{U}{W} a_5 \frac{K_0(Wa)}{K_1(W)}, & \text{if } r > a \end{cases}, \\ A_2(r) &= \left(\tfrac{\epsilon_0}{\mu_0}\right)^{1/2} \tfrac{kn_{co}^2}{\beta} \begin{cases} a_4 \frac{J_2(Ur/a)}{J_1(U)}, & \text{if } r \le a \\ -\frac{U}{W} a_6 \frac{K_2(Wr/a)}{K_1(W)}, & \text{if } r > a \end{cases}. \end{aligned} \tag{5.29}$$

These components of the magnetic field are depicted in Figure 5.7, where the contribution from the components with 2ϕ-dependence is orders of magnitude smaller than the rotationally symmetric components. We can see on Figure 5.7 and in Eq. (5.28) that all even and odd transverse magnetic fields are centro-symmetric functions ($H_{e,t}(r,\phi) = H_{e,t}(r,\pi+\phi)$ and $H_{o,t}(r,\phi) = H_{o,t}(r,\pi+\phi)$). Therefore, if the incoming electric field has anti-symmetric transverse components, both coupling efficiencies in Eq. (5.18) will be equal to zero: such a field will not be coupled into the fiber.

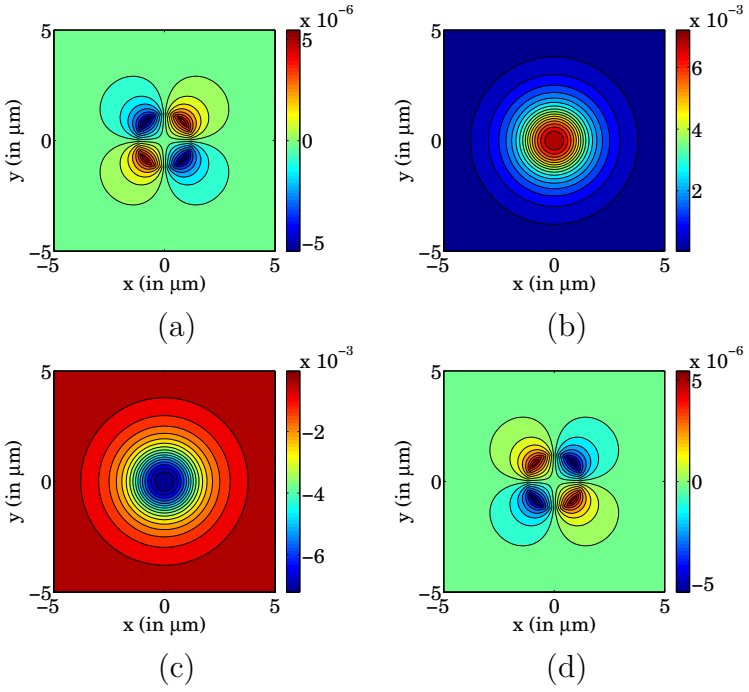

Figure 5.7: Transverse magnetic fields of the fundamental modes of a step-index single-mode fiber: (a) and (b) even mode (respectively $H_{e,x}(x,y)$ and $H_{e,y}(x,y)$) and (c) and (d) odd mode (respectively $H_{o,x}(x,y)$ and $H_{o,y}(x,y)$).

The coupling efficiency $\xi_{o,-}$ to the odd mode is given by

$$\xi_{o,-} = \int_0^{\infty}\int_0^{2\pi} \left[E_x(r,\phi)\, H_{y,o}(r,\phi) - E_y(r,\phi)\, H_{x,o}(r,\phi)\right] r\, dr\, d\phi. \tag{5.30}$$

After replacing Eq. (5.26) and Eq. (5.28) into Eq. (5.30) and after putting similar terms

together, we find

$$\begin{aligned}
\xi_{o,-} &= -K\int_0^{\infty}\int_0^{2\pi}\sum_{j=1}^{N} G_1 \sin\delta \exp\left(i\phi_j\right)\exp\left[irk_r\cos\left(k_{\phi,j}-\phi\right)\right]A_1\left(r\right)r\,dr\,d\phi \\
&\quad -K\int_0^{\infty}\int_0^{2\pi}\sum_{j=1}^{N} G_2 \sin\left(\delta-2k_{\phi,j}\right)\exp\left(i\phi_j\right)\exp\left[irk_r\cos\left(k_{\phi,j}-\phi\right)\right]A_1\left(r\right)r\,dr\,d\phi \\
&\quad +K\int_0^{\infty}\int_0^{2\pi}\sum_{j=1}^{N} G_1 \sin\left(\delta-2\phi\right)\exp\left(i\phi_j\right)\exp\left[irk_r\cos\left(k_{\phi,j}-\phi\right)\right]A_2\left(r\right)r\,dr\,d\phi \\
&\quad +K\int_0^{\infty}\int_0^{2\pi}\sum_{j=1}^{N} G_2 \sin\left(\delta-2k_{\phi,j}+2\phi\right)\exp\left(i\phi_j\right)\exp\left[irk_r\cos\left(k_{\phi,j}-\phi\right)\right]A_2\left(r\right)r\,dr\,d\phi.
\end{aligned} \tag{5.31}$$

Using the integral definitions of the Bessel functions presented in Appendix A, we find

$$\begin{aligned}
\xi_{o,-} &= -2\pi K G_1 \sin\delta\sum_{j=1}^{N}\exp\left(i\phi_j\right)\int_0^{\infty} J_0\left(rk_r\right)A_1\left(r\right)\,r\,dr \\
&\quad -2\pi K G_2\sum_{j=1}^{N}\sin\left(\delta-2k_{\phi,j}\right)\exp\left(i\phi_j\right)\int_0^{\infty} J_0\left(rk_r\right)A_1\left(r\right)\,r\,dr \\
&\quad -2\pi K G_1\sum_{j=1}^{N}\sin\left(\delta-2k_{\phi,j}\right)\exp\left(i\phi_j\right)\int_0^{\infty} J_2\left(rk_r\right)A_2\left(r\right)\,r\,dr \\
&\quad -2\pi K G_2\sum_{j=1}^{N}\sin\left(\delta-2k_{\phi,j}+2k_{\phi,j}\right)\exp\left(i\phi_j\right)\int_0^{\infty} J_2\left(rk_r\right)A_2\left(r\right)\,r\,dr.
\end{aligned} \tag{5.32}$$

where J_0 and J_2 denote respectively the zeroth and the second order Bessel functions of the first kind. Finally, after using the sum identities given in Appendix A, we have

$$\xi_{o,-} = \begin{cases} -3i\pi K\exp\left(-i\delta\right)\left(G_1 I_2 + G_2 I_1\right), & \text{if } N=3 \\ 0, & \text{if } N\neq 3 \end{cases}, \tag{5.33}$$

where $I_1 = \int_0^{\infty} J_0\left(rk_r\right)A_1\left(r\right)\,r\,dr$ and $I_2 = \int_0^{\infty} J_2\left(rk_r\right)A_2\left(r\right)\,r\,dr$.

Similarly, for the coupling efficiency corresponding to the even mode $\xi_{e,-}$, we have

$$\xi_{e,-} = \begin{cases} 3\pi K\exp\left(-i\delta\right)\left(G_1 I_2 + G_2 I_1\right), & \text{if } N=3 \\ 0, & \text{if } N\neq 3 \end{cases}. \tag{5.34}$$

In order to calculate the rejection ratio, we need to know the coupling efficiencies corresponding to the constructive interference. In this case, the beams are all in phase ($\phi_j = 0$).

After calculations, we find (for $N \neq 2$)

$$\begin{aligned} \xi_{o,+} &= -2\pi KN \sin(\delta) (G_1 I_1 + G_2 I_2), \\ \xi_{e,+} &= -2\pi KN \cos(\delta) (G_1 I_1 + G_2 I_2). \end{aligned} \tag{5.35}$$

In the case of constructive interference, the detected power would be given by

$$P_{out} = 4\pi^2 K^2 N^2 |G_1 I_1 + G_2 I_2|^2 P, \tag{5.36}$$

which shows that the photon flux coming from the planet is proportional to N^2.

The rejection ratio is then found using Eq. (5.25)

$$R_{out} = \begin{cases} 2\left|\frac{G_1 I_1 + G_2 I_2}{G_1 I_2 + G_2 I_1}\right|^2, & \text{if } N = 3 \\ \infty, & \text{if } N \neq 3 \end{cases}. \tag{5.37}$$

For very small numerical apertures ($\mathrm{NA_{eff}} < 0.01$), we have

$$G_2/G_1 \propto \mathrm{NA_{eff}^2} \text{ and } I_2/I_1 \propto \mathrm{NA_{eff}^2}, \tag{5.38}$$

in such a way that $G_2 I_2 / G_1 I_1 \propto \mathrm{NA_{eff}^4}$. The rejection ratio is therefore given in good approximation by

$$R_{out} = \begin{cases} 2\left|\frac{1}{G_2/G_1 + I_2/I_1}\right|^2 \propto \mathrm{NA_{eff}^{-4}}, & \text{if } N = 3 \\ \infty, & \text{if } N \neq 3 \end{cases}. \tag{5.39}$$

Except for the case $N = 3$, both coupling efficiencies $\xi_{o,-}$ and $\xi_{e,-}$ are equal to zero in such a way that no light will be coupled in the fiber. The rejection ratio will therefore be theoretically infinite for $N \neq 3$. When $N = 3$, the rejection ratio is in good approximation inversely proportional to the fourth power of the numerical aperture while it was inversely proportional to the square of the numerical aperture without optical fiber. We can also see in Eq. (5.39) that the rejection ratio does not depend on the initial direction of the polarization. Note that the rejection ratio given in Eq. (5.37) is only rigorous for ray-like beams and not for finite-size beams.

5.3.2 Simulations

In this section, we have performed numerical simulations in order to validate the results obtained in Section 5.1 and in order to extend these results to finite-size beams. In all simulations, propagation losses inside the fiber are neglected. Only the coupling losses (due to a mismatch between the incoming field and the mode of the fiber) are taken into account.

In our simulations, we use a wavelength of 600 nm and a step-index single-mode fiber with a numerical aperture NA = 0.125 and a core radius $a = 1.2$ μm. We assume a

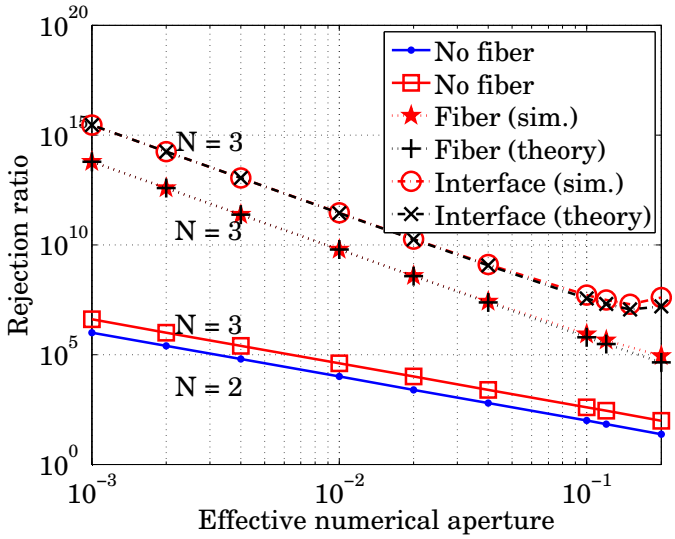

Figure 5.8: Rejection ratio as a function of the effective numerical aperture in the case of two beams (dots, solid line) and three beams (squares, solid line) without fiber filtering and in the case of three beams after the fiber (stars, dotted line). The circle-markers dash-dotted line corresponds to the three-beam case after fiber filtering when Fresnel losses are taken into account. The plus-markers dotted line and the cross-markers dash-dotted line are the theoretical curves obtained with Eq. (5.39).

core material with a refractive index $n_{co} = 1.45$. For such a fiber, the two orthogonal fundamental modes are given in Appendix B.

Using the results of Section 5.2 for the electric field distributions in the focal plane, we can calculate the different coupling efficiencies in Eq. (5.18) and the rejection ratio in Eq. (5.25).

For $N \neq 3$, we indeed find an infinite rejection ratio for all incoming polarizations and numerical apertures. The rejection ratio as a function of the effective numerical aperture in the case $N = 3$ is depicted in Figure 5.8 (stars, dotted line). The plus-markers dotted line is the theoretical curve calculated with Eq. (5.39). We can see that the agreement between these simulations and the theoretical rejection ratio is very good for NA < 0.01. For these low numerical apertures, the rejection ratio is inversely proportional to the fourth power of the numerical aperture, as predicted by Eq. (5.39). For larger numerical apertures, both curves start diverging from each other but remain of the same order of magnitude. For a typical numerical aperture of 0.06, the rejection ratio would be of the order of 10^6 and would therefore be large enough for Earth-like planet detection.

In all cases, our extended-beam simulations are in very good agreement with the theoretical results obtained in Section 5.1 with ray-like beams.

Fresnel losses

When coupled into an optical fiber, light goes through an air-glass interface. Some of the light does not go through the interface but is reflected back. The losses due to this reflection are called *Fresnel losses*. These losses can have an effect on the rejection ratio since the field distribution will be affected by the interface. In this section, we calculate the rejection ratio after fiber filtering taking into account the air-glass interface.

We consider an air-glass ($n = 1.45$) interface in the focal plane of the focusing optics. Using the formalism described in [66], we can calculate the field distribution at a certain distance (we chose one wavelength) after the interface. The coupling efficiencies (and therefore the rejection ratio) corresponding to these field distributions can then be calculated using Eq. (5.18).

The rejection ratio for three-beam interference as a function of the numerical aperture is depicted in Figure 5.8 (circles, dash-dotted line). We see a very good agreement with the theoretical rejection ratio calculated with Eq. (5.39) (crosses, dash-dotted line). We also see that the presence of the interface improves the rejection ratio (still inversely proportional to the fourth power of the effective numerical aperture for NA < 0.01). In the case of a numerical aperture of $\mathrm{NA}_{\mathrm{eff}} = 0.06$, the rejection ratio would be of the order of 10^8. Note that the rejection ratio for $N \neq 3$ is still infinite for all numerical apertures.

However, even though the interface improves the rejection ratio, it also leads to a reduction of the photon flux coming from the planet. The photon flux has been numerically estimated to be 66% of the flux obtained without interface. Therefore, a trade-off has to be made between high rejection ratio and photon flux. If a 10^6 rejection ratio is sufficiently high, then an anti-reflection coating should be applied to reduce Fresnel losses and therefore to gain photons.

5.4 Polarization-based nulling interferometers

In the previous sections, we have considered nulling interferometers in which destructive interference is achieved by phase shifting. In this section, we consider nulling interferometers based on rotation of the polarization instead of phase shifting [69]. In such a nulling interferometer, all beams are in phase ($\phi_j = 0$) but the direction of the polarization is rotated ($\delta_j = \delta_0 + \psi_j$) for each beam (see Figure 5.9 (a)). Such polarization rotations can be obtained, for instance, with achromatic half-wave plates.

5.4.1 Ray tracing

Similarly to what has been done in Section 5.1, the electric field in the entrance pupil corresponding to the linearly polarized j^{th} beam can be found by replacing $\delta_j = \delta_0 + \psi_j$

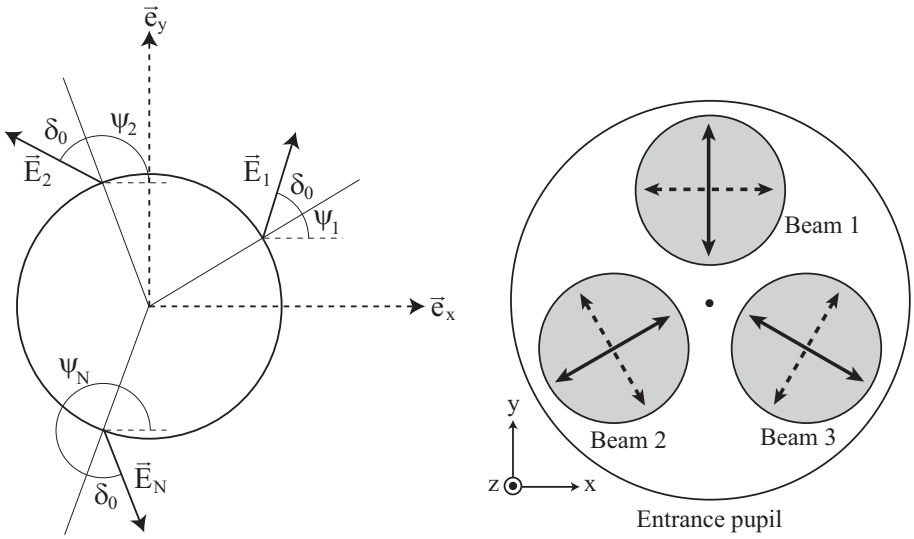

(a) (b)

Figure 5.9: Schematic entrance pupil of a multi-axial nulling interferometer based on polarization rotation (a) in the case of N ray-like beams and (b) in the case of three extended beams. The solid arrows represent a quasi-radial polarization while the dotted arrows represent the quasi-azimuthal polarization

into Eq. (5.1),

$$\vec{E}_{ent,j} = E_0 \cos\delta_0 \, \vec{e}_r + E_0 \sin\delta_0 \, \vec{e}_\psi. \tag{5.40}$$

A rotation around the azimuthal axis gives the electric field in the exit pupil,

$$\begin{aligned} \vec{E}_{ex,j} \;=\; & E_0 \left[\cos\delta_0 \cos\left(\tfrac{2\pi}{N}(j-1)\right)\cos\alpha - \sin\delta_0 \sin\left(\tfrac{2\pi}{N}(j-1)\right)\right]\vec{e}_x \\ & + E_0 \left[\cos\delta_0 \sin\left(\tfrac{2\pi}{N}(j-1)\right)\cos\alpha - \sin\delta_0 \cos\left(\tfrac{2\pi}{N}(j-1)\right)\right]\vec{e}_y \\ & + E_0 \cos\delta_0 \sin\alpha \, \vec{e}_z \,. \end{aligned} \tag{5.41}$$

The electric field at focus is purely longitudinal and simply given by the sum of all individual longitudinal fields,

$$E_z = E_0 N \cos\delta_0 \sin\alpha. \tag{5.42}$$

A calculation of the electric field corresponding to constructive interference is not straightforward since we first need to find for which phase differences between the beams we have a maximal intensity. This can be done by maximizing the on-axis transverse field or, equivalently, by minimizing the on-axis longitudinal field. If we assume that each beam has a different phase ϕ_j, the on-axis longitudinal field is simpy given by

$$E_z = E_0 \sum_{j=1}^{N} \exp\left(i\phi_j\right) \cos\delta_0 \sin\alpha. \tag{5.43}$$

This longitudinal field can be cancelled by choosing the following phases ϕ_j,

$$\phi_j = \frac{2\pi}{N}(j-1)\,. \tag{5.44}$$

Using these phases, we can calculate the transverse on-axis electric field and thereafter the on-axis electric energy density $\mathcal{U}_+$ corresponding to constructive interference. After calculations, we find

$$\mathcal{U}_+ = \left(\cos^2\delta_0\cos^2\alpha + \sin^2\delta_0\right)\begin{cases} 4\left|E_0\right|^2, & \text{if } N = 2, \\ \left|E_0\right|^2 N^2/2, & \text{if } N \neq 2. \end{cases} \tag{5.45}$$

Comparing Eq. (5.45) with Eq. (5.8), we see that both expressions are identical in the case $N = 2$, which is normal since a polarization rotation of π and a phase shift of π are mathematically equivalent. However, for $N > 2$, the maximal intensity of such a polarization-based interferometer is only half the intensity obtained with a phase-based interferometer. The latter is therefore twice as efficient.

The rejection ratio is given by

$$R = \begin{cases} \frac{4\left(\cos^2\delta_0\cos^2\alpha+\sin^2\delta_0\right)}{\sin^2\alpha\cos^2\delta}, & \text{if } N = 2, \\ \frac{N^2\left(\cos^2\delta_0\cos^2\alpha+\sin^2\delta_0\right)}{2\sin^2\alpha\cos^2\delta}, & \text{if } N \neq 2. \end{cases} \tag{5.46}$$

and is therefore inversely proportional to the square of the numerical aperture as it is the case for phase-based nulling interferometers. We can see in Eq. (5.46) that the rejection ratio is minimal for a quasi-radial polarization distribution ($\delta_0 = 0$) and is infinite for quasi-azimuthal polarization distribution ($\delta_0 = \pi/2$).

Note that in the two-beam case, both phase- and polarization-based interferometers are mathematically equivalent. The quasi-radial and quasi-azimuthal polarizations correspond respectively to the cases where the polarization is along the baseline and perpendicular to the baseline.

5.4.2 Electric field distribution

In this section, we will only consider the case of three beams with quasi-azimuthal and quasi-radial polarizations as depicted in Figure 5.9(b).

The field distribution in the focal plane for quasi-azimuthal and quasi-radial polarizations are depicted in Figure 5.10(a) and Figure 5.10(b). We see that, as expected from the ray tracing model, the longitudinal field is equal to zero on-axis in the quasi-azimuthal case. The rejection ratio would therefore be infinite. For quasi-radial polarization, the longitudinal field is maximal on-axis, leading to a limited rejection ratio.

We can also show in the case of polarization-based interferometers that the rejection ratio is in very good agreement with Eq. (5.46). Therefore, we validated with rigorous diffraction theory all results obtained with a simple ray tracing approach.

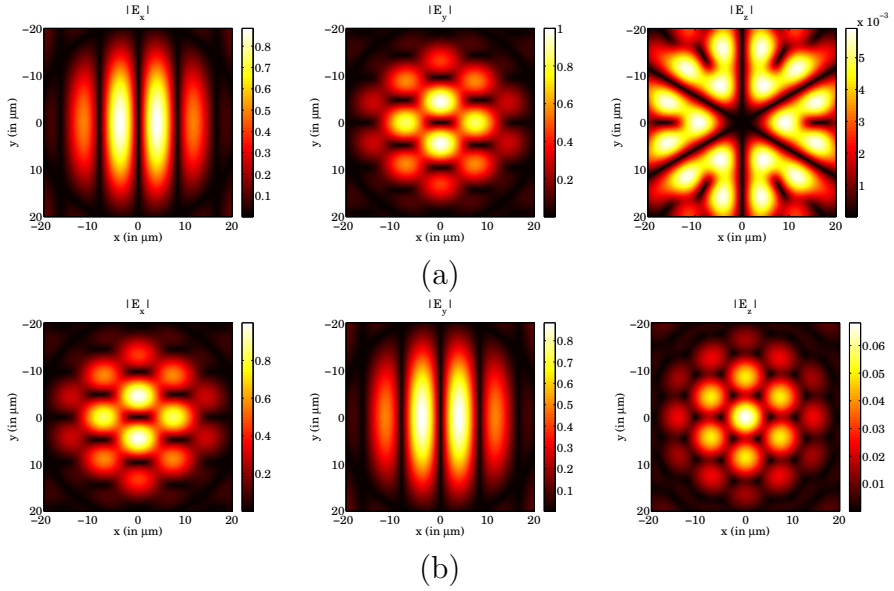

Figure 5.10: Three components of the electric field ($|E_x|$, $|E_y|$ and $|E_z|$) in the focal plane of the focusing optics in the case of a three-beam multi-axial combiner. The beams are in phase and are linearly polarized along either the azimuthal axis (a) or the radial axis (b). In each case, the three components of the field have been normalized to the largest component.

5.4.3 Single-mode fiber filtering for polarization-based nulling interferometers

In the case of a nulling interferometer based on polarization rotation, the transverse components of the electric field in the focal plane are given by

$$E_x = K \sum_{j=1}^{N} \{[G_1 \cos(\delta + k_{\phi,j}) - G_2 \cos(\delta - k_{\phi,j})] \exp[irk_r \cos(k_{\phi,j} - \phi)]\}, \tag{5.47a}$$

$$E_y = K \sum_{j=1}^{N} \{[G_1 \sin(\delta + k_{\phi,j}) + G_2 \sin(\delta - k_{\phi,j})] \exp[irk_r \cos(k_{\phi,j} - \phi)]\}. \tag{5.47b}$$

The coupling efficiencies to the orthogonal fiber modes are given by

$$\begin{aligned} \xi_{o,-} \quad = \quad & -2\pi K G_1 \sum_{j=1}^{N} \sin(\delta + k_{\phi,j}) \int_0^{\infty} J_0(rk_r) A_1(r)\, r\, dr \\ & -2\pi K G_2 \sum_{j=1}^{N} \sin(\delta - k_{\phi,j}) \int_0^{\infty} J_0(rk_r) A_1(r)\, r\, dr \\ & -2\pi K G_1 \sum_{j=1}^{N} \sin(\delta - k_{\phi,j}) \int_0^{\infty} J_2(rk_r) A_2(r)\, r\, dr \\ & -2\pi K G_2 \sum_{j=1}^{N} \sin(\delta + k_{\phi,j}) \int_0^{\infty} J_2(rk_r) A_2(r)\, r\, dr \end{aligned}, \tag{5.48}$$

and

$$\begin{aligned}\xi_{e,-} &= -2\pi K G_1 \sum_{j=1}^{N} \cos\left(\delta + k_{\phi,j}\right) \int_0^\infty J_0\left(r k_r\right) A_1\left(r\right)\, r\, dr \\ &\quad +2\pi K G_2 \sum_{j=1}^{N} \cos\left(\delta - k_{\phi,j}\right) \int_0^\infty J_0\left(r k_r\right) A_1\left(r\right)\, r\, dr \\ &\quad +2\pi K G_1 \sum_{j=1}^{N} \sin\left(\delta - k_{\phi,j}\right) \int_0^\infty J_2\left(r k_r\right) A_2\left(r\right)\, r\, dr \\ &\quad -2\pi K G_2 \sum_{j=1}^{N} \sin\left(\delta + k_{\phi,j}\right) \int_0^\infty J_2\left(r k_r\right) A_2\left(r\right)\, r\, dr\end{aligned} . \tag{5.49}$$

Since $\sum_{j=1}^{N} \cos\left(k_{\phi,j}\right) = \sum_{j=1}^{N} \sin\left(k_{\phi,j}\right) = 0$, both coupling efficiencies are equal to zero,

$$\xi_{o,-} = \xi_{e,-} = 0. \tag{5.50}$$

For nulling interferometers based on the rotation of polarization, light coming from an on-axis point source is not coupled in the fiber. The rejection ratio will therefore be infinite for any number of beams, any numerical aperture and any incoming polarization. Since the coupling efficiencies are rigorously equal to zero for any polarization and any numerical aperture and by linearity of the coupling efficiencies, we conclude that the results obtained in this section are also valid in the case of extended beams.

For the coupling efficiencies corresponding to constructive interference, we find after calculations

$$\xi_{o,+} \approx -2\pi K G_1 I_1 \begin{cases} 2\sin\delta, & \text{if } N = 2, \\ Ni/2 \exp\left(-i\delta\right), & \text{if } N \neq 2, \end{cases} \tag{5.51}$$

and

$$\xi_{e,+} \approx -2\pi K G_1 I_1 \begin{cases} 2\cos\delta, & \text{if } N = 2, \\ N/2 \exp\left(-i\delta\right), & \text{if } N \neq 2. \end{cases} \tag{5.52}$$

The output power corresponding to constructive interference is then given by

$$P_{out} = 4\pi^2 K^2 \left|G_1 I_1\right|^2 P \begin{cases} 4, & \text{if } N = 2, \\ N^2/2, & \text{if } N \neq 2. \end{cases}, \tag{5.53}$$

Comparing to phase-based interferometers (Eq. (5.36)), we see that in the case of two beams, the output power is nearly identical. However, for $N > 2$, the efficiency of a polarization-based interferometer is only half the efficiency of a phase-based interferometer. The price to pay to reach an infinite rejection ratio for any number of beams, any numerical aperture and any incoming polarization is therefore a loss of half the flux coming from the planet.

5.5 Conclusions

We performed a detailed analysis of multi-axial beam combination for nulling interferometry. We first used a simple ray-tracing model to illustrate the problem. With that model, we have shown that a longitudinal field is created by the focusing optics. This longitudinal component drastically limits the performance of the interferometer. We have shown that the rejection ratio is inversely proportional to the square of the numerical aperture and, except in the two-beam case, is independent of the polarization. In the case of a two-beam interferometer, the rejection ratio would be limited if beams were initially linearly polarized along the baseline. If the polarization is perpendicular to the baseline, the rejection ratio is theoretically infinite. We also investigated the case of nulling interferometers based on rotation of the polarization. We have seen that the rejection ratio is also in this case inversely proportional to the square of the numerical aperture, is minimal for quasi-radial polarization and infinite for quasi-azimuthal polarization.

We then performed a three-dimensional electric field analysis in the focal plane of a multi-axial nulling interferometer using rigorous diffraction theory. With that model, we analyzed the electric field distribution in the case of two- and three-beam nulling interferometers. We have shown that results obtained with rigorous diffraction theory were in very good agreement with the results obtained by ray tracing, therefore confirming these results. In a typical set-up with $\mathrm{NA}_{\mathrm{eff}} = 0.06$, the rejection ratio would be of the order of $10^2 - 10^3$ if both polarizations are used, which is too low for Earth-like exoplanet detection.

We also have investigated the filtering capabilities of a single-mode optical fiber placed at focus of a multi-axial beam combiner with respect to the longitudinal polarization issue. We have seen that the transverse magnetic fields of the fundamental modes are centro-symmetric functions. As a consequence, any incoming field with anti-symmetric transverse electric fields will not be coupled into the fiber. The fiber is therefore a perfect filter for these anti-symmetric transverse electric fields.

We have given a rigorous analytical expression for the coupling efficiencies and for the rejection ratio in the case of ray-like beams. We have seen that the rejection ratio in a three-beam phase-based nulling interferometer is in good approximation inversely proportional to the fourth power of the numerical aperture. For any other number of beams, the theoretical rejection ratio is infinite regardless of the polarization. We have also shown that, for the case of polarization-based nulling interferometers, the rejection ratio would be theoretically infinite for any number of beams, any numerical aperture and any incident polarization. However, this infinite rejection ratio occurs at the expense of half the photon flux coming from the planet.

Finally, we have validated these results with numerical simulations in the case of finite-size beams. Except in the three-beam case, the rejection ratio is theoretically infinite for all polarizations. The fiber is therefore an essential component of these multi-axial nulling interferometers since it solves the fundamental problem of the longitudinal polarization which occurs even in the perfect case (aberration-free). However, for three-beam com-

bination, light will be coupled into the fiber. The rejection ratio is therefore limited for both polarizations. We further have shown that the rejection ratio is, for small numerical apertures, inversely proportional to the fourth power of the numerical aperture of the system, which leads to less stringent requirements. Indeed, with a typical $\mathrm{NA_{eff}} = 0.06$, the rejection ratio would be of the order of 10^6 or 10^8 taking the interface into account (note that the interface would lead to a loss of photon flux). In this case, the single-mode fiber does not completely filter out the incoming electric field. However, the amount of light coupled in the fiber in the case of destructive interference is sufficiently low to allow Earth-like exoplanet detection. Therefore, a single-mode fiber is also essential in the three-beam case. The fiber is also an essential component of a polarization-based multi-axial nulling interferometer, since it leads to a theoretically infinite rejection ratio for any number of beams regardless of the polarization.

With this study, we have shown a fundamental limitation of multi-axial beam combiners, which can be solved by means of fiber filtering. We conclude that the longitudinal field component should not prevent direct detection of Earth-like exoplanets.

Chapter 6

Experimental results

In this chapter, we present the experimental results obtained on two different set-ups. The first nulling interferometer uses delay lines as phase shifters in order to demonstrate the principle of nulling interferometry without achromatic phase shifters [28, 52, 70]. In the second interferometer, destructive interference is achieved by using polarization properties of light [69, 71, 72] (see Chapter 3). We will then show, in Section 6.3, the experimental validations of the findings of Chapter 4.

6.1 Nulling interferometry without achromatic phase shifters

It has been shown that high rejection ratio is possible with delay lines only as phase-shifters [28, 52]. In a wide spectral band, the chromatism induced by the delay lines would drastically limit the rejection ratio. This problem is overcome by increasing the number of beams. Indeed, in the family of interferometers proposed by Mieremet [53], a larger number of beams allows less stringent requirements in terms of achromaticity.

An experimental set-up has been built to demonstrate this principle. In this section, we will present and discuss the latest results obtained with this set-up.

6.1.1 Principle

In the case of a three-beam interferometer with an amplitude distribution $(1, 2, 1)$, the generally proposed interferometer is the Degenerated Angel Cross (DAC) where the phases of the three beams are given by $(0, \pi, 0)$. The idea proposed by Mieremet [53] is to use for the third beam a phase of 2π instead of 0. The 2π phase shift may seem trivial but it would lead to a higher rejection ratio. Indeed, in order to reach the π phase shift, a certain phase shifter is used. Since the phase-shifter is not perfect, the applied phase shift will be $\pi + \epsilon(\lambda)$ instead of π, leading to a limited rejection ratio. If an identical phase shifter is used to reach the 2π phase shift, the applied phase shift will be $2\pi + 2\epsilon(\lambda)$. As

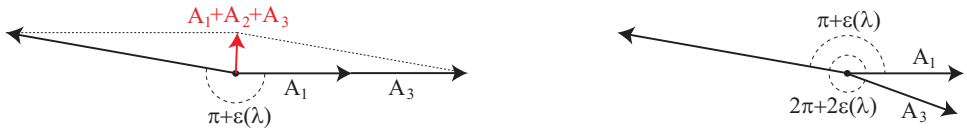

(a) (b)

Figure 6.1: Combination of three beams with an amplitude distribution of $(1, 2, 1)$ and a phase distribution of (a) $(0, \pi, 0)$ and (b) $(0, \pi, 2\pi)$.

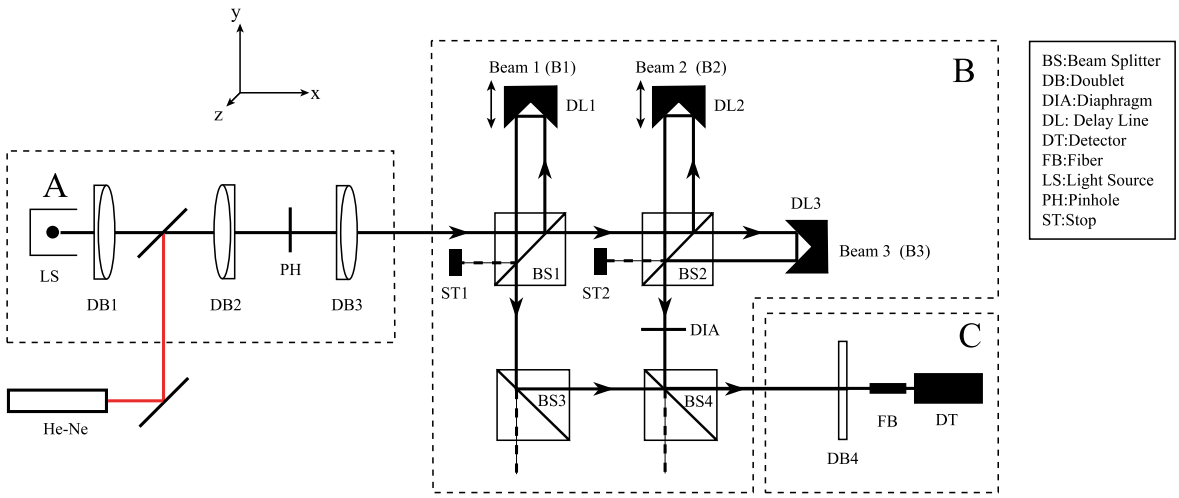

Figure 6.2: The experimental set-up can be divided in three blocks: the star simulator (A), the interferometer (B) and the detection stage (C).

depicted in Figure 6.1, this would lead to a much smaller residual intensity and therefore to a much higher rejection ratio.

The same can be applied to a larger number of beams. It is shown [53] that increasing the number of beams would lead to a higher rejection ratio (for a fixed ϵ) or less stringent requirements in terms of achromaticity (for a fixed rejection ratio). The latter gave the idea of using very chromatic phase shifters such as delay lines to reach the required phase shifts. Indeed, with such a chromatic phase shifter, a rejection ratio of 10^6 in a wide spectral band (typically 8–12 μm) can be reached with six beams. This was a very promising idea since the original plan of the DARWIN mission was to use six telescopes. Furthermore, delay lines are very easy to implement and are anyhow necessary for optical path difference corrections.

6.1.2 Experimental set-up

The experimental set-up previously built in our lab [52] is depicted in Figure 6.2. It is a three-beam nulling interferometer. It can be divided in three blocks: the star simulator (A), the interferometer (B) and the detection stage (C).

In the star simulator, light from a Xe-arc light source (LS) is focused onto a 5 μm-pinhole (PH), acting as a point source. Light is then collimated with a doublet (DB3) to form a 8-mm beam. With color filters, we set a spectral band ranging from 500 to 650 nm. Furthermore, for alignment purposes, we use a He-Ne laser focused onto the same pinhole using a folding mirror.

The interferometer consists of four beam-splitters (BS) to create and recombine three beams. Each of these three beams goes, before recombination, to different retro-reflectors acting as delay lines. The relative optical path differences between the three beams can be varied by changing the position of the delay lines (DL) via piezo-actuators.

After recombination, the beams are sent to a single-mode optical fiber (FB) for modal filtering [31]. The fiber is then connected to a power meter (DT) to detect the resulting power.

The interference pattern is built by measuring the intensity as a function of the position of the delay lines. We define the rejection ratio as the ratio between the maximal and the minimal intensities of the interference pattern.

6.1.3 Previous results

In this experimental set-up, a rejection ratio of 10^6 is not possible due to the chromatism induced by the delay lines and the limited number of beams. With two beams, the theoretical rejection ratio that we could reach in such a wide spectral band is of the order of 100. The three-beam interferometer would allow a rejection ratio of a few thousands with the appropriate amplitude distribution.

The optimal amplitude ratio is 1:2:1, which corresponds to a power ratio of 1:4:1. Reaching this amplitude distribution in an achromatic way without affecting the phase is not trivial. For that purpose, we use a diaphragm that limits the size (and therefore the power) of two of the three beams. Note that we have shown that this diaphragm can distort the spectral shape of the beams due to two different effects: the diffraction by a diaphragm (or by a sharp edge) and the coupling efficiency of the beams into the single-mode optical fiber are wavelength-dependent in such a way that beams with different shapes (or wavefronts) will have different wavelength-dependent coupling efficiencies and therefore different wavelength-dependent phases and amplitudes) [73].

The goal of the experiment was to show that the optimal amplitude ratio would lead to a relatively high rejection ratio compared to the conventional 1:1:1 amplitude distribution. The theoretical and measured rejection ratios [52] are listed in Table 6.1. We see that the equal-amplitude rejection ratio matches the expectations much better than in the case of the 1:2:1 amplitude distribution. In the following sections, we investigate possible reasons for such a low rejection ratio.

Amplitude distribution	Expected rejection ratio	Measured rejection ratio
1:1:1	275	188
1:2:1	3100	42

Table 6.1: Expected and measured rejection ratios in the case of a three-beam nulling interferometer. The spectral band ranges from 500 to 650 nm.

6.1.4 Spectral measurements

In order to achieve a rejection ratio of a few thousands, the intensity of the different beams should be matched with an accuracy of the order of 1 %. In a monochromatic set-up, this is easily achieved using amplitude-matching devices such as a knife-edge, a diaphragm, ... In a wide spectral band, however, this condition must be fulfilled for each wavelength, implying that each component must be achromatic or identical for each beam.

Spectral mismatchings have already been pointed out in this set-up [52] but, because of low light levels, only indirect measurements of the spectra were possible by Fourier analysis of pairwise interferograms. In theory, a Fourier transform of the recorded interferogram is a direct measurement of the spectrum. However, this is only true if the two interfering beams have identical spectra. In order to point out spectral mismatching between the two beams, some additional information is needed. In our set-up, the spectra of all beams could be indirectly calculated by using the fact that each beam was involved in two different pairwise interferograms. In order to confirm the spectral mismatching pointed out by this technique, we performed direct measurements, using two different methods.

At first, we compared the intensity of the different beams at certain specific wavelengths, using narrow-band interference filters (10 nm FWHM at the central wavelengths 502, 551, 576, 594 and 643 nm). In order to see whether the single-mode fiber affected the spectrum, measurements have been performed both before and after the fiber. The results are shown in Figure 6.3(b). Each point represents the relative intensity of the first (B1) and the second (B2) beams with respect to the third beam (B3). In an ideally achromatic set-up without any spectral mismatching, these relative spectra would be constant over the spectral band.

In the second set of measurements, we used a multi-mode fiber spectrometer to directly measure the whole spectra. Two series of measurements of the three beams are depicted in Figure 6.3(a), where some numerical filtering was applied in order to smoothen the spectra. We see that, for each beam, the two series of measurements look very different. Indeed, the fiber was not very stable and the spectra were strongly depending on the alignment or the bending of the fiber. As a conclusion, absolute measurements as such were not reliable. Nevertheless, as long as we keep the same configuration for all the beams, we can compare the spectra in a more reliable way. Indeed, if we compare these two series of spectra with the spectrum of the third beam, (see Figure 6.3(b)), we see that the relative measurements are quite repeatable while the absolute spectra were totally different. Furthermore, we see that they match quite nicely the first measurements performed with the interference filters, confirming the reliability of both methods. All measurements show large spectral

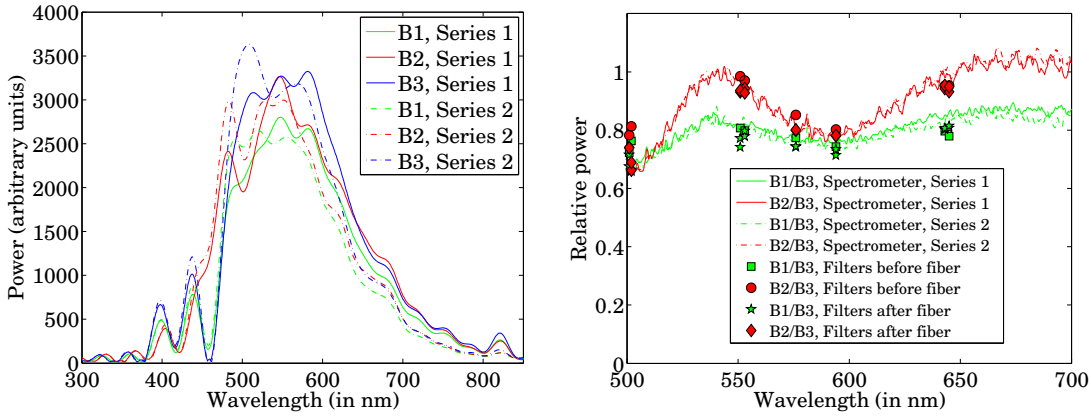

(a) (b)

Figure 6.3: (a) Spectra of the three beams (B1, B2, B3) measured with a multi-mode fiber spectrometer. A numerical low-pass filter has been applied to remove the noise. (b) Relative spectral measurements with interference filters (individual marks) and a multi-mode fiber spectrometer (lines). For each method, two series of measurements have been performed.

mismatchings (see Figure 6.3(b)), mainly between the second and the third beams B2 and B3 (more than 20% mismatching).

As already mentioned previously, amplitude-matching in a wide spectral band is not an easy task, since the amplitude-matching method can also affect the phase and the shape of the spectrum. Indeed, measurements of the spectra with a knife-edge or a diaphragm showed that these devices affect the shape of the spectrum, but the measurements depicted in Figure 6.3(b) already show unacceptable mismatchings even without any amplitude-matching device. Another possible reason for spectral mismatching would be the wavelength-dependent coupling efficiency to the single-mode optical fiber [73]. Different coupling efficiencies could be caused by misalignments or aberrations, but as we can see on Figure 6.3(b), the influence of the fiber is not so important. Indeed, measurements have been performed before and after the fiber and they do not show significant differences. Another possible reason would be differences in the coatings of the beam-splitters. Indeed, by swapping two of the beam-splitters, we found similar results but this time with the most important spectral mismatching between the first and the third beams. From this measurement, we conclude that the spectral mismatching is thus mainly caused by coating imperfections of the beam-splitters.

To correct for this mismatching, we should either replace the beam-splitters or find a way to chromatically adapt the amplitudes. The latter is not experimentally straightforward but might be an interesting option since, as seen in Chapter 2 [59], a much higher rejection ratio (theoretically infinite) could be reached.

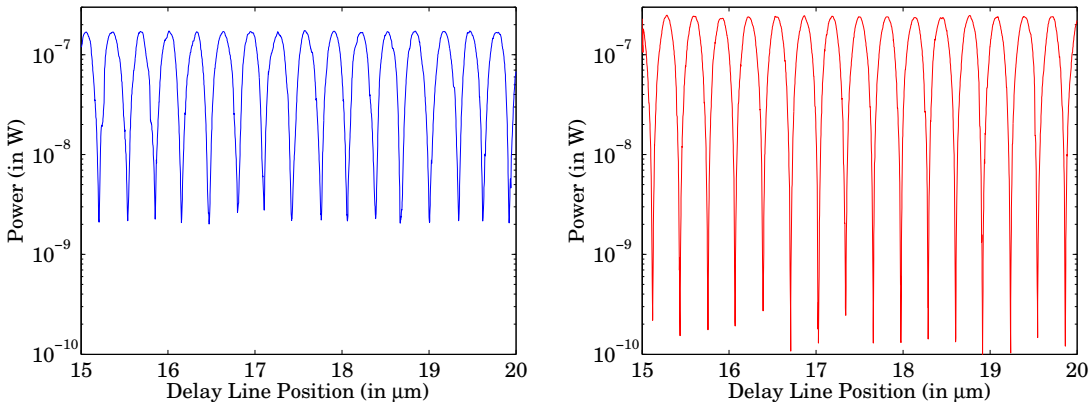

Figure 6.4: Interference patterns with laser light (He-Ne) without polarizer between (a) beams 1 and 3 ($R = 87$) and (b) beams 2 and 3 ($R = 2770$).

6.1.5 Polarization measurements

In order to check the alignment of the set-up, we performed two-beam interferometry with a He-Ne laser (see Figure 6.4). We recorded a much higher rejection ratio between beams B2 and B3 than between beams B1 and B2 and between beams B1 and B3 (see Table 6.2).

In a monochromatic set-up, amplitude matching is trivial and phase matching is also easily performed by changing the position of the delay line with 1-nm steps. Thus, in this case, the only remaining possibility for such a relevant discrepancy should come from polarization mismatching. This problem can be solved (in the monochromatic case) by placing a linear polarizer (Glan-Laser polarizer) after recombination before the single-mode optical fiber. Measurements with and without polarizer are summarized in Table 6.2, where we can see that the rejection ratios are of the same order of magnitude for each two-beam combination when we use a linear polarizer after recombination.

	B1 and B2	B1 and B3	B2 and B3
No polarizers	94	87	2770
One GL-polarizer	15000	5140	5710
Two GL-polarizers	6390	18000	/

Table 6.2: Measured rejection ratios in the case of a two-beam monochromatic nulling interferometer without polarizers, with one Glan-Laser polarizer after beam recombination and with Glan-Laser polarizers before splitting and after recombining the beams.

In order to quantify these polarization mismatchings, we directly measured the polarization of the three beams with the He-Ne laser (before the single-mode fiber). For each beam, we measured the intensity after a linear polarizer oriented at 0° (I_0), 45° (I_{45}), 90° (I_{90}) and 135° (I_{135}). From these intensities, we can calculate three of the Stokes

parameters using

$$\begin{aligned} S_0 &= I_0 + I_{90}, \\ S_1 &= I_0 - I_{90}, \\ S_2 &= I_{45} - I_{135}. \end{aligned} \tag{6.1}$$

With the general state of polarization being an ellipse, we can qualify the polarization of each beam by an ellipticity ϵ and an angle α giving the orientation of the ellipse (the direction of rotation is only determined by the fourth Stokes parameter). The orientation α and the ellipticity ϵ can be calculated from the Stokes parameters using

$$\begin{aligned} \tan 2\alpha &= \frac{S_2}{S_1}, \\ \cos 2\epsilon &= \sqrt{\frac{{S_1}^2+{S_2}^2}{{S_0}^2}}. \end{aligned} \tag{6.2}$$

The polarization measurements are depicted in Figure 6.5. Each point represents a measurement in the ellipticity-orientation domain and the rectangle around that point represents the uncertainty of the measurement. Even though the uncertainties were relatively important, we clearly see three different clusters of points, each of them representing one beam. These measurements confirm the presence of polarization mismatchings between the beams. We see in Figure 6.5 that the ellipticities corresponding to beams B2 and B3 are similar. B1 has a different ellipticity but a comparable orientation to B2. Considering the results of Table 6.2, we conclude that this ellipticity change is more critical than the orientation mismatching since both rejection ratios involving beam B1 are very low. Indeed, by calculating the theoretical rejection ratios obtained with the measured polarization, we find similar results to the measured rejection ratios: the rejection ratios between beams B1 and B3 and between B1 and B2 is one order of magnitude lower than the rejection ratio between beams B2 and B3.

The reason for these polarization mismatchings is probably some birefringence induced in the beam-splitters. Note that these measurements have only been performed for one wavelength. Therefore, it does not give full information concerning the entire spectral band. Nevertheless, it allows us to think that similar mismatchings are also present at other wavelengths.

6.1.6 Latest results

In Section 6.1.4, we showed that there are spectral mismatchings between the beams in our set-up. One way to reduce this problem is to limit the spectral band using color filters to a region where, as it can be seen in Figure 6.3(a), the mismatching was less pronounced. The results shown here are performed using this reduced spectral band ranging from 550 to 700 nm.

The polarization mismatching reported in Section 6.1.5 is also not trivial to solve. Using a linear polarizer after recombination provides quite good results with monochromatic light. Unfortunately, in a wide spectral band, the induced birefringence will give rise after the linear polarizer to different wavelength dependent amplitudes and phases which cannot be easily compensated for.

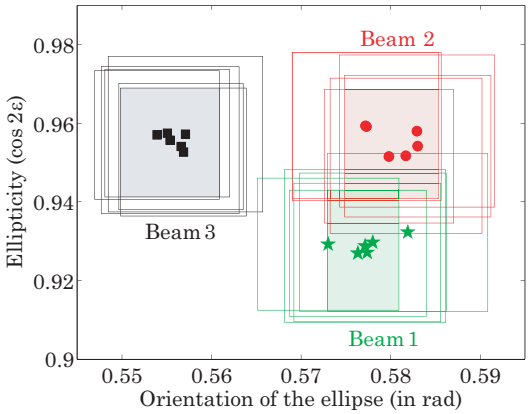

Figure 6.5: Polarization of the three beams with laser light (He-Ne) represented by their ellipticity and long-axis orientation. Each point represents one measurement in the ellipticity-orientation space and the rectangles represent the uncertainty of these measurements. The semi-transparent rectangles are the intersection of all uncertainty boxes for each beam

.

The results, with laser and white light, with or without polarizers, are summarized in Table 6.3. We see that, with the laser, the two- or three-beam rejection ratio is of the order of 10^4. This finite rejection ratio is probably due to vibrations or non-perfect amplitude matching; the instability of the laser signal made the amplitude-matching difficult. The white-light measurements show no significant difference with or without polarizers, but as discussed above, this can be explained by the fact that polarization mismatchings can be wavelength-dependent.

	Two beams			**Three beams**
	B1 and B2	B1 and B3	B2 and B3	B1, B2 and B3
Laser				
No polarizer	94	87	2770	/
One polarizer	15000	5140	5710	11027
Two polarizers	6390	18000	/	/
White light				
No polarizer	/	40.8	46.8	101.7
One polarizer	/	107.7	74.2	82.2
Two polarizers	/	73.3	54.8	97.4

Table 6.3: Measured rejection ratios in the case of a two-beam and a three-beam nulling interferometer, with laser and white light. Measurements have been taken without polarizer, with one polarizer after recombination or with one polarizer after recombination and one before splitting.

Two measurements using white light are depicted in Figure 6.6: (a) the measured interference pattern between beams 1 and 3, with one polarizer before splitting and one after recombination, and (b) the interference pattern of the three beams without polarizer. In the ideal case, the two-beam fringes should be symmetric with respect to the maximum

but we clearly see in Figure 6.6(a) that it is not the case. We can also see in Figure 6.6(b) that the minimum and maximum of the interference pattern have approximately the same ordinate. In terms of phase-shifts with respect to the maximum, we can say that the minimum is located at $(\Delta\phi_1 = 0, \Delta\phi_2 = \pi)$ while it has been shown [53] that it should always be at $(\Delta\phi_1 = 2\pi, \Delta\phi_2 = \pi)$ (not depicted here) for any amplitude distribution and any spectral mismatching.

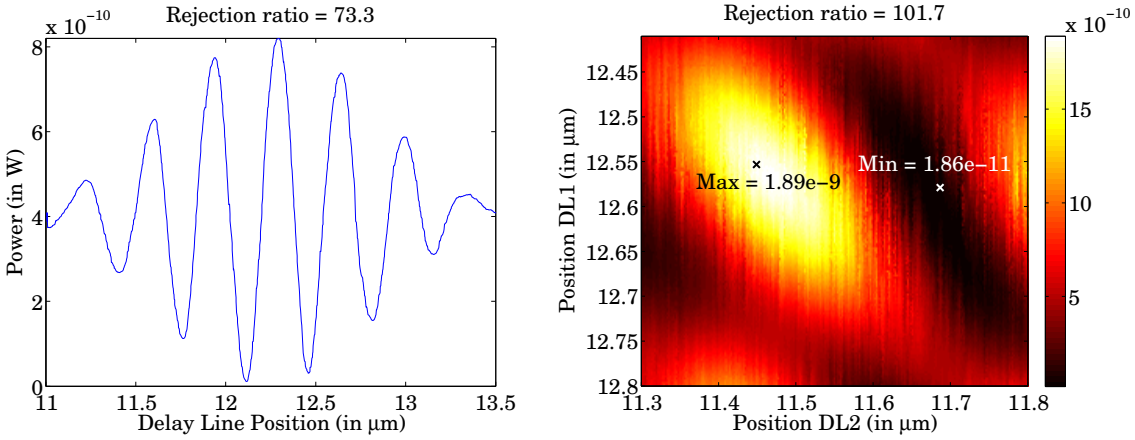

(a) (b)

Figure 6.6: Measured white light interference patterns (a) with two beams ($R = 73$) and (b) three beams ($R = 102$) .

One phenomenon that could account for both asymmetries or "defects" in the interference patterns is dispersion. This can be understood if one considers the interference between two beams. As shown in Chapter 4, if one of the beams has a longer path in glass, it will give rise to an asymmetric pattern. The "level" of asymmetry depends on the path difference in glass. Dispersion can also explain the measured three-beam interference pattern. In a wide-band interferometer, dispersion is most likely to occur, since all beams encounter different optics with different wavelength-dependent refractive indices. For instance, in our set-up, a slight misalignment of the beam splitters induces different path lengths inside the material. Dispersion might also arise from the inhomogeneity of the coatings or, in the case of a long-baseline ground-based interferometer, dispersion occurs mainly because of differences in water vapor content between the two arms of the interferometer. The effect of dispersion through glass plates and the validation of the theoretical predictions made in Chapter 4 will be presented in Section 6.3.

6.2 Polarization nulling interferometry

Theoretically, we have shown in Chapter 3 that it is possible to reach a high rejection ratio in a wide spectral band with commercially available components by using polarization properties. In this section, we will present the experimental results obtained with this technique.

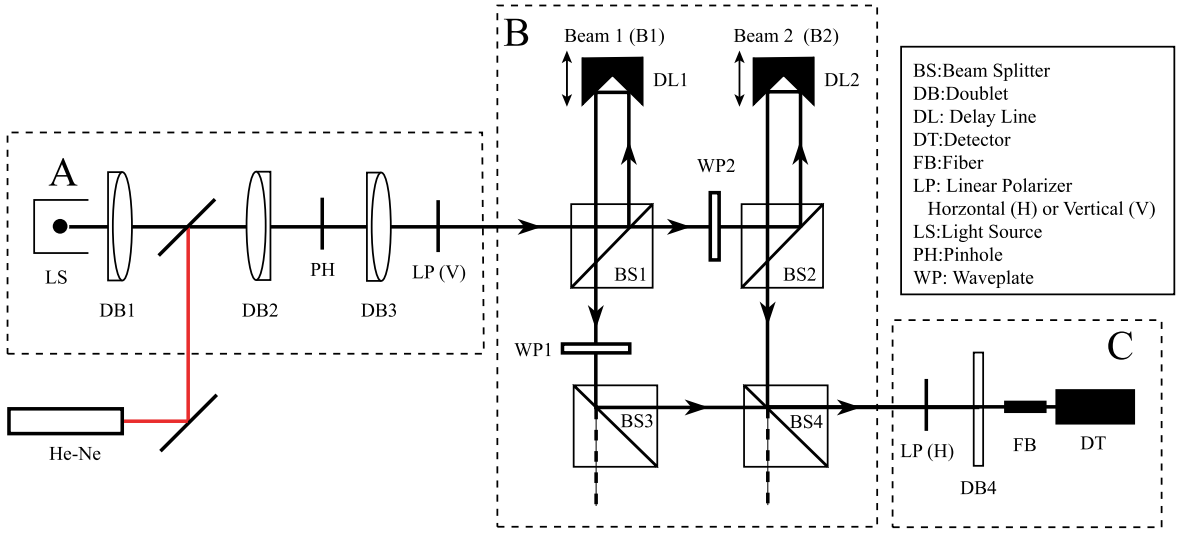

Figure 6.7: The experimental set-up presented in Section 6.1.2 has been adapted and changed into a two-beam polarization nulling interferometer.

6.2.1 First fringes

As a proof-of-principle, we performed our first measurements on the set-up presented in Section 6.1.2 and depicted in Figure 6.2, using only two beams. We see in Figure 6.7 a schematic drawing of the set-up adapted for polarization nulling interferometry. The only differences with the set-up of Section 6.1.2 are the orientation of the polarizers (they are crossed) and the additional waveplates. For these first measurements, we used multiple-order waveplates (half-waveplate at 632 nm).

In order to check the alignment, we first performed measurements with monochromatic light (He-Ne laser). Results are depicted in Figure 6.8. We see that a rejection ratio of 10^4 has been reached, which is similar to previous results obtained with this set-up.

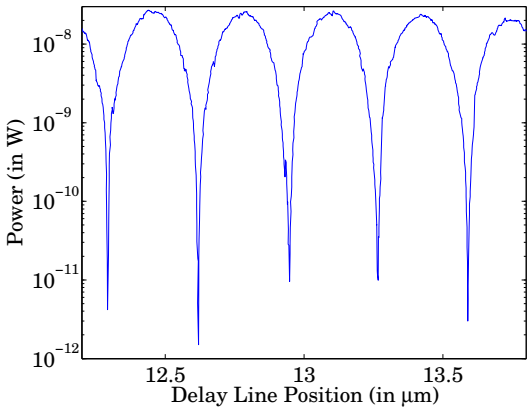

Figure 6.8: Experimental interferometric results with He-Ne laser and multiple-order half-waveplates.

The spectrum of the white light covers the wavelength range from 550 to 750 nm but since

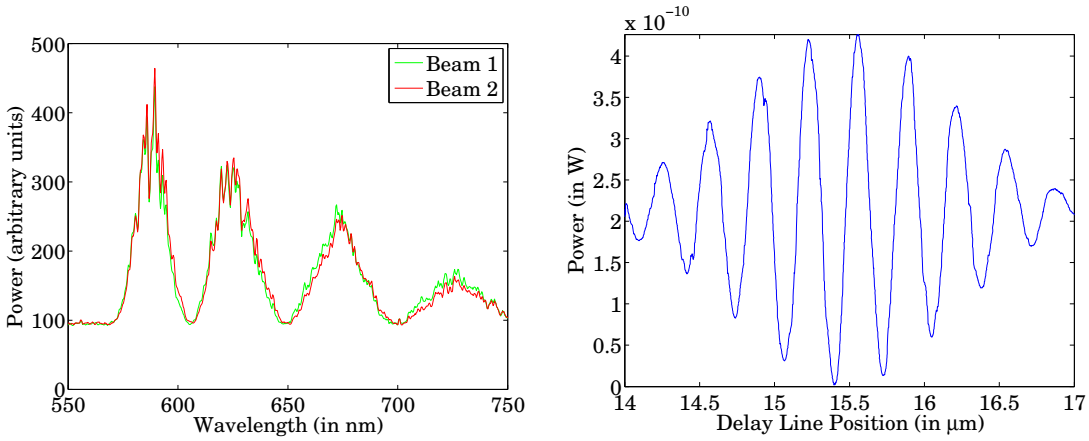

(a) (b)

Figure 6.9: Experimental interferometric results with white light and multiple-order half waveplates. (a) Spectra of the two beams due to the multiple-order waveplates and (b) white-light interference pattern with a rejection ratio of 230.

we use multiple-order waveplates the spectrum is not fully transmitted, as shown explicitly in Figure 6.9(a). As we can see, the waveplates are half-waveplates at 632 nm (maximum of transmission). The measured interference pattern is depicted in Figure 6.9(b). We reached a rejection ratio of 230 in a wide spectral band (which is not bad considering the large spectral mismatchings between the beams in the set-up). But similarly to what has been observed in Section 6.1.6, the interference pattern of Figure 6.9 is not symmetric with respect to the minimum. This is due to dispersion as discussed in Chapter 4. An experimental attempt to correct this asymmetry will be presented in Section 6.3.

6.2.2 Design of a new experimental set-up

As mentioned in Section 6.1, important spectral mismatchings of the order of 20% over the spectral band have been pointed out. These spectral mismatches are mainly due to imperfections in the coatings of the beam-splitters. We also have observed important polarization mismatchings. Both amplitude and polarization mismatchings resulted in drastic limitations on the rejection ratio.

In this new design, we have paid attention not only to the fact of having identical beam-splitters but also to the symmetry of the optical paths for all beams. The set-up presented in Section 6.2.1 is not optically symmetric: the number of front- and back-transmissions and of front- and back-reflections are not the same for each beam. This lack of symmetry can be analyzed in the following way assuming that all beam-splitters are identical. The complex transmission coefficients of the beam-splitters are given by t_p, t_s, t'_p and t'_s and the complex reflection coefficients are given by r_p, r_s, r'_p and r'_s, where the subscript s or p refers to s- or p-polarization respectively, while the $'$ denotes a backside transmission or reflection. We can show that, in order to achieve perfect destructive interference in a

polarization-based interferometer, these coefficients must fulfill the conditions

$$\begin{gathered} t'_s = t_s \text{ and } t'_p = t_p, \\ t_p r_s = r_p t_s. \end{gathered} \tag{6.3}$$

These conditions must be fulfilled for all wavelengths in the spectral band. It is reasonable to think that the first condition in Eq. (6.3) is easily fulfilled: frontside and backside transmission coefficients are identical (which is not true for reflection coefficients). However, the second of these conditions is not trivially satisfied for all wavelengths. Note that this set-up is perfectly symmetric when used as a phase-based nulling interferometer as originally designed. The lack of symmetry only arises when the set-up is used as a polarization nulling interferometer.

Therefore, in order to solve the problem of these important mismatchings and lack of optical symmetry, we designed and fabricated a three-beam polarization nulling interferometer, as presented below.

Design

A schematic drawing of the set-up is depicted in Figure 6.10. It is a two-level three-beam polarization-based nulling interferometer. For simplicity, only a two-dimensional top-view of the set-up is represented in Figure 6.10. The light source and the beam splitting are on the upper level, while beam recombination and detection take place on the lower level.

The light source (LS) is a visible Xe arc source with a spectral band ranging from 450 to 750 nm. Light from this source is focused onto a single-mode optical fiber (OF). For alignment purpose, a He-Ne laser is focused onto the same optical fiber. A collimating optics (CO) system is used to collimate the light coming from the fiber to a diameter of 8 mm. The light is then linearly polarized using a Glan-Laser polarizer (LP).

With the help of three beam-splitters (BS), three identical beams are created. Each beam encounters a waveplate (WP). These waveplates must be as identical as possible but set at different orientations (see Chapter 3). Each beam passes through a parallel glass plate (DP) that can be tilted to compensate for eventual dispersion. The beams are then reflected backwards by cat's eye-type delay lines (DL). These delay lines are mounted on a micrometer screw for coarse OPD corrections and are fine-tuned using a piezo-activated mirror. The beams come back one level higher in such a way that they do not pass through the dispersion plates and the waveplates a second time. A two-level instead of a double-path set-up is needed since the waveplates should only operate in single path.

The beams are recombined with the same beam-splitters as the ones used for beam-splitting. Indeed, beam separation and combination are totally symmetric in this proposed set-up. The combined beams are then sent to a single-mode optical fiber for wavefront filtering and detection.

Some of the flat mirrors are actuated by piezo-elements to correct residual tip/tilt angular deviations between the beams. Note that the polarizers are used before beam separation

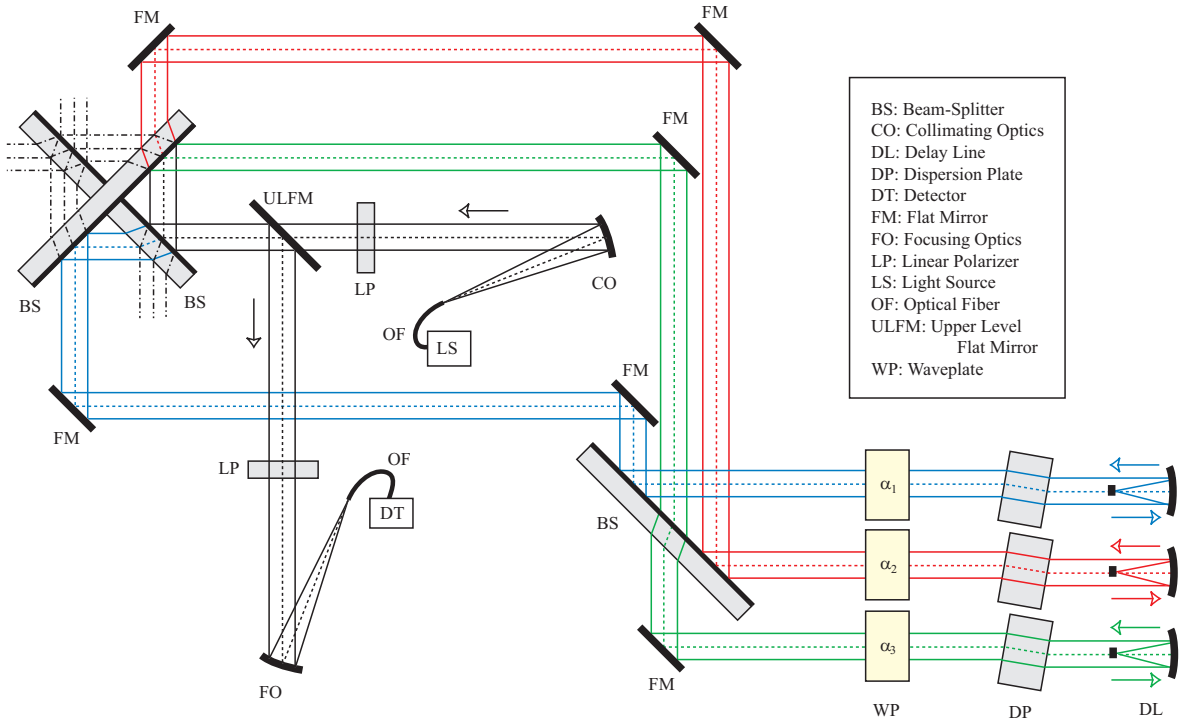

Figure 6.10: Design of a new experimental two-level set-up.

and after beam combination to make sure that no differential polarization orientation limits the rejection ratio.

Features

The set-up is a three-beam visible light polarization nulling interferometer. The waveplates can be replaced by an image-rotator or another device similarly affecting the polarization. Additionally, the set-up can also be converted into a traditional nulling interferometer by replacing the waveplates with an achromatic phase-shifter.

The set-up is entirely symmetric: all beams have the same number of frontside, backside-transmissions *and* reflections. As a consequence, if the beam-splitters are identical, all beams are perfectly identical, which was not the case in the set-up of Figure 6.7. In addition, the beam generator and the beam combiner are independently symmetric. Therefore, if the beam generator were to be replaced by three telescopes, the set-up would not loose its symmetry.

Three outputs of the beam-combiner (dash-dotted lines in Figure 6.10) can be used for complete three-beam end-to-end fringe tracking. Further study is needed to find a comparable fringe-tracking strategy in the case of a polarization nulling interferometer.

As mentioned in Chapter 3, accurate global amplitude matching can be achieved by rotation of the waveplates.

In this set-up, we also added glass plates to compensate for residual dispersion.

Tolerances

In this section, we review the requirements needed to reach a 10^5-rejection ratio in a broad spectral band. Some of these requirements are identical to standard requirements in nulling interferometry [62], while some other requirements are specific to polarization nulling interferometry (see Chapter 3). To find these tolerances, we assumed that all requirements have a uniform distribution. In practice, this is probably not true, since one effect will be dominant. The tolerances given here will therefore correspond to the worst case scenario.

- The absolute value of the transmission/reflection coefficients of the beam-splitters is not important in this design as long as the beam-splitters are identical. Since intensities should be matched within 0.1% [62], the transmission/reflection coefficients of the beam-splitters must be identical within 0.1%. The coatings of the beam-splitters should also be homogeneous within 0.1%.

- A wedge in a beam splitter introduces tip/tilt and position-dependent dispersion. The tip/tilt can be corrected, so can be the average dispersion. However, the position-dependent thickness in glass cannot easily be compensated for. After calculations, we found that the absolute wedge angle of the beam-splitters must be less than 1 mrad and the wedge angles must be identical for all beam-splitters within 10-20 μrad.

- A tip/tilt angle between the two beams induces an amplitude mismatching due to different coupling efficiencies with the single-mode fiber. In the monochromatic case, this can be solved with an amplitude-matching device. However, in a wide spectral band, this amplitude mismatching will be wavelength-dependent due to the chromatic coupling efficiencies [73] and therefore cannot be compensated for. The tip/tilt between two beams should be corrected within 5 μrad, which will be achieved by piezo-actuated tip/tilt mirrors.

- A wavefront quality of $\lambda/20$ RMS over the beam cross-sections is needed to have a 10^5 rejection ratio, because of the wavelength-dependent coupling efficiency with the single-mode fiber [73]. This number should be multiplied by two and by the square root of the number of optical surfaces for the equivalent requirement in terms of a single surface.

- The path difference in glass (BK7) should be corrected within 40 nm, which means that the rotation of a 20-mm dispersion plate should be accurate within typically 100 μrad.

- The extinction ratio of the linear polarizers should be at least 10^5 (see Chapter 3), as it is the case for the commercially available Glan-Laser polarizers.

- The absolute birefringence of the waveplates is not very important as long as they are identical. However, the differential birefringence between two different waveplates must be smaller than $\lambda/1000$ (see Chapter 3). Note that in order to meet this requirement, stress-free mounting should be used for all optical components in the various beam paths.

- The polarizers and waveplates must be rotated with an accuracy of 1 mrad (see Chapter 3).

The set-up has been designed and the optical components have been selected in order to meet these requirements. However, for many elements, the wavefront quality could not be guaranteed. All components have a surface quality of $\lambda/20$ RMS or better. This should limit the rejection ratio to around 10^4.

Prospects

At the time when these lines were written, all optical components arrived and the set-up was ready to use. Unfortunately, no experimental results could be obtained within the available time. We hope to perform two- and three-beam experiments during the coming months.

However, preliminary wavefront measurements at an intermediate position between beam splitting and beam recombination allow us to think that the rejection ratio will be of the order of $10^4 - 10^5$ at the highest. We noticed that the alignment of the delay lines is critical for the wavefront quality. The cat's eye-type delay lines might also lead to polarization mismatching: a beam linearly polarized at 45° becomes after the delay line slightly ellipitically-polarized (with an extinction ratio of 10^2 compared to 10^5 for the incoming beam). It is therefore important to send a pure s- or p-polarization to the delay line, in such a way that the waveplates used to achieve the destructive interference should be placed after the delay line.

Another limiting factor in our set-up may be the light level. The high requirement in homogeneity of the beam splitters led upon fabrication to fairly poor transmission and reflection coefficients of the order of 30%. Since each beam is transmitted or reflected six times by the beam-splitters, this leads to a loss in total transmission of more than a factor 10. We expect the total white-light power after coupling to the fiber to be of the order of 1 nW or less. With our current detector, this light level would only allow a rejection ratio of several thousands. However, we have a photodiode, which if used in combination with an amplifier should be able to detect powers as low as a few fW. This requires the realization of a good shield to prevent background light from reaching the detector. A good electronic shield is also needed because our long cables pick up all sorts of signal. We can also enhance the signal-to-noise ratio by chopping the useful signal at a specific frequency.

6.3 Effect of dispersion in a nulling interferometer

In order to validate the theoretical predictions that we have made in Chapter 4, we performed measurements using our table-top experimental set-up.

6.3.1 Set-up

Only two-beam measurements have been performed. For these measurements, we used the experimental set-up presented in Section 6.1.2 and depicted in Figure 6.2.

The required thickness of the additional glass plate is of the order of a few microns. For simplicity, we used a 5 mm-thick BK7 plate in each beam that was rotated in order to achieve the desired differential thickness. By measuring accurately the angle of rotation of the plates with a He-Ne laser, we could deduce the effective thickness of the plate using Snell's law and simple geometrical considerations.

6.3.2 Measurements

We performed measurements both with and without achromatic phase shifter.

Nulling without achromatic phase shifter

We first performed measurements without achromatic phase shifter. The rejection ratio as a function of the differential thickness is depicted in Figure 6.11(a). We see that the overall shape is very similar to the one expected: a central minimum when there is no differential dispersion and two main peaks when the thickness increases followed by two secondary minima and secondary maxima. However, we see that the position of the maxima and minima does not exactly coincide. This is probably due to slightly different spectra used in the simulations and in the experiment. Indeed, we used an additional filter to cut-off the infrared part of the spectrum. The final spectrum used in these measurements has not been measured. We also see that we found expected values for one of the maxima while significantly lower values have been found for the other maximum. This has been repeatedly measured and remains unexplained. A possible explanation would be the presence of additional non-compensated dispersion induced by the coatings of the beam-splitters and the mirrors, but this has to be confirmed.

In Figure 6.12, we see the recorded interference patterns corresponding to the different minima and maxima of the rejection ratio. All measured fringes are quite similar to the simulated ones, except for the fact that the measured fringe packets are somewhat wider. This is probably due the mismatching between the spectra in the simulations and in the experiment. As mentioned earlier, an additional filter has been used, making the spectrum narrower and therefore the fringes wider. We see, as expected, that the interference

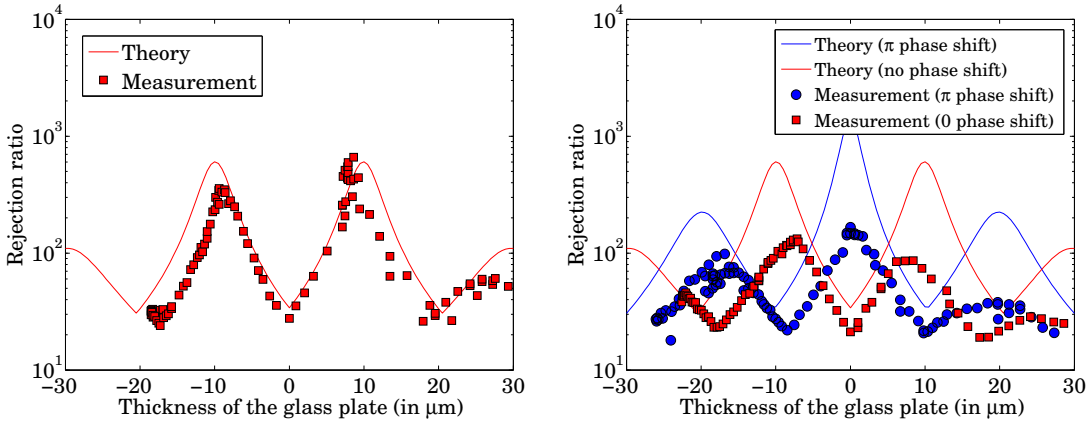

Figure 6.11: Measured rejection ratio as a function of the thickness of the glass plate d in the case of (a) a nulling interferometer without achromatic phase shifter and (b) a polarization nulling interferometer. In the latter, depending on the orientation of the waveplates, we have no phase shift or a π phase shift.

pattern corresponding to the central minimum of the rejection ratio is symmetric with respect to the maximal intensity (see Figure 6.12(a)), while for the two main peaks of the rejection ratio, the fringes are symmetric with respect to the minimal intensity (see Figures 6.12(b) and (c)). The fringes corresponding to the secondary minima start losing their symmetry (see Figures 6.12(d) and (e)).

Polarization nulling interferometer

In the second set of measurements, we used the set-up as a two-beam polarization nulling interferometer. We added achromatic waveplates in order to rotate the polarization by 180° and therefore have them act as an achromatic phase shifter [69] (see Chapter 3). With this configuration, we performed two series of measurements. For the first one, both waveplates had the same orientation (at $\pi/4$) and therefore no phase shift between the beams was introduced. For the second set of measurements, one waveplate was oriented at $\pi/4$, while the second one was oriented at $3\pi/4$, leading to an effective π phase difference between the two beams.

In Figure 6.11(b), we see the rejection ratio as a function of the effective thickness of the glass plate for both measurements. We can see that even though the curve has the predicted overall shape, the values are much lower than the ones expected: the maximal measured rejection ratio with this set-up was of the order of 10^2 instead of 10^3. The reason for this disagreement is not clear at this moment but it might be caused by polarization mismatching as pointed out in Section 6.1.5. This mismatching is difficult to quantify in a wide spectral band and is therefore complicated to take into account in the simulations.

Figure 6.13 depicts the recorded interference patterns corresponding to the different minima and maxima of the rejection ratio when an achromatic π phase shift is applied be-

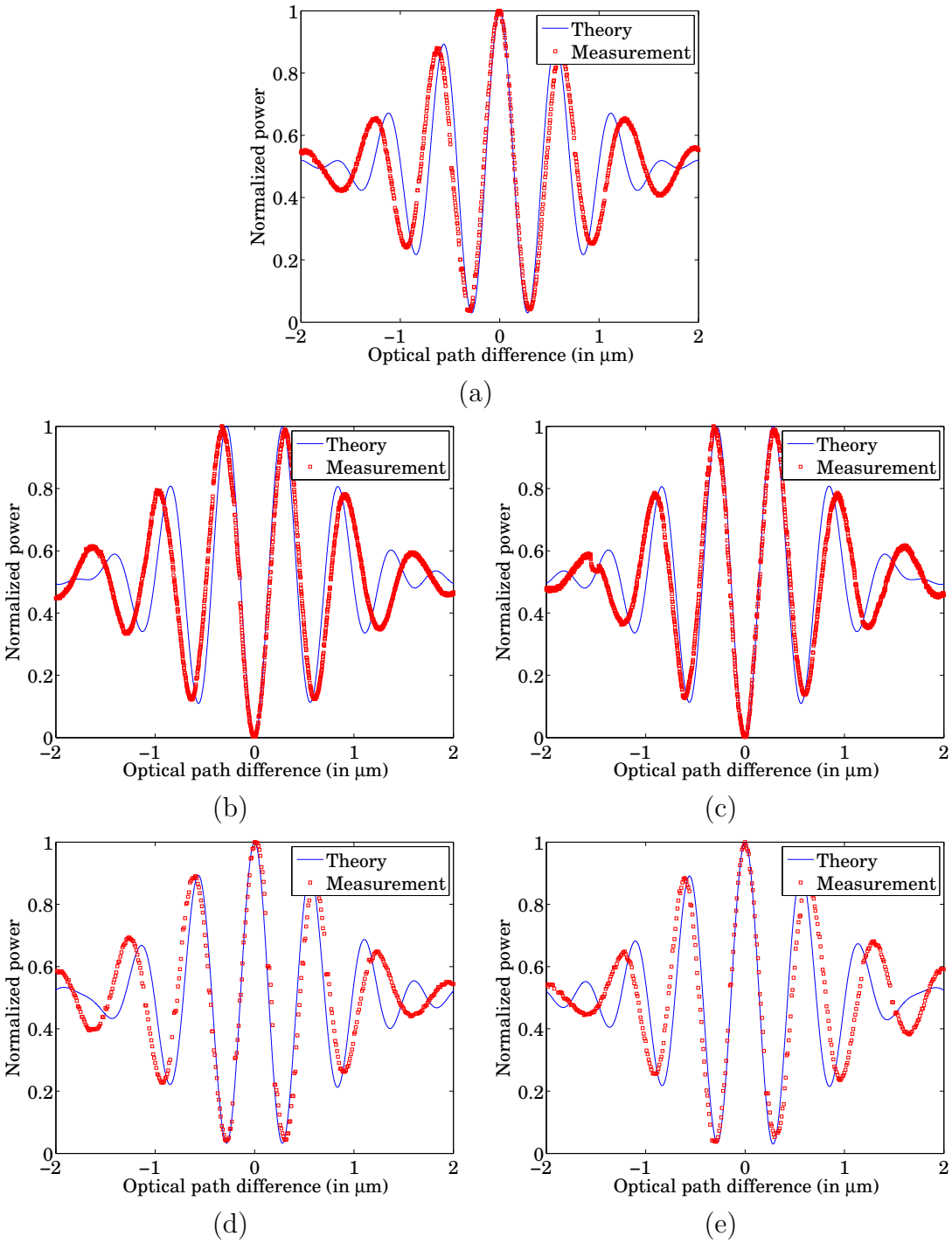

Figure 6.12: Measured fringes with a nulling interferometer without achromatic phase shifter for the following thicknesses of the introduced glass plate: (a) $d = 0$ μm, (b) $d = -10$ μm, (c) $d = 10$ μm, (d) $d = -20$ μm and (e) $d = 20$ μm

tween the beams. All measured fringes are quite similar to the theoretical ones, except for the width of the interference patterns due to a mismatching between the spectra in the simulations and in the experiment. As expected, we see that the interference pattern corresponding to the central maximum of the rejection ratio is symmetric with respect to the minimal intensity (see Figure 6.13(a)), while for the two first minima of the rejection ratio, the fringes are quasi-symmetric with respect to the maximal intensity (see Figures 6.13(b) and (c)). The fringes corresponding to the secondary maxima are more asymmetric (see Figures 6.13(d) and (e)). As expected, the pattern of Figure 6.13(b) (respectively (d)) is a mirrored version of Figure 6.13(c) respectively (e)) with respect to the zero-OPD point, which confirms their respective differential glass thicknesses d compared to the central maximum.

6.4 Conclusions

In the first section of this chapter, we have analyzed the reasons for the unexpected results previously obtained with a nulling interferometer without achromatic phase shifters. We measured, in a direct way, the spectra of the different beams with two different methods: with narrow-band interference filters and with a fiber spectrometer. We have shown that, even though the methods were not very reliable for absolute measurements, both methods gave very similar and repeatable results in a relative way. With these results, we have pointed out some important spectral mismatching (of the order of 20%) between the beams.

Next, we have measured polarization mismatchings and quantified them in the monochromatic case. We have seen that both ellipticity and orientation differ from one beam to the other, resulting in a drastically limited rejection ratio in the monochromatic case. We also have seen that, even though simple linear polarizers solve the problem in the monochromatic case, it is not straightforward to fix that problem in a wide spectral band.

In the second part of this chapter, we have implemented the concept of polarization nulling interferometry on our table-top two-beam experimental set-up. In the monochromatic case, we have reached a rejection ratio of 2.10^4, which is the maximum obtained with this set-up when used as a nulling interferometer without achromatic phase shifter. In a wide spectral band (from 550 to 750 nm), we reached a rejection ratio of several hundreds with conventional multi-order waveplates. This low rejection ratio can be explained by the already-pointed out spectral and polarization mismatchings and by different path lengths in glass.

We have also identified a lack of symmetry between the beams as another limitation of our set-up. Given these limitations, a new set-up has been designed. The design is a three-beam visible light polarization-based nulling interferometer. It is entirely symmetric with respect to the number of frontside and backside transmissions and reflections in the optical paths. It allows complete three-beam end-to-end fringe-tracking, accurate amplitude-matching and dispersion compensation. Internal modulation is also possible. The required quality and tolerances of all optical components have been analyzed so that

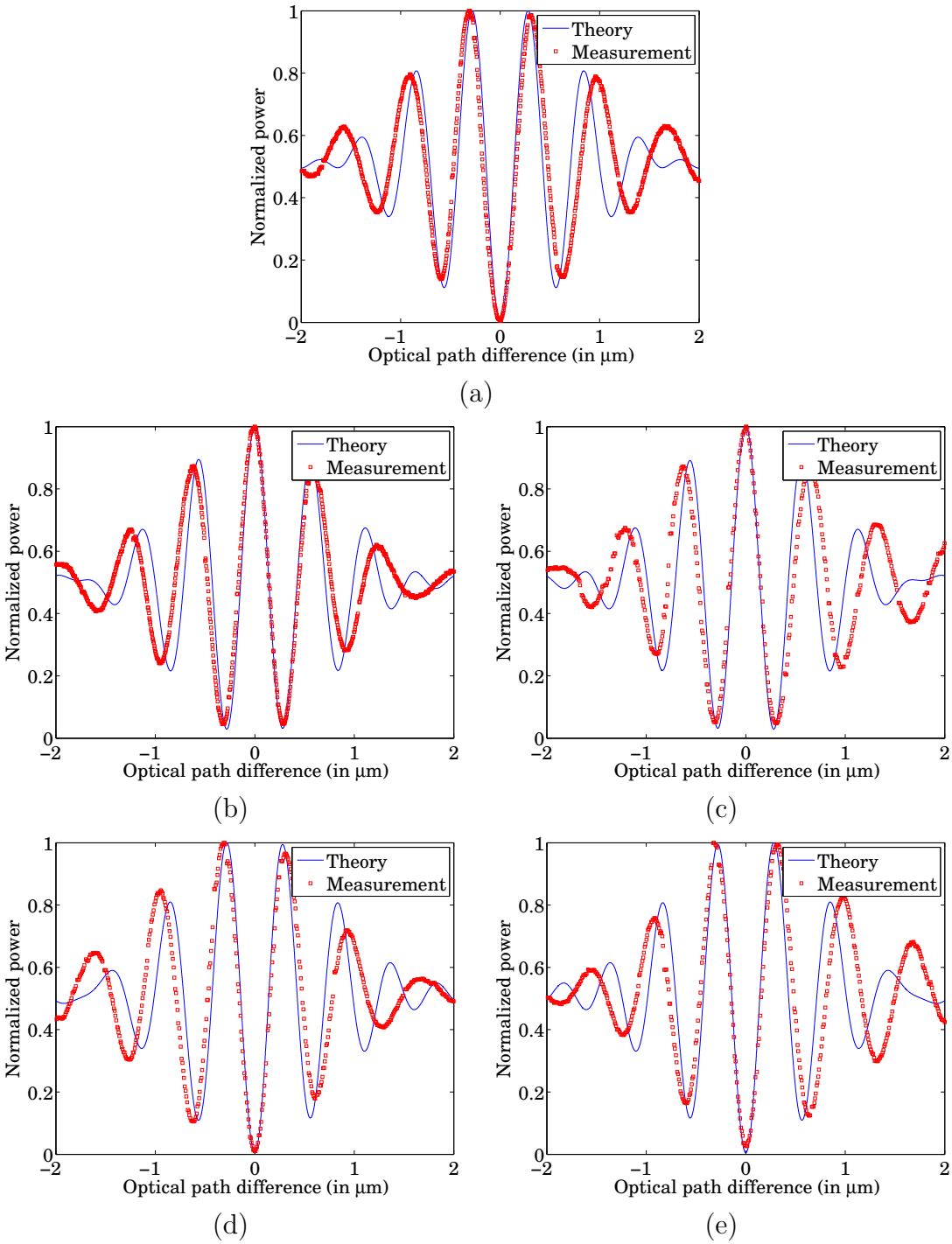

Figure 6.13: Measured fringes with a polarization nulling interferometer for different thicknesses of the introduced glass plate: (a) $d = 0$ μm, (b) $d = -10$ μm, (c) $d = 10$ μm, (d) $d = -20$ μm and (e) $d = 20$ μm

a rejection ratio of at least 10^5 can be reached in a wide spectral band.

Actual measurements with the designed set-up were not possible within the available time but we will hopefully perform two- and three-beam visible-light measurements during the coming months. Considering the intermediate, wavefront and polarization measurements using the actual components, a rejection ratio of $10^4 - 10^5$ is expected with a 40-50% bandwidth. Although this value is lower than the one initially aimed at while designing the set-up, it would still be the best performance achieved so far with a three-beam nulling interferometer.

Finally, in the last part of this chapter, we have validated experimentally our theoretical predictions made in Chapter 4 about the influence of dispersion in nulling interferometry. We measured the rejection ratio as a function of the thickness of the introduced glass plate with and without achromatic phase shifter. The overall shape of the interference patterns and of the rejection ratio curves were in good agreement with the theory. The main difference between theory and measurements is that the measured fringes were a little bit wider than expected and the positions of the maxima and minima of the rejection ratio were slightly different. Both these differences can be explained by a mismatching between the spectra used in the simulations and in the experiments. Another important difference between theory and experiment was that the values of the measured rejection ratio were significantly lower than expected. This is probably due to polarization mismatching between the beams.

Chapter 7

Discussion and conclusions

In this thesis, we have presented new perspectives in nulling interferometry by introducing methods and concepts that should allow a high rejection ratio in a broad spectral band. We therefore offered an alternative to the technically challenging achromatic phase shifters. These concepts are discussed, theoretically and numerically, in the first chapters of this thesis. We then have thoroughly analyzed the particular case of a multi-axial nulling interferometer and discussed its fundamental limitation with respect to longitudinal polarization. The last chapter is dedicated to the presentation of all experimental results obtained throughout this thesis research.

Using only achromatic components is not an absolute requirement in nulling interferometry. An infinite rejection ratio is possible with wavelength-dependent components in an infinitely wide spectral band as long as the phase-induced (resp. the amplitude-induced) chromatism is compensated by chromatic amplitudes (resp. phases). This concept, called "chromatism compensation", shows the interaction between amplitude and phase in nulling interferometry. Therefore, amplitude and phase should not be treated independently.

The amplitude-phase condition to have on-axis destructive interference for N beams can be generalized by assuming coherent but arbitrary and independent states of polarization for all beams. An infinite rejection ratio can therefore be achieved with beams with different but coherent polarizations. For instance, this can be realized with an achromatic polarization rotator. Another possible approach only involves off-the-shelf linear polarizers and conventional waveplates (achromatic or not) or similar devices such as an image rotator. With this approach, the spectral band in which a high rejection ratio can be reached is theoretically infinite, as long as light is transmitted. In terms of transmission in a broad band, zero-order or achromatic waveplates are preferable. This method has the advantage of providing internal modulation. Further studies must be performed to find an efficient modulation scheme in presence of extended sources and time-depending amplitude or phase instabilities. This scheme should involve four beams since the current plan for the Darwin mission is to make use of four telescopes. This type of interferometer also provides inherent amplitude-matching, pointing out the interaction between amplitude and polarization in such a nulling interferometer. Even though it has not been mentioned in this thesis, other types of nulling interferometer should be found by considering the general amplitude-phase-polarization interaction. For future research, it might be inter-

esting to look at hybrid nulling interferometers, where asymmetric transmission maps are obtained with achromatic phase shifters such as dispersive plates and internal modulation is performed using polarization.

Dispersion affects the performance of most nulling interferometers since all beams pass through different pieces of materials with different wavelength-dependent refractive indices. This changes the wavelength-dependent phase differences between the beams. In a nulling interferometer based on achromatic phase shifting, dispersion should be compensated for since it will automatically degrade the rejection ratio. However, dispersion can be used to optimize the performance of an interferometer by correcting the first-order chromaticity of the phase shift and therefore enhance the rejection ratio to such a level that Earth-like exoplanet detection would be possible with a three-beam interferometer without achromatic phase shifter.

A longitudinal field is created at the focus of a multi-axial nulling interferometer, due to the rotation of the vibration planes by the focusing optics. This longitudinal field will drastically limit the rejection ratio, which will decrease proportionally to the square of the numerical aperture. However, a single-mode fiber is used at the focus of the beam combiner to perform wavefront filtering. This single-mode fiber will change the electric field distribution and affect the performance of the multi-axial beam combiner. For a three-beam phase-based nulling interferometer, the rejection ratio after fiber filtering is now inversely proportional to the fourth power of the numerical aperture. For a typical numerical aperture of 0.06, the rejection ratio should be of the order of $10^6 - 10^8$. For all other numbers of beams or for interferometers based on rotation of the polarization, the rejection ratio after the fiber is theoretically infinite regardless of the numerical aperture. Therefore, longitudinal polarization should not prevent the detection of an Earth-like exoplanet. However, a trade-off has to be made between a high rejection ratio and a high photon flux.

Finally, we presented experimental results obtained with our table-top experimental set-up. The previously-obtained results were explained by pointing out important spectral and polarization mismatchings between the beams. The theoretical results on the effect of dispersion in nulling were validated experimentally in the two-beam case. A first implementation of nulling interferometry using polarization has been realized on this experimental set-up, leading to a relatively limited rejection ratio. The spectral and polarization mismatchings and the lack of optical symmetry led to the design of a new three-beam interferometer. This design is fully symmetric assuming identical optical components and should therefore allow a high rejection ratio. Unfortunately, even though, all components were ordered and the set-up was ready to be used, time was missing to perform actual measurements. We expect to perform these measurements during the coming months and we hope to reach a $10^4 - 10^5$-rejection ratio in a $40 - 50\%$-wide spectral band. We expect the rejection ratio to be currently limited by the wavefront quality of the different beams. In the visible, aberrations can be relatively large. Even though a single-mode fiber is used as a wavefront filter, the rejection ratio could still be limited by aberrations because of the wavelength-dependent coupling efficiency with the fiber. Therefore, attention should be paid to aberrations for any experimental set-up in the visible. Even though not mentioned

in this thesis, preliminary studies of the influence of aberrations and the efficiency of the wavefront filtering have been performed. We hope to have time in the future to study this effect in more detail.

In the introduction of this thesis, we discussed the state of the art in nulling interferometry by showing the main experimental results that have been obtained these last ten years (see Figure 1.7). We can now look back and add our results to this chart (see stars in Figure 7.1). We see that our monochromatic results are reasonably good, even though they were only performed for alignment purpose. The three-beam measurement is particularly remarkable since it is the only three-beam measurement in the chart. Only the results from Martin et al. [39] were performed with a four-beam interferometer. Our broadband measurements are, on an absolute scale, relatively low. However, they distinguish themselves by the very wide spectral band in which they were performed. In particular, the dispersion measurement is theoretically limited, as opposed to experimentally limited. The only way to improve the rejection ratio is to increase the number of beams to three or to four, validating therefore the relevance of such a method. As discussed in this thesis, quite low results have been obtained with our promising polarization nulling interferometry due to severe limitations in our previous set-up. Hopefully, these problems should be solved in our new experimental set-up and we should therefore be able to reach a rejection ratio falling in the grey region of Figure 7.1.

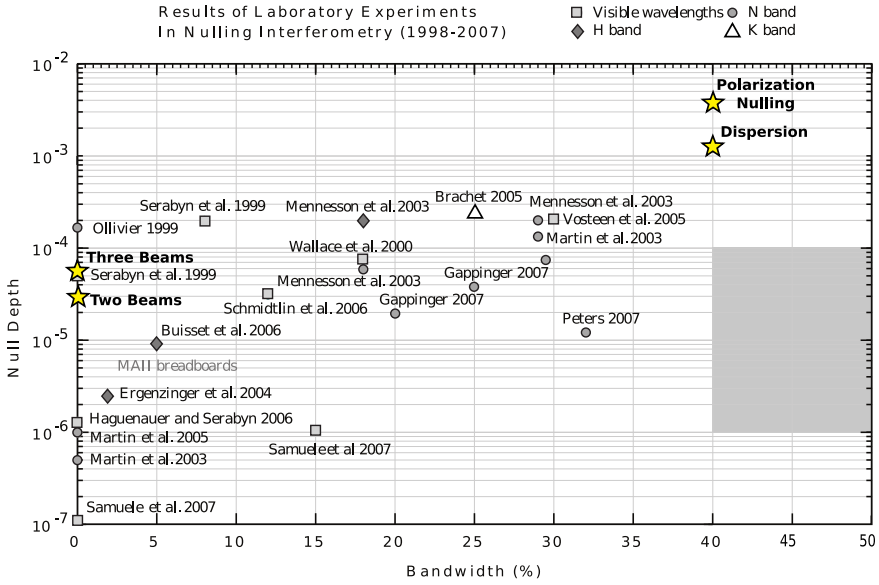

Figure 7.1: State of the art in nulling interferometry: null depth as a function of the bandwidth. The squares represent the measurements performed at visible wavelengths, the diamonds around 1.5 μm, the star around 2.2 μm and the circles have been performed in the mid-infrared around 10 μm. Courtesy of Peter R. Lawson (Jet Propulsion Laboratory, Caltech). On this chart, we added the results obtained throughout this thesis (stars). The grey box represents the region that we hope to achieve with our new set-up.

In conclusion, with this theoretical, numerical and experimental research, we opened the way to new possibilities for Earth-like exoplanet detection via nulling interferometry.

Appendix A

Mathematical definitions

In this appendix, we will summarize most of the mathematical definitions used throughout this thesis.

A.1 Bessel functions

In this section, we will present some properties of the Bessel functions.

The Bessel function of the first kind of order m, as defined in [74], is given by the integral

$$J_n(x) = \frac{i^{-n}}{\pi} \int_0^{\pi} \exp(ix\cos\phi)\cos(n\phi)\, d\phi. \tag{A.1}$$

From Eq. (A.1), we can derive the following expressions,

$$\begin{aligned}
\int_0^{2\pi} \exp\left[irk_r\cos(k_\phi-\phi)\right] d\phi &= \int_{k_\phi}^{2\pi+k_\phi} \exp\left[irk_r\cos(k_\phi-\phi)\right] d\phi \\
&= \int_0^{2\pi} \exp\left(irk_r\cos\phi\right) d\phi \\
&= \int_0^{\pi} \exp\left(irk_r\cos\phi\right) d\phi + \int_{\pi}^{2\pi} \exp\left(irk_r\cos\phi\right) d\phi \\
&= \underbrace{\int_0^{\pi} \exp\left(irk_r\cos\phi\right) d\phi}_{\pi J_0(rk_r)} + \underbrace{\int_0^{\pi} \exp\left(-irk_r\cos\phi\right) d\phi}_{(\pi J_0(rk_r))^*} \\
&= 2\pi J_0(rk_r).
\end{aligned} \tag{A.2}$$

We also have

$$\begin{aligned}
\int_0^{2\pi} \exp\left[irk_r\cos(k_\phi-\phi)\right]\cos\left(2\phi\right)d\phi &= \int_{k_\phi}^{2\pi+k_\phi} \exp\left[irk_r\cos(k_\phi-\phi)\right]\cos\left(2\phi\right)d\phi \\
&= \int_0^{2\pi} \exp\left(irk_r\cos\phi\right)\cos\left(2k_\phi-2\phi\right)d\phi \\
&= \cos\left(2k_\phi\right)\int_0^{2\pi} \exp\left(irk_r\cos\phi\right)\cos\left(2\phi\right)d\phi \\
&\quad +\sin\left(2k_\phi\right)\int_0^{2\pi} \exp\left(irk_r\cos\phi\right)\sin\left(2\phi\right)d\phi \\
&= \cos\left(2k_\phi\right)\int_0^{2\pi} \exp\left(irk_r\cos\phi\right)\cos\left(2\phi\right)d\phi \\
&= -2\pi J_2(rk_r)\cos\left(2k_\phi\right), \qquad \text{(A.3)}
\end{aligned}$$

and

$$\begin{aligned}
\int_0^{2\pi} \exp\left[irk_r\cos(k_\phi-\phi)\right]\sin\left(2\phi\right)d\phi &= \int_{k_\phi}^{2\pi+k_\phi} \exp\left[irk_r\cos(k_\phi-\phi)\right]\sin\left(2\phi\right)d\phi \\
&= \int_0^{2\pi} \exp\left(irk_r\cos\phi\right)\sin\left(2k_\phi-2\phi\right)d\phi \\
&= -\cos\left(2k_\phi\right)\int_0^{2\pi} \exp\left(irk_r\cos\phi\right)\sin\left(2\phi\right)d\phi \\
&\quad +\sin\left(2k_\phi\right)\int_0^{2\pi} \exp\left(irk_r\cos\phi\right)\cos\left(2\phi\right)d\phi \\
&= \sin\left(2k_\phi\right)\int_0^{2\pi} \exp\left(irk_r\cos\phi\right)\cos\left(2\phi\right)d\phi \\
&= -2\pi J_2(rk_r)\sin\left(2k_\phi\right). \qquad \text{(A.4)}
\end{aligned}$$

A.2 Sum identities

In this section, we will present some basic sum identities. In all cases, we will consider $N > 1$.

$$\sum_{j=1}^{N} \exp\left(i\, n \frac{2\pi}{N}(j-1)\right) = \begin{cases} N, & \text{if } n = mN, m \in \mathbb{N} \text{ and } m > 0 \\ 0, & \text{otherwise} \end{cases}. \tag{A.5}$$

As a consequence, we have

$$\sum_{j=1}^{N} \cos\left(n \frac{2\pi}{N}(j-1)\right) = \begin{cases} N, & \text{if } n = mN, m \in \mathbb{N} \text{ and } m > 0 \\ 0, & \text{otherwise} \end{cases}, \tag{A.6}$$

and

$$\sum_{j=1}^{N} \sin\left(n \frac{2\pi}{N}(j-1)\right) = 0. \tag{A.7}$$

We also have

$$\begin{aligned} &\sum_{j=1}^{N} \cos\left(2\frac{2\pi}{N}(j-1)\right) \exp\left(i\frac{2\pi}{N}(j-1)\right) \\ &= \frac{1}{2}\sum_{j=1}^{N} \exp\left(i\, 3\frac{2\pi}{N}(j-1)\right) + \frac{1}{2}\sum_{j=1}^{N} \exp\left(-i\frac{2\pi}{N}(j-1)\right) \\ &= \begin{cases} 3/2, & \text{if } N = 3 \\ 0, & \text{if } N \neq 3 \end{cases}, \end{aligned} \tag{A.8}$$

and

$$\begin{aligned} &\sum_{j=1}^{N} \sin\left(2\frac{2\pi}{N}(j-1)\right) \exp\left(i\frac{2\pi}{N}(j-1)\right) \\ &= \frac{1}{2i}\sum_{j=1}^{N} \exp\left(i\, 3\frac{2\pi}{N}(j-1)\right) - \frac{1}{2i}\sum_{j=1}^{N} \exp\left(-i\frac{2\pi}{N}(j-1)\right) \\ &= \begin{cases} -3i/2, & \text{if } N = 3 \\ 0, & \text{if } N \neq 3 \end{cases}. \end{aligned} \tag{A.9}$$

Appendix B

Fundamental mode of a single-mode fiber

We will consider a step-profile fiber unbounded in the radial direction. This infinite-cladding approximation is good if the decay length of the modes in the cladding is small compared to the actual thickness of the cladding, which is the case in the fiber we simulated. We also assume that the fiber profile is z-invariant. The refractive index is then given by

$$n(r) = \begin{cases} n_{co}, & \text{if } 0 \leq r < a \\ n_{cl}, & \text{if } a < r < \infty \end{cases}, \tag{B.1}$$

where a is the core radius. From these refractive indices, we can define a numerical aperture NA and a fiber parameter V,

$$NA = \sqrt{n_{co}^2 - n_{cl}^2} \quad \text{and} \quad V = ka\sqrt{n_{co}^2 - n_{cl}^2}, \tag{B.2}$$

where k is the wave number. This fiber parameter V determines the number of modes propagating in the fiber. For instance, a step-profile fiber is single-mode if $V < 2.405$. We can also define a profile height parameter Δ,

$$\Delta = \frac{1}{2}\left(1 - \frac{n_{cl}^2}{n_{co}^2}\right). \tag{B.3}$$

Each mode propagating in the fiber has a certain propagation constant β from which we can define modal parameters for the core U and the cladding W,

$$U = a\sqrt{k^2 n_{co}^2 - \beta^2} \quad \text{and} \quad W = a\sqrt{\beta^2 - k^2 n_{cl}^2}. \tag{B.4}$$

In order to simplify the notation and to comply with [68], we will introduce a set of parameters

$$\begin{aligned} b_1 &= \tfrac{1}{2U}\left[\tfrac{J_0(U)}{J_1(U)} - \tfrac{J_2(U)}{J_1(U)}\right]; & b_2 &= -\tfrac{1}{2W}\left[\tfrac{K_0(W)}{K_1(W)} + \tfrac{K_2(W)}{K_1(W)}\right], \\ F_1 &= (\tfrac{UW}{V})^2\left(b_1 + (1-2\Delta)b_2\right); & F_2 &= (\tfrac{V}{UW})^2 \tfrac{1}{b_1+b_2}, \\ a_1 &= \tfrac{F_2-1}{2}; & a_2 &= \tfrac{F_2+1}{2}, \\ a_3 &= \tfrac{F_1-1}{2}; & a_4 &= \tfrac{F_1+1}{2}, \\ a_5 &= \tfrac{F_1-1+2\Delta}{2}; & a_6 &= \tfrac{F_1+1-2\Delta}{2}, \end{aligned} \tag{B.5}$$

where J_ν is the Bessel function of the first kind and K_ν is the modified Bessel function of the second kind.

Using these definitions, the propagation constant β (and therefore the modal parameters U and W) can be found by solving the eigenvalue equation derived in [68],

$$k^2 n_{co}^2 F_1 = \beta^2 F_2. \tag{B.6}$$

The transverse electric field (E_r, E_ϕ) for the two fundamental modes (even and odd) is given in polar coordinates ($\rho_0 = r/a, \phi$) by [68]

$$E_r = \begin{cases} -\frac{a_1 J_0(U\rho_0)+a_2 J_2(U\rho_0)}{J_1(U)} f(\phi), & \text{if } 0 \le \rho_0 \le 1 \\ -\frac{U}{W}\frac{a_1 K_0(W\rho_0)-a_2 K_2(W\rho_0)}{K_1(W)} f(\phi), & \text{if } 1 \le \rho_0 < \infty \end{cases}, \tag{B.7a}$$

$$E_\phi = \begin{cases} -\frac{a_1 J_0(U\rho_0)-a_2 J_2(U\rho_0)}{J_1(U)} g(\phi), & \text{if } 0 \le \rho_0 \le 1 \\ -\frac{U}{W}\frac{a_1 K_0(W\rho_0)+a_2 K_2(W\rho_0)}{K_1(W)} g(\phi), & \text{if } 1 \le \rho_0 < \infty \end{cases}, \tag{B.7b}$$

where $f(\phi)$ and $g(\phi)$ are given by

$$f(\phi) = \begin{cases} \cos\phi \\ \sin\phi \end{cases} \quad ; \quad g(\phi) = \begin{cases} -\sin\phi & \text{for even modes} \\ \cos\phi & \text{for odd modes} \end{cases}. \tag{B.8}$$

The x- and y-components of the electric field (E_x, E_y) can then be calculated using

$$E_x = E_r \cos\phi - E_\phi \sin\phi, \tag{B.9a}$$

$$E_y = E_r \sin\phi + E_\phi \cos\phi. \tag{B.9b}$$

For the transverse magnetic field of the two fundamental modes (even and odd), we have

$$H_r = \begin{cases} \left(\frac{\epsilon_0}{\mu_0}\right)^{1/2} \frac{k n_{co}^2}{\beta}\frac{a_3 J_0(U\rho_0)-a_4 J_2(U\rho_0)}{J_1(U)} g(\phi), & \text{if } 0 \le \rho_0 \le 1 \\ \left(\frac{\epsilon_0}{\mu_0}\right)^{1/2} \frac{k n_{co}^2}{\beta}\frac{U}{W}\frac{a_5 K_0(W\rho_0)+a_6 K_2(W\rho_0)}{K_1(W)} g(\phi), & \text{if } 1 \le \rho_0 < \infty \end{cases}, \tag{B.10a}$$

$$H_\phi = \begin{cases} -\left(\frac{\epsilon_0}{\mu_0}\right)^{1/2} \frac{k n_{co}^2}{\beta}\frac{a_3 J_0(U\rho_0)+a_4 J_2(U\rho_0)}{J_1(U)} f(\phi), & \text{if } 0 \le \rho_0 \le 1 \\ -\left(\frac{\epsilon_0}{\mu_0}\right)^{1/2} \frac{k n_{co}^2}{\beta}\frac{U}{W}\frac{a_5 K_0(W\rho_0)-a_6 K_2(W\rho_0)}{K_1(W)} f(\phi), & \text{if } 1 \le \rho_0 < \infty \end{cases}, \tag{B.10b}$$

and

$$H_x = H_r \cos\phi - H_\phi \sin\phi, \tag{B.11a}$$

$$H_y = H_r \sin\phi + H_\phi \cos\phi. \tag{B.11b}$$

Finally, the longitudinal fields (E_z, H_z) are given by

$$E_z = \begin{cases} \frac{-iU}{a\beta}\frac{J_1(U\rho_0)}{J_1(U)} f(\phi), & \text{if } 0 \le \rho_0 \le 1 \\ \frac{-iU}{a\beta}\frac{K_1(W\rho_0)}{K_1(W)} f(\phi), & \text{if } 1 \le \rho_0 < \infty \end{cases}, \tag{B.12a}$$

$$H_z = \begin{cases} -i\left(\frac{\epsilon_0}{\mu_0}\right)^{1/2} \frac{UF_2}{ka}\frac{J_1(U\rho_0)}{J_1(U)} g(\phi), & \text{if } 0 \le \rho_0 \le 1 \\ -i\left(\frac{\epsilon_0}{\mu_0}\right)^{1/2} \frac{UF_2}{ka}\frac{K_1(W\rho_0)}{K_1(W)} g(\phi), & \text{if } 1 \le \rho_0 < \infty \end{cases}. \tag{B.12b}$$

Bibliography

[1] M. Mayor and D. Queloz, "A Jupiter-mass companion to a solar-type star," Nature **378**(6555), 355–359 (1995).

[2] D. Charbonneau, T. Brown, D. Latham, and M. Mayor, "Detection of Planetary Transits Across a Sun-like Star," Astrophys. J. **529**(1), L45–L48 (2000).

[3] M. A. C. Perryman, "Extra-solar planets," Reports on Progress in Physics **63**(8), 1209–1272 (2000).

[4] A. Einstein, "Lens-like action of a star by the deviation of light in the gravitational field," Science **84**(2188), 506–507 (1936).

[5] A. Léger, J.-M. Mariotti, M. Ollivier, and B. Mennesson, "Search for Extra-Solar Life through Planetary Spectroscopy," in *Origins*, C. E. Woodward, J. M. Shull, and H. A. Thronson, Jr., eds., vol. 148 of *Astronomical Society of the Pacific Conference Series*, pp. 458–+ (1998).

[6] A. Brack, "Life in the solar system," Advances in Space Research **24**(4), 417–433 (1999).

[7] A. Brack, "Liquid water and the origin of life," Origins of Life and Evolution of Biospheres **23**(1), 3–10 (1993).

[8] A. Léger, M. Ollivier, K. Altwegg, and N. J. Woolf, "Is the presence of H_2O and O_3 in an exoplanet a reliable signature of a biological activity?" Astron. Astrophys. **341**, 304–311 (1999).

[9] L. Kaltenegger, M. Fridlund, and J. Kasting, "Review on habitability and biomarkers," in *Earth-like Planets and Moons*, B. H. Foing and B. Battrick, eds., vol. 514 of *ESA Special Publication*, pp. 277–282 (2002).

[10] J. R. Angel, A. Y. S. Cheng, and N. J. Woolf, "A space telescope for IR spectroscopy of Earthlike planets," Nature **232**, 341–343 (1986).

[11] B. Lyot, "The study of the solar corona and prominences without eclipses (George Darwin Lecture, 1939)," MNRAS **99**, 538–+ (1939).

[12] F. Roddier and C. Roddier, "Stellar Coronograph with Phase Mask," Publ. Astron. Soc. Pac. **109**, 815–820 (1997).

[13] D. Rouan, P. Riaud, A. Boccaletti, Y. Clénet, and A. Labeyrie, "The Four-Quadrant Phase-Mask Coronagraph. I. Principle," Publ. Astron. Soc. Pac. **112**, 1479–1486 (2000).

[14] P. Riaud, A. Boccaletti, D. Rouan, F. Lemarquis, and A. Labeyrie, "The Four-Quadrant Phase-Mask Coronagraph. II. Simulations," Publ. Astron. Soc. Pac. **113**, 1145–1154 (2001).

[15] D. Mawet, P. Riaud, O. Absil, and J. Surdej, "Annular Groove Phase Mask Coronagraph," The Astrophysical Journal **633**(2), 1191–1200 (2005).

[16] R. N. Bracewell, "Detecting nonsolar planets by spinning infrared interferometer," Nature **274**(5673), 780–781 (1978).

[17] J. Angel and N. J. Woolf, "An Imaging Nulling Interferometer to Study Extrasolar Planets," The Astrophysical Journal **475**(1), 373–379 (1997).

[18] B. Mennesson, A. Leger, and M. Ollivier, "Direct detection and characterization of extrasolar planets: The Mariotti space interferometer," Icarus **178**(2), 570–588 (2005).

[19] Y. Rabbia, J. Gay, J.-P. Rivet, and J.-L. Schneider, "Review of Concepts and Constraints for Achromatic Phase Shifters," in *GENIE - DARWIN Workshop - Hunting for Planets*, vol. 522 of *ESA Special Publication* (2003).

[20] E. Serabyn and M. M. Colavita, "Fully symmetric nulling beam combiners," Appl. Opt. **40**(10), 1668–1671 (2001).

[21] A. Title and W. Rosenberg, "Achromatic retardation plates," in *Polarizers and applications*, vol. 307 of *Proc. SPIE*, pp. 120–125 (1981).

[22] S. Pancharatnam, "Generalized theory of interference, and its applications," Proc. Ind. Acad. Sci. A **44**, 247 (1956).

[23] P. Hariharan and P. E. Ciddor, "An achromatic phase-shifter operating on the geometric phase," Opt. Comm. **110**(1-2), 13–17 (1994).

[24] N. Baba, N. Murakami, , and T. Ishigaki, "Nulling interferometry by use of geometric phase," Opt. Lett. **26**(15), 1167–1169 (2001).

[25] D. Mawet, J. Baudrand, C. Lenaerts, V. Moreau, P. Riaud, D. Rouan, and J. Surdej, "Birefringent achromatic phase shifters for nulling interferometry and phase coronography," in *Towards Other Earths: DARWIN/TPF and the Search for Extrasolar Terrestrial Planets*, vol. 539 of *ESA Special Publication*, pp. 519–524 (2003).

[26] D. Rouan and D. Pelat, "The achromatic chessboard, a new concept of phase shifter for Nulling Interferometry - I. theory," ArXiv e-prints **802** (2008). 0802.3334.

[27] A. L. Mieremet, J. Braat, H. Bokhove, and K. Ravel, "Achromatic phase shifting using adjustable dispersive elements," vol. 4006 of *Proc. SPIE*, pp. 1035–1041 (2000).

[28] A. Mieremet and J. Braat, "Nulling interferometry without achromatic phase shifters," Appl. Opt. **41**(22), 4697–4703 (2002).

[29] P. Haguenauer and E. Serabyn, "Deep nulling of laser light with a single-mode-fiber beam combiner," Appl. Opt. **45**(12), 2749–2754 (2006).

[30] C. Buisset, X. Rejeaunier, Y. Rabbia, C. Ruilier, M. Barillot, L. Lierstuen, and J. Armengol, "Multi-axial interferometry: demonstration of deep nulling and investigation of polarization effects," vol. 6268 of *Proc. SPIE*, p. 626819 (2006).

[31] B. Mennesson, M. Ollivier, and C. Ruilier, "Use of single-mode waveguides to correct the optical defects of a nulling interferometer," J. Opt. Soc. Am. A **19**(3), 596–602 (2002).

[32] O. Wallner, W. Leeb, and R. Flatscher, "Design of spatial and modal filters for nulling interferometers," vol. 4838 of *Proc. SPIE*, pp. 668–679 (2003).

[33] O. Wallner, J. P. Armengol, and A. Karlsson, "Multi-Axial Single-Mode Beam Combiner," vol. 5491 of *Proc. SPIE*, pp. 1417–1434 (2004).

[34] H. Bokhove, J. P. Kappelhof, H. J. P. Vink, L. L. A. Vosteen, and Z. Sodnik, "Broadband nulling using a prism phase shifter," in *Towards other Earths: DARWIN/TPF and the Search for Extrasolar Terrestrial Planets*, M. Fridlund, T. Henning, and H. Lacoste, eds., vol. 539 of *ESA Special Publication*, pp. 367–369 (2003).

[35] F. Brachet, A. Labeque, A. Leger, M. Ollivier, C. Lizambert, V. Hervier, B. Chazelas, B. Pellet, T. Lepine, and C. Valette, "Nulling interferometry for the Darwin Mission: polychromatic laboratory test bench," vol. 5491 of *Proc. SPIE*, pp. 991–998 (2004).

[36] K. Ergenzinger, R. Flatscher, U. Johann, R. Vink, and Z. Sodnik, "EADS Astrium Nulling Interferometer Breadboard for DARWIN and GENIE," in *5th International Conference on Space Optics*, B. Warmbein, ed., vol. 554 of *ESA Special Publication*, pp. 223–230 (2004).

[37] S. R. Martin, E. Serabyn, and G. Hardy, "Deep nulling of laser light in a rotational shearing interferometer," vol. 4838 of *Proc. SPIE*, pp. 656–667 (2003).

[38] S. R. Martin, R. O. Gappinger, F. M. Loya, B. P. Mennesson, S. L. Crawford, and E. Serabyn, "Mid-infrared nuller for Terrestrial Planet Finder: design, progress, and results," vol. 5170 of *Proc. SPIE*, pp. 144–154 (2003).

[39] S. Martin, P. Szwaykowski, and F. Loya, "Testing exo-planet signal extraction using the Terrestrial Planet Finder planet detection testbed," vol. 5905 of *Proc. SPIE*, p. 590508 (2005).

[40] B. Mennesson, S. L. Crawford, E. Serabyn, S. Martin, M. Creech-Eakman, and G. Hardy, "Laboratory performance of the Keck Interferometer nulling beam combiner," in *Towards other Earths: DARWIN/TPF and the Search for Extrasolar Terrestrial Planets*, M. Fridlund, T. Henning, and H. Lacoste, eds., vol. 539 of *ESA Special Publication*, pp. 525–528 (2003).

[41] B. Mennesson, P. Haguenauer, E. Serabyn, and K. Liewer, "Deep broad-band infrared nulling using a single-mode fiber beam combiner and baseline rotation," in *Advances in Stellar Interferometry*, J. D. Monnier, M. Schöller, and W. C. Danchi, eds., vol. 6268 of *Proc. SPIE* (2006).

[42] R. M. Morgan, J. H. Burge, and N. J. Woolf, "Final laboratory results of visible nulling with dielectric plates," in *Interferometry for Optical Astronomy II*, W. A. Traub, ed., vol. 4838 of *Proc. SPIE*, pp. 644–655 (2003).

[43] E. Schmidtlin, J. K. Wallace, R. Samuele, B. M. Levine, and M. Shao, "Recent progress of visible light nulling interferometry and first 1 million null result," in *IAU Colloq. 200: Direct Imaging of Exoplanets: Science and Techniques*, C. Aime and F. Vakili, eds., pp. 353–360 (2006).

[44] E. Serabyn, J. K. Wallace, G. J. Hardy, E. G. H. Schmidtlin, and H. T. Nguyen, "Deep Nulling of Visible Laser Light," Appl. Opt. **38**(34), 7128–7132 (1999).

[45] L. L. A. Vosteen, H. J. P. Vink, H. van Brug, and H. Bokhove, "Achromatic phase-shifter breadboard extensions," vol. 5905 of *Proc. SPIE*, p. 59050A (2005).

[46] V. Weber, M. Barillot, P. Haguenauer, P. Y. Kern, I. Schanen-Duport, P. R. Labeye, L. Pujol, and Z. Sodnik, "Nulling interferometer based on an integrated optics combiner," vol. 5491 of *Proc. SPIE*, pp. 842–850 (2004).

[47] K. Wallace, G. Hardy, and E. Serabyn, "Deep and stable interferometric nulling of broadband light with implications for observing planets around nearby stars," Nature **406**(6797), 700–702 (2000).

[48] O. P. Lay, M. Jeganathan, and R. Peters, "Adaptive nulling: a new enabling technology for interferometric exo-planet detection," vol. 5170 of *Proc. SPIE*, pp. 103–112 (2003).

[49] R. Peters, O. Lay, A. Hirai, and M. Jeganathan, "Adaptive nulling in the mid-IR for the terrestrial planet finder interferometer," in *Techniques and Instrumentation for Detection of Exoplanets III*, D. Coulter, ed., vol. 6693 of *Proc. SPIE*, p. 669315 (2007).

[50] O. P. Lay, S. R. Martin, and S. L. Hunyadi, "Planet-finding performance of the TPF-I Emma architecture," vol. 6693 of *Proc. SPIE*, p. 66930A (2007).

[51] H. Vink, H. Bokhove, B. Ouwerkeek, J. Kappelhof, H. van Brug, B. Snijders, and L. Vosteen, "Achromatic prism-based phaseshifter for nulling in the visible," vol. 4852 of *Proc. SPIE*, pp. 803–808 (2003).

[52] C. van der Avoort, A. Mieremet, S. Pereira, and J. Braat, "Demonstration of nulling using delay line phase shifters," vol. 5491 of *Proc. SPIE*, pp. 808–815 (2004).

[53] A. L. Mieremet and J. J. M. Braat, "Deep nulling by means of multiple-beam recombination," Appl. Opt. **42**(10), 1867–1875 (2003).

[54] N. Baba and N. Murakami, "A method to image extrasolar planets with polarized light," Publ. Astron. Soc. Pac. **115**(0), 1363–1366 (2003).

[55] R. Azzam and N. Bashara, *Ellipsometry and polarized light* (Elsevier, Amsterdam, 1987).

[56] P. Hariharan, "Achromatic and apochromatic halfwave and quarterwave retarders," Opt. Eng. **35**(11), 3335–3337 (1996).

[57] P. Hariharan and P. E. Ciddor, "Variable achromatic polarization rotators," Opt. Eng. **36**(9), 2563–2566 (1997).

[58] C. Koresko, B. Mennesson, E. Serabyn, M. Colavita, R. Akeson, and M. Swain, "Longitudinal dispersion control for the Keck Interferometer nuller," in *Interferometry in Optical Astronomy II*, vol. 4838 of *Proc. SPIE*, pp. 4838–127 (2002).

[59] J. Spronck, S. Pereira, and J. Braat, "Chromatism compensation in wide-band nulling interferometry for exoplanet detection," Appl. Opt. **45**(4), 597–604 (2006).

[60] O. Lay, "Removing instability noise in nulling interferometers," vol. 6268 of *Proc. SPIE*, p. 62681A (2006).

[61] B. Lane, M. Muterspaugh, and M. Shao, "Calibrating an interferometric null," Astrophysical Journal **648**(2), 1276–1284 (2006).

[62] E. Serabyn, "Nulling interferometry: symmetry requirements and experimental results," in *Interferometry in Optical Astronomy*, P. J. Lena and A. Quirrenbach, eds., vol. 4006 of *Proc. SPIE*, pp. 328–339 (2000).

[63] S. Quabis, R. Dorn, M. Eberler, O. Glöckl, and G. Leuchs, "The focus of light - theoretical calculation and experimental tomographic reconstruction," Appl. Phys. B **72**(0), 109–113 (2001).

[64] V. Ignatowsky, "Diffraction by a lens of arbitrary aperture," Tr. Opt. Inst. Petrograd **1**(4), 1–36 (1919).

[65] B. Richards and E. Wolf, "Electromagnetic diffraction in optical systems: II. Structure of the image field in an aplanatic system," Proc. Roy. Soc. A **253**(0), 358–379 (1959).

[66] A. S. van de Nes, L. Billy, S. F. Pereira, and J. J. M. Braat, "Calculation of the vectorial field distribution in a stratified focal region of a high numerical aperture imaging system," Opt. Exp. **12**(7), 1281–1293 (2004).

[67] O. Wallner and W. Leeb, "Minimum length of a single-mode fiber spatial filter," J. Opt. Soc. Am. A **19**, 2445–2448 (2002).

[68] A. Snyder and J. Love, *Optical waveguide theory* (Chapman and Hall, London, 1983).

[69] J. Spronck, S. Pereira, and J. Braat, "Polarization nulling interferometry for exoplanet detection," Opt. Exp. **14**(7), 2657–2670 (2006).

[70] J. Spronck, S. Pereira, and J. Braat, "Nulling interferometry without achromatic phase shifters: latest results," vol. 6268 of *Proc. SPIE*, p. 626832 (2006).

[71] J. Spronck, S. Pereira, and J. Braat, "Nulling interferometry for exoplanet detection using polarization properties," vol. 6268 of *Proc. SPIE*, p. 62681B (2006).

[72] J. Spronck, L. Vosteen, S. Pereira, and J. Braat, "Design of a polarization nulling interferometer for exoplanet detection," vol. 6693 of *Proc. SPIE*, p. 66930M (2007).

[73] J. Spronck, S. Pereira, and J. Braat, "Chromatic coupling efficiency of a single-mode optical fiber for nulling interferometry," Proc. IEEE/LEOS Benelux, pp. 277–280 (2005).

[74] M. Abramowitz and I. Segun, *Handbook of mathematical functions* (Dover, New York, 1968).

About the author

Julien Spronck is born in 1981 in Liège, Belgium. In 2004, he graduated *magna cum laude* in Physics Engineering at the University of Liège, Belgium. During the last three years of this cursus, he specialized in Space Techniques. His own interests pushed him towards the direction of Space Optics with a master thesis entitled "Study and design of a co-phased optical aperture generator". While working on this thesis, he applied for a Ph.D. position in the Optics Research Group of Delft University of Technology in the field of nulling interferometry for exoplanet detection. His knowledge in the field made him a suitable candidate. He started his Ph.D. in September 2004. The project was then supported by the Kenniscentrum voor Apertuur Synthese (KAS), a collaboration between the Netherlands Organisation for Applied Scientific Research (TNO) and Delft University of Technology. Even though, KAS ceased its activities in 2005, the project remained supported by TNO. In August 2006, the author attended the Michelson Summer Workshop on Frontiers of Interferometry: Stars, Disks, and Terrestrial Planets at the Michelson Science Center of California Institute of Technology, Pasadena, California. During his thesis, he was involved in the supervision of several students from The Netherlands as well as trainees from France. He also performed academic tasks in the form of practica for the courses of 'Waves' and 'Research Practica' in Fourier spatial filtering and in microscopy. He was also involved in the group project-oriented course 'Education in Applied Physics'. The results of his Ph.D. studies have been published in several refereed papers and presented in several international conferences (London, Mons, Orlando, Noordwijk, Paris, The Hague, San Diego, Lille and Marseille). Since 2007, he also holds an international patent entitled "Polarization nulling interferometry".

List of Publications

Refereed publications

1. "Chromatism compensation in wide-band nulling interferometry for exoplanet detection", J. Spronck, S.F. Pereira, and J.J.M. Braat. Appl. Opt. **45 (4)**, 597–604 (2006).

2. "Polarization nulling interferometry for exoplanet detection", J. Spronck, S. F. Pereira and J. J. M. Braat. Opt. Express **14 (7)**, 2657-2670 (2006).

3. "The effect of the longitudinal polarization component in multi-axial nulling interferometry for exoplanet detection", J. Spronck and S.F. Pereira. Submitted to Astron. Astrophys. (2008)

4. "The effect of dispersion in nulling interferometry for exoplanet detection", J.F.P. Spronck, J.W.N. Los and S.F. Pereira. In preparation.

5. "Multiplexing information on an optical disc by spatial and phase coding", S. F. Pereira, J. F. P. Spronck, K. Wagner, C.C.Harb, and H. Bachor. In preparation.

Patents

1. "Polarization nulling interferometry", J.F.P. Spronck, Patent WO2007111508, published on October 4th, 2007.

Conference proceedings

1. "Chromatic coupling efficiency of a single-mode optical fiber for nulling interferometry", J. Spronck, S. F. Pereira and J. J. M. Braat. Poster presentation at IEEE/LEOS Benelux Symposium 2005, Mons, Belgium (December 2005)

2. "Nulling interferometry for exo-planet detection using polarization properties", J. Spronck, S. F. Pereira and J. J. M. Braat. Oral presentation at SPIE conference on "Astronomical Telescopes and Instrumentation", 2006, Orlando, USA, (May 2006)

3. "Nulling interferometry without achromatic phase shifters: latest results", J. Spronck, S. F. Pereira and J. J. M. Braat. Poster presentation at SPIE conference on "Astronomical Telescopes and Instrumentation", 2006, Orlando, USA (May 2006)

4. "Three-dimensional electric field analysis in a multi-axial beam combiner for nulling interferometry", J. Spronck, S. F. Pereira and J. J. M. Braat. Poster presentation at International Conference on Space Optics (ICSO) 2006, Noordwijk, The Netherlands (June 2006)

5. "Vectorial analysis of polarization issues in multi-axial nulling interferometers for exoplanet detection", J. Spronck, S. F. Pereira and J. J. M. Braat. Oral presentation at SPIE conference on "Techniques and Instrumentation for Detection of Exoplanets III", 2007, San Diego, USA (August 2007)

6. "Design of a polarization nulling interferometer for exoplanet detection", J. Spronck, L.L.A. Vosteen, S. F. Pereira and J. J. M. Braat. Oral presentation at SPIE conference on "Techniques and Instrumentation for Detection of Exoplanets III", 2007, San Diego, USA (August 2007)

7. "Compensation and optimization of dispersion in nulling interferometry", J.F.P. Spronck, J.W.N. Los and S.F. Pereira. Oral presentation at SPIE conference on "Astronomical Telescopes and Instrumentation", 2008, Marseille, France (June 2008)

Conference contributions

1. "Chromatism compensation in wide-band nulling interferometry for exoplanet detection", J. Spronck, S. F. Pereira and J. J. M. Braat. Oral presentation at Advanced Optical Imaging, topical meeting of the European Optical Society (EOS) 2005, London, United Kingdom (June 2005)

2. "Single-mode optical fibers in nulling interferometry: chromaticity and longitudinal polarization issues", J. Spronck, S. F. Pereira and J. J. M. Braat. Poster presentation at the EOS Annual Meeting, 2006, Paris, France (October 2006).

3. "Single-mode optical fibers in nulling interferometry: chromaticity and longitudinal polarization issue", J. Spronck,S. F. Pereira and J. J. M. Braat. Poster presentation at IOP Fotonica Evenement, 2007, Den Haag, The Netherlands (April 2007).

4. "Influence of aberrations on the performances of a nulling interferometer for exoplanet detection", J. Spronck and J.J.M. Braat. Advanced Optical Imaging, topical meeting of the European Optical Society (EOS) 2007, Lille, France (September 2007)

Acknowledgements

This is my favorite section ... the one where I get to speak freely. The one written by my heart and where my heart is relieved from the gratefulness that I am usually not able to express. And what I like the most about this section is that it is the only one that most of the people actually read.

I first would like to acknowledge the people who directly contributed to the realization of this thesis. I am extremely grateful to ...

... **Joseph**, for inviting me on that day of February 2004 and giving me the opportunity to work in this particularly pleasant group (despite the non-suit-matching shoes that I was wearing that day). Thank you for your endless support and for the numerous fruitful and interesting discussions. I also would like to thank you for helping me to keep up with my mother tongue and to improve my Dutch level. Merci. Dank u.

... **Silvania**, for helping me daily with every single aspect of this thesis ... from cover to cover ... from the first day until the last one. I also would like to thank you for being so kind and welcoming. And for all the excellent food that you made for us. Obrigado.

... All students and interns who helped me a lot with the experimental work: **François**, **Fons**, **Marion**, **Niels**, **Jan**. Your help was very much appreciated. Thank you.

I would like to thank people at TNO without which this project would not have been possible: ...

... **Amir Vosteen**, for the very helpful discussions, especially about the design of the new experimental set-up. Thank you for always showing an interest in my work and for sharing your ideas and your valuable knowledge. Bedankt.

... **Henk Bokhove**, for fruitful discussions, mainly about the patent and the design of the new experimental set-up. Bedankt.

... **Ben Braam**, for your support. Bedankt.

I am also grateful to all members of my defence committee **Prof. H. Paul Urbach**, **Prof. Jean Surdej**, **Prof. Christoph Keller**, **Dr. Pierre Kern** and **Dr. ir. Ad A.M. Maas** for accepting to be part of the committee and for their interesting comments and suggestions. I am particularly thankful to ...

... **Jean Surdej**, for constructive discussions and for inviting me several times to Liège.

Merci.

... **Pierre Kern**, for very productive suggestions and for giving me the opportunity to give a seminar in LAOG, Grenoble and to visit the labs. Merci.

I also would like to thank **Rodolphe Krawczyk** for inviting me to Thalès Alenia Space (formerly known as Alcatel Alenia Space). Merci.

I am very thankful to all people at Optica for a very nice work environment and for sharing so much good time, in particular:

... **Yvonne** and **Lucia**, for the great job they always achieve. Bedankt.

... **Marnix**, for being there when needed. Bedankt.

... **Rob**, for his always excellent work and for the time he spent to design and build very important parts of the set-up. Bedankt.

... **Roland**, for the infinity of problems that he solved during these four years (sometimes only his presence helped solving the problem). Bedankt.

... **Raymond**, for his well-appreciated expertise. Bedankt.

And now, here comes the time I get to thank all the friends that I made during these four years:

... **Edgar**, for being my first friend in the optics group, for making me feel like at home where my home was not. I'll always remember that morning in Fjällbacka. Salamat.

I particularly would like to thank the "little women" for allowing me to bother them as much as I wanted:

... **Aura**, for a lot of things that we shared in four years: food of course, words, laughters, complicity, a lot of arguments and all the necessary distractions. Thank you as well for sharing my nervousness and for bearing the unbearable. That is how I would define friendship. Priceless. I could never have dreamt of a better office-mate. Cepat tinggalkan masa lalu, kita jelang hari. Saya akan rindu kamu. Terima kasih.

... **Reshmi\Reshmi\Reshmi**, for all the things that you taught me about your rich culture. Even we did not meet on the market, your friendship is very valuable to me. So is your constant smile ... always cheering up. Nandi.

... **Man**: I am also grateful to you for the extremely precious complicity, for your sweetness and your laughter. Don't worry, I'd visit you in Eindhoven and I'd definitely visit you in China. Xie xie.

And I am also thankful to ...

... **Janne**, for giving me a hint of Dutch culture and for being my best Dutch friend. Tot de volgende mosseldag of iets anders. Bedankt.

... **Oana**, for always being cheerful and welcoming (at least when you have no deadline). Multumesc.

... **Maarten**, (to practice your french), merci d'avoir été notre bouc émissaire. Comme on dit en français ... Qui aime bien, châtie bien. If you ask Aurèle what the last sentence means, he'll tell you something like "Spank me if you love me", which is not quite what I mean. Bedankt, Maarten. Succes.

... **Bas** and **Peter**, for always being part of any activity we would come up with. Bedankt.

... **Aurélie**, for the six months that you spent here with us. Mémorable. Merci.

... **Sven**, for your almost silent footstep, sometimes scary, but most of the time announcing the coffee break.

For everybody else from the Optics Group who contributed to make this group so "gezellig": **Cas**, **Olaf**, **Arthur**, **Sami**, **Hannah**, **Morris**, **Luat**, **Joe**, **Nick**, **Wouter**, **Mounir**, **Gopakumar**, **Nandini**, **Paul**, **Fokke**, **Florian** and **Paul** (please forgive me if I forgot someone).

And then destiny tricked me and decided to make me a climber (in the sense that I climb, not in the sense that I would be any good at it). Like others did before me, I found very strange to start climbing in this country. But nevertheless, I did and I liked it. So I would like to thank all those people who saw mountains where there was nothing (or not more than a wall):

... **Aude** and **Michaël**, pour tous ces bons moments, pour votre amitié, votre accueil et votre chaleur humaine. Merci.

... **Julie**, la femme de ma vie + 20 cm ;o) ... pour tous les fous rires et cette complicité partagés. Merci.

... **Marcos**, **Carla**, supongo que estaís riendo ahora porque estaís imaginandome hablar con una diferente voz ... Y Carla se va cantando: "Qué lindo brazito que tengo yo, qué lindo y pequeño que Dios me dio." ;o) ... Me gustaría agradeceros por vuestra amistad, por todos esos buenos momentos que hemos vivido juntos y por todos los momentos que viviremos. Muchas gracias.

... **Uli** und **Swantje** (now I can call you climbers), for being the most friendly couple of the whole Delft and I guess from the whole Germany. Vielen Danken.

I also would like to thank all other climbers: **Alexis**, **Flavie**, **Adrien**, **Loïc**, **Agnès**, **Amer**, **Steffi** and others.

I am also grateful to all other people that I met in Delft, which made these four years a great experience. I particularly thank **Ralph** for being welcoming (you didn't always have the choice) and of course for always being so German. Danke. I also thank the Jungle-Egg Worshippers, (**Marnix** and **Tai**), for all the fun we had. Bedankt. Thank you.

Almost last but not least, I am extremely thankful to ...

... **Aurèle** ... for everything else. (I'll keep it extremely short for the sake of your ankles). Que serais-je sans toi? MERCI. MERCI. MERCI.

... **Shadaim**, tu sais pourquoi ;o) Merci.

Et maintenant, je voudrais remercier une catégorie de personnes qui me tient particulièrement à coeur:

... **Christophe** et **Virginie**, **Stéfano** et **Stéphanie**, **Alain**, **Sarah**, pour toujours être là quand j'ai besoin de vous. Longue vie aux Gogols et Standard champion. Merci.

... **Maman**, **Papa**, **Laurent**, **Valérie**, **Olivier**, **Maud**. Merci pour votre soutien et votre amour.

Et puis, la dernière mais non la moindre, **marraine**, pour sans cesse penser à moi et prier pour moi. Moi aussi, je pense à toi. Merci.

... Et quand l'heure du départ fut proche :

Ah! Dit le renard... Je pleurerai.

C'est ta faute, dit le petit prince, je ne te souhaitais point de mal, mais tu as voulu que je t'apprivoise...

Bien sûr, dit le renard.

Mais tu vas pleurer! Dit le petit prince.

Bien sûr, dit le renard. J'y gagne, dit le renard, à cause de la couleur du blé.

Thank you !!!